THERMAL CONDUCTIVITY OF UNSATURATED SOILS

By

Jun Yao

A dissertation submitted in partial fulfillment of the requirements for the degree of

Doctor of Philosophy (GEOLOGICAL ENGINEERING)

At the UNIVERSITY OF WISCONSIN-MADISON 2018

Date of final oral examination: 05/08/2018

The dissertation is approved by the following members of the Final Oral Committee:

William J. Likos, Professor, Civil and Environmental Engineering/Geological Engineering (advisor)
Dante O. Fratta, Associate Professor, Civil and Environmental Engineering/Geological Engineering
James M. Tinjum, Associate Professor, Geological Engineering/Engineering Professional Development
Francisco J. Arriaga, Assistant Professor, Soil Science
Matthew Ginder-Vogel, Assistant Professor, Civil and Environmental Engineering

© Copyright by Jun Yao 2018

All Rights Reserved

ABSTRACT

Heat transfer through soils is a fundamental process in many energy geosystems such as shallow geothermal heat exchangers, energy piles, buried high-voltage power cables in wind or solar energy applications, and subsurface thermal energy storage systems. In these and other applications in the growing field of energy geotechnics, thermal conductivity of unsaturated soils is critical for the performance of these energy geosystems involving coupled heat and moisture transport phenomena. There is considerable basic research need to more effectively link the fundamental soil thermal behavior to the soil (e.g., soil types and water content), environmental (e.g., temperature), and construction (e.g., stress) factors.

The first objective of this study is to explore appropriate experimental techniques and procedures to measure the thermal conductivity of unsaturated soils. Experiments were conducted to compare two sensing techniques for measuring thermal conductivity of unsaturated soils: (i) a modified transient plane source (MTPS) method for non-destructive measurements using a planar, interfacial heat reflectance sensor; and (ii) a transient line source (TLS-SP) method utilizing an embedded single-probe heat source. Measurement protocols for coarse-grained and fine-grained soils were developed. Thermal conductivity dry out curves (TCDCs) were measured for five soil types, including poorly-graded sand, well-graded sand with silt, silty sand, silt, and clay. The MTPS sensor consistently produced higher thermal conductivity for degrees of saturation greater than about 50%, but lower thermal conductivity for saturations less than 50%. Saturated thermal conductivity measured using the MTPS sensor ranged from 8% to 26% greater than values measured using the TLS-SP sensor. Dry thermal conductivity measurements were comparable (< 5% difference) for fine-grained soils, but were consistently and appreciably greater using the TLS-SP for coarse-grained soils. Mechanisms responsible for these differences include thermally-

induced water migration, latent heat transfer, sensor-soil contact resistance, gravity-induced water migration, and specimen heterogeneity. Secondary experiments indicated that the effects of gravity-induced water migration were insignificant within the short (< 5 min) time frame elapsed between sample preparation and measurement.

The second objective of this study is to investigate the effects of elevated temperature on thermal conductivity of unsaturated soils using an evaporative technique in a temperature-controlled oven at temperatures up to 75°C. Thermal conductivity of both sands at low to intermediate saturations ($S \sim 0.1$ to 0.5) increased appreciably at elevated temperature. Maximum thermal conductivity occurred at 75°C and around the point of critical saturation ($S_c \sim 0.1 - 0.13$), where thermal conductivity was about twice that at room temperature (~ 23 °C). This was attributed to the influence of latent heat transfer from vapor diffusion at air-water interfaces, which have a maximum surface area within this saturation regime. A new empirical model was proposed for predicting thermal conductivity dry out curves at elevated temperatures. Modeled TCDCs show good agreement with experimental results.

The third objective of this study is to investigate the coupled effects of temperature and stress level on thermal conductivity of unsaturated sands. A suction-controlled thermo-mechanical (SCTM) method has been developed to measure thermal conductivity of unsaturated soils at different temperatures (5.5 °C to 75.5 °C), isotropic net normal stresses (35 kPa to 400 kPa), and wetting conditions (hysteretic drying and wetting paths). This method permits quantification of thermal conductivity of soils under the influence of stress level and temperature (i.e. construction and environmental conditions). A poorly-graded sand is used to investigate the coupled effects of temperature and stress level on thermal conductivity of unsaturated sands. For saturated sand, thermal conductivity from the initial loading cycle increases with increasing isotropic net normal

stress (loading) and decreases along a different path with decreasing normal stress (unloading) due to the irreversible plastic strain. Thermal conductivity of saturated sand also shows a decreasing trend as temperature increases and is potentially due to increasing void space caused by thermal expansion of solid particles during heating. The thermal conductivity increases appreciably as both isotropic net normal stress and temperature increase at intermediate saturations ($S \sim 0.3$ to 0.75). Maximum thermal conductivity occurs at 75.5 °C and 400 kPa when S = 0.54, where the value of thermal conductivity is 4.59 W/m-K. The potential mechanisms responsible for increasing thermal conductivity in this saturation range are pore water redistribution and larger effective solid-solid contact area for heat transfer due to increased contact area and water meniscus between solid particles (particle deformation). Hysteresis in thermal conductivity with respect to wetting-drying direction is also observed due to the dilative pattern of soil specimen in the wetting direction.

ACKNOWLEDGEMENTS

First of all, I would like to express my sincere gratitude to my advisor, Professor William J. Likos, for his continuous support and mentorship of my Ph.D. study, for his patience, motivation and immense knowledge. I appreciate all his contribution of time, ideas and funding to make my Ph.D. experience productive and rewarding.

Besides my advisor, I would like to thank the rest of my Ph.D. thesis committee: Professor Dante O. Fratta, Professor James M. Tinjum, Professor Francisco J. Arriaga, and Professor Matthew Ginder-Vogel, for their insightful comments and encouragement. I also want to thank Xiaodong Wang for his great support in providing and designing lab instruments and devices in the lab. Additionally, I would like to give special thanks to Professor Jianyong Shi from Hohai University for his kind support and inspired advice during my Ph.D. study.

Thank you to the entire Geofamily, former graduate fellows and friends in Madison who made my experience unique and memorable. I would also like to thank my friends Xiaofei Chen, Lei Xu, Zi Wang, Zhe Liu, Zhenzhong Wu who have always offered their support inside and outside the United States.

Finally, I want to express my great gratitude to my parents, Baosheng Yao and Fengxia Wang for their endless support and love. The last special word of acknowledgement is to my dear wife, Yanyu Zhu, who has been extremely supportive of me during the process and has made countless sacrifices and help. She has always offered her love, tolerance and encouragement to prevent me from several wrong turns and made me finally reach this point.

TABLE OF CONTENTS

ABSTRACT	i
ACKNOWLEDGEMENTS	iv
TABLE OF CONTENTS	v
LIST OF FIGURES	viii
LIST OF TABLES	xii
1. INTRODUCTION	1
2. BACKGROUND: EXPERIMENTAL TECHNIQUES AND PROCEDURES FOR SOI THERMAL CONDUCTIVITY MEASUREMENTS	
2.1 INTRODUCTION	6
2.2 EXPERIMENTAL TECHNIQUES	7
2.2.1 Steady-state Method	7
2.2.2 Transient Method	8
2.2.3 Preliminary Comparison	11
2.3 EXPERIMENTAL PROCEDURES	11
2.3.1 Multiple-Specimen Procedures	12
2.3.2 Modified Hanging Column Procedures	12
2.3.3 Staged-Drying Procedures	15
2.3.4 Preliminary Comparison	16
2.4 SUMMARY	17
2.5 REFERENCES	18
2.6 TABLES	21
2.7 FIGURES	23
3. TRANSIENT PLANE AND LINE SOURCE METHODS FOR SOIL THERMAL CONDUCTIVITY	26
3.1 INTRODUCTION	26
3.2 MATERIALS AND METHODS	29
3.2.1 Test Materials	29
3.2.2 TCDC Measurement Sensors and Approaches	30
3.3 RESULTS AND DISCUSSION	
3.3.1 Measured Thermal Conductivity Dry-out Curves	33

3.3.2 Sensor Comparison	36
3.4 SUMMARY	41
3.5 REFERENCES	42
3.6 TABLES	46
3.7 FIGURES	49
4. THERMAL CONDUCTIVITY OF UNSATURATED SANDS AT MODERATELY	
ELEVATED TEMPERATURES (25°C TO 75°C)	
4.1 INTRODUCTION	56
4.2 BACKGROUND	58
4.3 PROPOSED MODEL	62
4.4 MATERIALS AND METHODS	63
4.5 RESULTS AND DISCUSSION	64
4.6 SUMMARY	66
4.7 REFERENCES	67
4.8 TABLES	70
4.9 FIGURES	73
5. THERMAL CONDUCTIVITY OF COMPACTED CLAYS	78
5.1 INTRODUCTION	78
5.2 MATERIALS AND METHODS	80
5.3 RESULTS AND DISCUSSION	82
5.4 SUMMARY	85
5.5 REFERENCES	86
5.6 TABLES	89
5.7 FIGURES	92
6. COUPLED EFFECTS OF TEMPERATURE AND STRESS LEVEL ON THERMAL	
CONDUCTIVITY OF UNSATURATED SOILS.	99
6.1 INTRODUCTION	99
6.2 EXPERIMENTAL PROGRAM	102
6.2.1 Experimental Set-up	102
6.2.2 Thermal Calibration	104
6.2.3 Specimen Preparation	105

6.2.4 Specimen Saturation	
6.2.5 Testing Procedures	
6.3 RESULTS AND DISCUSSION	110
6.4 SUMMARY	115
6.5 REFERENCES	116
6.6 TABLE	
6.7 FIGURES	121

LIST OF FIGURES

Figure 2-1. Transient sensing techniques: (a) TLS sensors in TLS-SP (single probe) and TLS-DP
(dual probe) configuration; (b) TPS sensor (Krupa and Malinarič, 2014); (c) MTPS sensor 23
Figure 2-2. Schematic of modified hanging column apparatus (after Smits et al. 2010) 24
Figure 2-3. Schematic of staged-drying test apparatus (after Woodward and Tinjum, 2013) 25
Figure 3-1. Grain size distribution curves for five test soils
Figure 3-2. Soil-water retention curves for five test soils
Figure 3-3. Schematic of MTPS sensor set-up for (a) multiple-specimen test procedure and (b)
single-specimen test procedure
Figure 3-4. TCDCs obtained using MTPS and TLS-SP sensors along with Lu and Dong (2015)
models for five test soils: (a) SP; (b) SW-SM; (c) SM; (d) CL; (e) ML
Figure 3-5. Comparison of measured thermal conductivity using TLS-SP and MTPS sensors 53
Figure 3-6. Relationship between maximum heating temperature and degree of saturation with
TLS-SP and MTPS sensors for coarse-grained soils. 54
Figure 3-7. Thermal conductivity measured using MTPS sensor at top soil surface (SP) over time.
Figure 4-1. Schematic of capillary-assisted vapor diffusion
Figure 4-2. Conceptual TCDCs at elevated temperatures
Figure 4-3. Grain size distribution curves for two test sands
Figure 4-4. SWCCs, measured and modeled (best-fit) TCDCs of (a) SP4; (b) SW-SM2
Figure 4-5. Relationship between ω and temperature for both sands
Figure 5-1. A schematic of (a) Lambe (1958) theory; (b) Olsen (1962) theory
Figure 5-2. Grain size distribution curves of four clayey soils

Figure 5-3. Standard Proctor compaction curves of four clayey soils
Figure 5-4. TCDCs along with Campbell (1985) model for four test soils: (a) ALT29; (b) ALT28;
(c) DC18; (d) LC8
Figure 5-5. Relationships between cut-off saturation and clay content from Campbell (1985)
correlation (in dash and solid lines) and actual fitting results from this study (in solid markers) 96
Figure 5-6. Comparison of measured thermal conductivity at wet and dry of optimum 97
Figure 5-7. Pore size frequency from Mercury Intrusion Porosimetry test for DC18
Figure 6-1. Primary coupled thermo-hydro-mechanical processes in soils (after François and
Laloui, 2008)
Figure 6-2: (a) Schematic and (b) Photo of Suction-Controlled Thermo-Mechanical (SCTM)
apparatus
Figure 6-3. Temperature-Controlling System (TCS) in SCTM apparatus
Figure 6-4. SCTM apparatus (TCS omitted) with specific sensor designations
Figure 6-5. Schematic of thermal calibration set-up
Figure 6-6. Thermal calibration curves for (a) heating and (b) cooling directions
Figure 6-7. Photos of specimen set-up: (a) forming jackets with neoprene membrane; (b) sensor
embedding after second layer of soil
Figure 6-8. Photos of packed specimen with sensors: (a) top view of layout of sensor cables and
lines; (b) side view of specimen with O-rings and thermocouple
Figure 6-9. Schematic of specimen saturation set-up
Figure 6-10. Temperature, isotropic net normal stress and matric suction paths of the soil specimen
test procedures

Figure 6-11. Results from (a) thermal conductivity and (b) void ratio and volumetric strain as a
function of isotropic net normal stresses at 20 °C during initial loading-unloading cycle for
saturated sand $(S = 1)$.
Figure 6-12. The relationship between saturated thermal conductivity (λ_{sat}) and void ratio at 20 °C
during initial loading-unloading cycle. 132
Figure 6-13. The relationship between saturated thermal conductivity (λ_{sat}), temperature (T), and
isotropic net normal stress (σ_c) in heating and loading cycles
Figure 6-14. The relationship between volumetric strain (ε_{ν}) , temperature (T) , and isotropic net
normal stress (σ_c) in heating and loading cycles.
Figure 6-15. The relationship between volumetric strain (ε_{ν}) and temperature (T) in heating
direction when $\sigma_c = 35 \text{ kPa}$
Figure 6-16. The relationship between (a) saturated thermal conductivity (λ_{sat}) and isotropic net
normal stress (σ_c); and (b) volumetric strain (ε_v) and isotropic net normal stress (σ_c) at each
temperature in loading and heating direction
Figure 6-17. Measured thermal conductivity as a function of saturation (S) and temperature (T)
when (a) $\sigma_c = 35$ kPa; (b) $\sigma_c = 100$ kPa; (c) $\sigma_c = 200$ kPa; and (d) $\sigma_c = 400$ kPa in heating and
loading directions
Figure 6-18. Differential thermal conductivity with respect to the thermal conductivity when σ_c =
35 kPa when (a) $T = 75$ C; (b) $T = 47.5$ °C; (c) $T = 20$ °C and 5.5 °C
Figure 6-19. Soil water characteristic curve (SWCC) in drying direction obtained from axis-
translation technique. 139
Figure 6-20. Schematic of contact area and pore water meniscus changes due to normal stress (Cho
and Santamarina. 2001)

Figure 6-21. Measured thermal conductivity of thermally dried specimen as a function of isotropic		
net normal stress	.41	
Figure 6-22. Measured thermal conductivity and SWCC in drying and wetting directions 1	.42	
Figure 6-23. Void ratio changes in drying and wetting directions at 35 kPa and 20 °C	43	

LIST OF TABLES

Table 2-1. Comparison of five techniques for measuring soil thermal conductivity
Table 2-2. Comparison of approximate time to obtain TCDCs
Table 3-1. Comparison of five techniques for measuring soil thermal conductivity
Table 3-2. Summary of MTPS and TLS-SP sensor specifications (manufacturer reported) 47
Table 3-3. Saturated thermal conductivity, dry thermal conductivity, and Lu and Dong (2015)
modeling parameters for five test soils
Table 4-1. Summary of index properties for two sands
Table 4-2. Summary of the results for best-fitting parameters
Table 4-3. Summary of R^2 at different temperatures of each model for two soils
Table 5-1. Summary of index properties for four clayey soils
Table 5-2. Summary of target and actual dry unit weight (γ_d) and water content (w) for clay
specimens 90
Table 5-3. Saturated thermal conductivity, dry thermal conductivity, critical saturation, and
Campbell (1985) modeling parameters for four test soils
Table 6-1. Summarized test program for different matric suction steps

CHAPTER ONE

INTRODUCTION

Soil thermal behavior has been widely researched from the perspective of agricultural soil science (e.g., the germinating and developing of seeds usually require a certain threshold temperature, which is dependent on the soil thermal properties). In geotechnical engineering, however, there remains relatively limited studies on the topic of soil thermal behavior compared to the number of studies on traditional geotechnical research areas (i.e., mechanical and hydraulic behavior of soil). More recent studies on soil thermal behavior are related to emerging energy geotechnical applications, such as shallow geothermal heat exchangers, energy piles, buried power cables in wind or solar energy applications, subsurface thermal energy storage systems, and nuclear waste repositories.

Thermal conductivity of soils in these applications is critical for designing the systems and maintaining the efficiency. For example, in backfill design for buried power cables, it was found that 0.1 W/m-K decrease in thermal conductivity of backfill could result in approximate 16 years reduction of cable life without changing the electrical load (Karahan and Kalenderli, 2011). de leon and Anders (2008) studied the cable ampacity using finite element method and found that 0.5 W/m-K decrease in thermal conductivity of backfill could lead to 15% decrease in cable ampacity. Similarly, in the application of energy piles, thermal efficiency of the system could drop 40% if thermal conductivity of surrounding soil decreases from 2.65 W/m-K to 0.9 W/m-K (Akrouch *et al.*, 2016).

In these applications, soils are often unsaturated and thus include multiple phases (i.e., solid, liquid, and gas). Owing to the large contrast in the thermal conductivity of the solid, liquid and gas phases, soil thermal conductivity is not constant, but rather may change appreciably with changes

in pore water saturation from wetting or drying. The relationship between thermal conductivity and pore water saturation is often referred as thermal conductivity dryout curve (TCDC). A large number of experimental, analytical, and computational approaches for measuring or estimating the TCDC have been explored (*e.g.*, Campbell *et al.*, 1994; Côté and Konrad, 2005; Smits *et al.*, 2010; Likos, 2013, 2014; Yao *et al.*, 2014; Lu and Dong, 2015; Ghanbarian and Daigle, 2016). Other important factors that may affect the soil thermal properties include mineralogy, particle shape, particle and pore microstructures, bulk density and temperature (Shiozawa and Campbell, 1990).

This dissertation includes six chapters, including the introductory Chapter 1. Chapter 2, titled "Background: Experimental Techniques and Procedures for Soil Thermal Conductivity Measurements," reviews commonly used experimental techniques and procedures for measuring thermal conductivity of soils. This chapter provides a background to understand the fundamental techniques and procedures for development of experiments. A preliminary comparison of the reviewed experimental techniques and procedures has shown that transient sensor techniques are applicable over a range of thermal conductivity relevant to most unsaturated and saturated soils, and concurrent moisture content and thermal conductivity measurement is recommended for producing robust and continuous thermal conductivity dryout curves.

Chapter 3, titled "Transient Plane and Line Source Methods for Soil Thermal Conductivity," presents results from laboratory experiments conducted to compare two sensing techniques for measuring thermal conductivity and the TCDC of unsaturated soils: (i) a modified transient plane source (MTPS) method for non-destructive measurements using a planar, interfacial heat reflectance sensor; and (ii) a transient line source (TLS-SP) method using an embedded single-probe heat source. Thermal conductivity and thermal conductivity dry out curves (TCDCs) are measured and compared for five representative soil types, including poorly-graded sand, well-

graded sand with silt, silty sand, silt, and clay. Advantages and limitations are identified and recommendations for measuring TCDCs using each sensor and for different soil types (coarse-grained and fine-grained) are provided.

Chapter 4, titled "Thermal conductivity of unsaturated sands at moderately elevated temperatures (25°C to 75°C)," investigates the effect of temperature on thermal conductivity dryout curves. Two different sandy soils including a poorly graded sand and a well graded sand with silt are used to determine TCDCs at temperatures ranging from 25°C to 75°C. An empirical model is proposed based on the experimental observations and similar results available in the literature (Campbell *et al.*, 1994; Smits *et al.*, 2013). The proposed model is compared with five other empirical models incorporating the effects of water saturation and temperature for estimating TCDCs.

In Chapter 5, titled "Thermal Conductivity of Compacted Clays," each of four natural clayey soils was compacted at conditions dry of optimum Proctor compaction and a wet of optimum, respectively. Thermal conductivity of each specimen was measured over the full range of saturation to produce thermal conductivity dryout curves (TCDC). The main purpose of this study is to evaluate the difference between thermal conductivity of clay compacted dry of optimum and wet of optimum (and associated differences in soil fabric). An existing model is also evaluated for estimating thermal conductivity dryout curves for clayey materials.

In Chapter 6, titled "Coupled Effects of Temperature and Stress Level On Thermal Conductivity of Unsaturated Soils," introduced a new suction-controlled thermo-mechanical (SCTM) method to measure thermal conductivity of unsaturated soils at different temperatures (5.5 °C to 75.5 °C), isotropic normal stresses (35 kPa to 400 kPa), and wetting conditions. The apparatus consists of three main testing systems including temperature-control, pressure-control,

and sensor and data acquisition systems. This method permits quantification of thermal conductivity of soils under the influence of stress level and temperature (i.e. construction and environmental conditions). The primary objective of this study is to investigate the coupled effects of temperature and stress level on the thermal conductivity of unsaturated sand. Hysteresis in thermal conductivity with respect to wetting-drying, loading-unloading and heating-cooling is also investigated.

REFERENCES

- Akrouch, G. A., Sánchez, M., and Briaud, J. L. (2016). An experimental, analytical and numerical study on the thermal efficiency of energy piles in unsaturated soils. *Computers and Geotechnics*, 71, 207-220.
- Campbell, G. S., Jungbauer, J. D., Bidlake, W. R., and Hungerford, R. D. (1994). Predicting the effect of temperature on soil thermal conductivity. *Soil Science*, 158(5), 307-313.
- Côté, J. and Konrad, J. M. (2005). A generalized thermal conductivity model for soil and construction materials. *Canadian Geotechnical Journal*, 42, 443-458.
- De Leon, F., and Anders, G. J. (2008). Effects of backfilling on cable ampacity analyzed with the finite element method. *IEEE Transactions on Power Delivery*, 23(2), 537-543.
- Ghanbarian, B., and Daigle, H. (2016). Thermal conductivity in porous media: Percolation-based effective-medium approximation. *Water Resources Research*, *52*(1), 295-314.
- Karahan, M., and Kalenderli, O. (2011). Coupled electrical and thermal analysis of power cables using finite element method. In *Heat Transfer-Engineering Applications*. InTech.

- Likos, W.J. (2013). Modeling thermal conductivity dryout curves from soil-water characteristic curves, *Journal of Geotechnical and Geoenvironmental Engineering*, 140(5).
- Likos, W.J. (2014). Pore-scale model for thermal conductivity of unsaturated sand. *Journal of Geotechnical and Geological Engineering*, 33(2), 179-192.
- Lu, N. and Dong, Y. (2015). Closed-Form Equation for Thermal Conductivity of Unsaturated Soils at Room Temperature. *Journal of Geotechnical and Geoenvironmental Engineering*, 141(6).
- Shiozawa, S., and Campbell, G. S. (1990). Soil thermal conductivity. *Remote Sensing Reviews*, 5(1), 301-10.
- Smits, K. M., Sakaki, T., Howington, S. E., Peters, J. F., and Illangasekare, T. H. (2013). Temperature dependence of thermal properties of sands across a wide range of temperatures (30–70C), *Vadose Zone Journal*, 12(1).
- Smits, K. M., Sakaki, T., Limsuwat, A., and Illangasekare, T. H. (2010). Thermal conductivity of sands under varying moisture and porosity in drainage wetting cycles. *Vadose Zone Journal*, 9(1), 1-9.
- Yao, J., Oh, H., Likos, W.J., and Tinjum, J.M. (2014). Three laboratory methods for measuring thermal resistivity dryout curves of coarse-grained soils, *Geotechnical Testing Journal*, 37(6), 1056-1067.

CHAPTER TWO

BACKGROUND: EXPERIMENTAL TECHNIQUES AND PROCEDURES FOR SOIL THERMAL CONDUCTIVITY MEASUREMENTS

2.1 INTRODUCTION

Since soil thermal conductivity is required to analyze many of the aforementioned engineering problems in Chapter One, it becomes very important to accurately measure thermal conductivity of soils in the laboratory or in situ. There are several experimental techniques available to measure the thermal conductivity of soils in many previous studies (e.g., Kersten, 1949; de Vries, 1952; Bristow et al., 1998). Farouki (1981) provides an overview of experimental techniques including steady-state and transient methods available for measuring thermal conductivity of soils. ASTM International test standard ASTM D5334-08 and Institute of Electrical and Electronics test standard IEEE 442-1981 describe procedures for obtaining soil thermal conductivity measurements using transient thermal probe methods. Previous literature has shown that thermal conductivity of soils is significantly dependent on the water content or degree of pore water saturation (Sepaskhah and Boersma, 1979; Hopmans and Dane, 1986). Measurements of soil thermal conductivity with respect to water content or degree of saturation have become essential in recent studies (Campbell et. al., 1994; Smits et. al., 2010; Likos et. al., 2012; Lu and Dong, 2015). The relationship between thermal conductivity and degree of pore water saturation is often referred as thermal conductivity dry-out curve (TCDC). Campbell (2011) gives an overview of two experimental procedures including single- and multiple-specimen procedures for producing thermal conductivity dry-out curves. Likos et. al. (2012) and Yao et. al. (2014) evaluate and compare several experimental procedures including single- and multiplespecimen procedures, staged-drying procedures and modified hanging column procedures for producing thermal conductivity dry-out curves.

This chapter reviews existing literature on commonly used experimental techniques and procedures for measuring thermal conductivity of soils. This information provides a background to understand the fundamental techniques and procedures for further development of the experiments presented subsequently.

2.2 EXPERIMENTAL TECHNIQUES

There are two broad approaches for measuring thermal conductivity: steady state methods and transient methods. This section reviews commonly used techniques in each method, and provides preliminary comparison of these techniques for specific application to soils.

2.2.1 Steady-state Method

The theoretical basis of most steady-state methods is described by the following equation: $\dot{q} = \lambda \nabla T \tag{2-1}$

where \dot{q} is heat flux density (W·m⁻²), λ is the thermal conductivity (W/m-K), and ∇T is the temperature gradient (K/m). The basic concept of steady-state method is to apply a constant heat flux to soils and monitor the temperatures within the certain distance from the heat source in soils when heat transfer in soils reaches steady state. A common steady-state method is the guarded hot plate method (GHP), which has been standardized as ASTM C177. In the commonly adopted double-sided mode of measurement, two identical test specimens are sandwiched between a main heater that provides a constant heat flux into the specimens and two isothermal cold plates maintained at fixed temperature by a heat sink. The main heater is often surrounded by a gap and concentric guard heater to minimize lateral heat flow within the apparatus. Outer insulation can be

used to reduce heat loss. Mean thermal conductivity of the pair of specimens at steady state is determined from (ASTM C1045):

$$\lambda = \frac{Q}{A[(\Delta T_{S-S}/L)_1 + (\Delta T_{S-S}/L)_2]}$$
 (2-2)

where Q is the rate of heat flow from the main heater (W), A is the specimen area normal to the heat flux (m²), and $\Delta T_{s-s}/L$ is the ratio of surface-to-surface temperature difference to the thickness (L) of specimen 1 and 2 (K·m⁻¹).

2.2.2 Transient Method

Transient methods were developed based on the full heat equation in the form:

$$\rho c_p \frac{\partial T}{\partial t} = \nabla \cdot (\lambda \nabla T) + G' \tag{2-3}$$

where ρc_p is volumetric heat capacity (J·m⁻³K⁻¹), T is temperature (K), t is time (s), λ is thermal conductivity (W·m⁻¹K⁻¹), and G' is heat generation per unit volume (W·m⁻³). A common transient technique is the transient line source (TLS) or heat probe method proposed by Stalhane and Pyk (1931). de Vries (1952) employed a single-needle TLS probe to measure soil thermal conductivity. Bristow *et al.* (1998) developed a dual-needle probe capable of measuring soil thermal diffusivity, volumetric heat capacity, and thermal conductivity. Examples of commercially available single-probe (TLS-SP) and dual-probe (TLS-DP) configurations are shown in Figure 2-1a. Using these approaches, heat energy is emitted from a thin-line heat source (*e.g.*, needle-shaped probe) embedded in the medium. Corresponding temperature response is monitored with a temperature sensor that is either integrated within the heat source (TLS-SP) or within a second probe located some distance from the heat source (TLS-DP). The rate of temperature change in either case depends on the thermal properties of the surrounding medium. For heat diffusing radially from a line source into a homogenous isotropic medium, corresponding temperature response is (Carslaw and Jaeger, 1959; Bristow *et al.*, 1994):

$$\frac{\partial T}{\partial t} = \alpha \left[\frac{\partial^2 T}{\partial r^2} + \frac{1}{r} \left(\frac{\partial T}{\partial r} \right) \right] \tag{2-4}$$

where α is thermal diffusivity (m²/s) and r is the radial distance (m) from the center of the heat source. The corresponding solution for a line source is (de Vries, 1952):

$$\Delta T(r,t) = \begin{cases} -(q/4\pi\lambda)Ei(-r^2/4\alpha t) &, 0 < t \le t_0 \\ (q/4\pi\lambda)\{Ei[-r^2/4\alpha (t-t_0)] - Ei(-r^2/4\alpha t)\}, t > t_0 \end{cases}$$
(2-5)

where ΔT is temperature change (K), q is heat input per unit time per unit length (J·s⁻¹m⁻¹), Ei is the first-order exponential integral operator, and t_0 is the duration (s) of the applied heat pulse. Thermal conductivity is calculated for single-probe or dual-probe configurations by analyzing temperature change as a function of time. Test standards ASTM D5334-08 and IEEE 442-1981 describe procedures to measure soil thermal conductivity using transient line source methods.

Unlike TLS methods, transient plane source (TPS) methods use an embedded planar surface (Figure 2-1b) to generate heating power that diffuses into the surrounding medium (Gustafsson, 1991). Temperature of the sensor surface increases with applied heating power and its electrical resistance [R(T)] changes accordingly:

$$R(T) = R_0[1 + \alpha \overline{\Delta T(\tau)}] \tag{2-6}$$

where R_0 is an initial resistance before heating (Ω) , α is a temperature coefficient of resistivity $(\Omega \cdot K^{-1})$, and $\overline{\Delta T(\tau)}$ is average temperature change as a function of non-dimensional time $(\tau = \sqrt{t/\theta})$, where θ is a characteristic time of the measurement. For conditions of zero contact resistance between the sensor and material, the average temperature change $(\overline{\Delta T(\tau)})$ is:

$$\overline{\Delta T(\tau)} = \frac{G}{\pi^{3/2} r \lambda} D(\tau) \tag{2-7}$$

where G is the total power output (W), r is the sensor radius (for a disk-shaped sensor), and $D(\tau)$ is a shape function. Thermal conductivity can be inversely calculated from the temperature change by measuring corresponding resistive voltage from eq. (2-6).

In contrast to the embedded TPS sensor approach, Mathis (1999) developed a modified transient plane source (MTPS) method using only one side of a planar source to conduct heat into the outer surface of a material. Here the sensor is placed in contact with the material rather than embedded within it, and thus has potential advantages for materials that may be sensitive to disturbance caused by physically inserting a sensing probe. As shown for one commercially available MTPS sensor on Figure 2-1c, a spiral-shaped heater/sensor element with an integrated guard ring generates a transient heat pulse to approximate 1D heat flow into the material. The material adsorbs some of the heat and the rest causes a temperature increase ($\sim 1 - 3$ °C) at the sensor/material interface. For a given heat input, temperature change at the sensor surface [$\Delta T(t)$] is:

$$\Delta T(t) = \frac{1.1284G\sqrt{t}}{e_1 + e_2} \tag{2-8}$$

where e_I and e_2 are the equivalent effusivity $(W \cdot s^{1/2}/m^2K)$ of the sensor and the material, respectively. Corresponding voltage change $[\Delta V(t)]$ is:

$$\Delta V(t) = I \cdot \Delta R(t) = I \cdot \alpha \cdot \Delta T(t) = \frac{1.1284 I \alpha G \sqrt{t}}{e_1 + e_2} = m \sqrt{t}$$
 (2-9)

where m is the slope of the voltage change versus \sqrt{t} . The temperature rise and induced voltage are proportional to the thermal properties of the material. The MTPS sensor may thus be calibrated by measuring 1/m in materials with known effusivity such that the unknown effusivity of a test material can be determined from:

$$\frac{1}{m} = M_1 \cdot e_2 + C_1 \tag{2-10}$$

where M and C are the slope and the intercept of a calibration line between 1/m and known e_2 values, respectively. Since the MTPS sensor is not able to measure volumetric heat capacity (ρc_p) , however, λ cannot be calculated from the relationship between e_2 and λ ($e_2 = \sqrt{\lambda \cdot \rho c_p}$). Alternatively, an iterative algorithm is used in the form:

$$\frac{1}{m-m^*} = M_2 \cdot \lambda + C_2 \tag{2-11}$$

where m^* is a calibration factor found by the iterative process, and M_2 and C_2 are the slope and the intercept of a calibration line for different material groups with known λ .

2.2.3 Preliminary Comparison

Table 2-1 summarizes applicable thermal conductivity ranges for each of the aforementioned sensing techniques and potential advantages and limitations for specific application to soils. Since the GHP technique requires considerable heat input that may potentially cause moisture migration in porous materials, the technique is considered problematic for measuring λ in unsaturated soils (Farouki, 1981; Bristow, 2002). Moreover, the λ range of the GHP technique is limited to approximately 0 to 2 W/m-K, and thus may not be suitable for soils at high saturation, where λ commonly ranges from about 1.5 to 3 W/m-K. Transient methods, on the other hand, are applicable over a range of λ relevant to most unsaturated and saturated soils, but have uncertainties associated with disturbance and sensor-soil contact resistance.

2.3 EXPERIMENTAL PROCEDURES

While no specific approach has yet to have been standardized for measuring TCDCs, several laboratory testing procedures have been developed and applied along drying and wetting paths. These most notably include multiple-specimen method (Campbell, 2011; Likos *et al.*, 2012), the instrumented Tempe cell or modified hanging column methods (e.g., Smits *et al.*, 2010; Likos

et al., 2012), and the staged-drying method (Woodward and Tinjum, 2012). Woodward and Tinjum (2012), Likos et al. (2012) and Yao et. al. (2014) report results from experiments designed to examine influences of issues inherent to each approach, including gravity-induced moisture migration, drying temperature, drying time, sensor location, sensor orientation, and sample heterogeneity.

2.3.1 Multiple-Specimen Procedures

These procedures are performed by direct measurement of thermal conductivity using a single-needle probe inserted into multiple soil specimens compacted to the target void ratio and over a range of water contents. Thermal conductivity for dry soil specimens is first measured by inserting a single-needle probe (TR-1, Decagon Devices, Inc.) into the top center of the compacted soil (vertical probe orientation). The TR-1 sensor is a 10-cm-long, 2.4-mm-diameter, single needle probe used in conjunction with the KD2-Pro transient line source thermal properties analyzer. The dry soil is then poured into a large container, thoroughly mixed with an amount of water to produce target water content, and then re-compacted into the mold for a second thermal conductivity measurement at the target void ratio. Compaction is done in a series of lifts while modifying the effort to achieve specimen volume corresponding to the target void ratio. This is usually repeated for a total of 10-20 compacted specimens having 9-19 water content increments. Water content and corresponding saturation for each increment are determined after each test by sampling soil from the vicinity of the TR-1 probe for gravimetric measurement.

2.3.2 Modified Hanging Column Procedures

In this method, soil-water characteristic curves (SWCCs) and TCDCs can be obtained concurrently along initial drying path from full saturation using an instrumented hanging column apparatus adapted from the design of Smits *et al.* (2010). The hanging column apparatus (Figure

2-2) consists of an acrylic confining cell modified from a commercially available flow cell (Model C1-029B, Soil Measurement Systems, Tucson, AZ), a perforated bottom plate, and a top cap. Dimensions of the cell include an outer diameter of 13.4 cm, wall thickness of 0.7 cm, and height of 8.0 cm. The bottom plate includes a brass screen designed to support a high-air-entry nylon membrane (pore size = 0.2 μ m, air-entry pressure = 340 kPa), through which suction may be applied via an external hanging-column water system (ASTM D6836-02). Sensors are directly embedded in soil to obtain concurrent measurements of matric suction (ψ), degree of saturation (S), temperature (T), and thermal conductivity (λ) as suction is slowly and continuously increased by bottom drainage using the hanging water column, followed by an evaporative drying phase.

The sensor for measuring matric suction (denoted I in Fig. 2-2) is a small-tip tensiometer inserted through a plastic fitting on the side wall of the cell, embedded into the soil, and connected to a differential pressure transducer (Model P55D, Validyne Engineering Corp., Northridge, CA) and data-logger system. The thermal sensor (II) is a dual-needle probe (SH-1) connected to a KD2Pro data-acquisition system (Decagon Devices, Pullman, WA) for measuring soil thermal properties. The SH-1 is a dual-needle probe with two 30-mm long, 1.28-mm diameter probes spaced 6 mm apart, and is capable of measuring thermal conductivity, thermal diffusivity, and volumetric specific heat. The moisture sensor (III) is a dual-prong dielectric moisture sensor (ECH₂O EC-5, Decagon Devices, Pullman, WA) connected to a Decagon Em50 data logger. Raw data acquired from the moisture sensor needs to be independently calibrated for each test material using the two-point α-mixing model approach from Sakaki *et al.* (2008). The temperature sensor (IV) is embedded into the top portion of the soil away from the other sensors and connected to the Em50 data logger.

Dry soil, which is dried in an oven at 105 °C for 24 h, is compacted directly into the confining sleeve in four equal layers to achieve a target void ratio. This results in a typical specimen height of 6.6 cm. The tensiometer, moisture sensor, and SH-1 sensor are embedded in soil between the 2nd and the 3rd layers with horizontal orientation (Figure 2-2). The three sensors are located on the same horizontal plane (within ~0.5 cm vertical offset) such that moisture content, suction, and thermal conductivity measurements could be considered to represent measurements obtained at comparable suction (i.e., at the same elevation above the water level in the hanging column). Sakaki et al. (2008) conducted experiments to show that the bulk sampling volume of the EC-5 moisture sensor is approximately 18 cm³, comprising a 2-cm length parallel to the prongs, a 1-cm length perpendicular to the prongs, and a 9-cm longitudinal length (including the sensor head). Thus, for a horizontally-oriented moisture sensor, the water content measurement represents some average of the material approximately 1 cm above and below the sensor, which corresponds to a difference in suction across the measurement volume of about 0.2 kPa. The water content measurement obtained is thus representative of a vertical region of sand equal to about 30% of the overall specimen height. The temperature sensor is inserted through a vent in the top cap and buried in the top portion of the sand after compacting the 4th layer.

After compacting the dry soil, valve 1 (Figure 2-2) is opened to wet the membrane and specimen from bottom to top until approximately 1 cm water ponded on the top of the soil surface. The water level in the cell and standpipe is then brought down to the midpoint of the cell at the elevation where the tensiometer, moisture sensor, and thermal probe are located. Valve 2 is then partially opened to produce a slow drip from the water column at a rate of 6 to 10 s/drip, thereby slowly and continuously increasing the suction at a corresponding rate of about 0.1 cm/hr (9.8 × 10^{-3} kPa/hr) to 0.5 cm/hr (4.9 × 10^{-2} kPa/hr). After the water in the standpipe is completely drained

at a suction head of ~125 cm H₂O (~12.25 kPa), the hanging column is removed, the top cap of the cell is removed, and a small mechanical fan is set up near the top of the specimen to promote continued drying through evaporation. Matric suction, water content, and thermal conductivity are continuously monitored until volumetric water content reached a value less than about 0.01, or until reliable measurements from the tensiometer could no longer be obtained.

2.3.3 Staged-Drying Procedures

Staged-drying methods for measuring the TCDC generally involve making incremental measurements of thermal conductivity and moisture content for a specimen compacted to some target density at initially high water content and then allowed to dry. Staged-drying results and the required amount of test time depend on the method of drying, boundary conditions (surface exposed to evaporation), drying temperature, soil type, and initial water content. Despite all of these potential effects, no formalized procedures currently exist for constraining these variables in the form of a standardized measurement protocol.

Likos *et al.* (2012) described procedures for TCDC testing of sandy soils that involved embedding a TR-1 probe into a nearly saturated sample placed on an electronic balance and allowed to dry in the ambient laboratory atmosphere. Changes in sample mass (used to calculate moisture content) and thermal conductivity were measured twice per day to produce a TRDC. Woodward and Tinjum (2013) conducted a series of tests designed to investigate potential issues with non-uniform water distribution in staged-drying tests. Cylinders of PVC pipe with an inner diameter of 152 mm and height of 203 mm were used as specimen molds. Soil specimens were compacted into the cylinder in three lifts using Standard compaction effort per ASTM D698. Saturation after compaction ranged from about 45% to 85% depending on soil type. The specimen top was open to the atmosphere and three holes were drilled into the side wall of the cylinder to

insert a horizontally-oriented TR-1 sensor at "top," "middle," and "bottom" locations corresponding approximately to the mid-height of each lift. The same probe was inserted and then removed to make initial λ measurements and periodic λ measurements after placing the specimen in a 50 °C oven for 1 day, 3 days, and 10 days of drying time. Soil was destructively sampled from each sensor location for gravimetric water content determination at the end of each increment, thus requiring three replicate specimens.

Yao et. al. (2014) adopted and modified Woodward and Tinjum (2013) to obtain more consistent target void ratios, to accommodate horizontal three-probe orientation, and to produce more robust results having a larger number of data points on the TCDC. The required amount of water to achieve full saturation at target void ratio was first poured into a chlorinated polyvinyl chloride (CPVC) cylinder (Figure 2-3). Soil was then poured directly into the water through a plastic funnel. This was done in three equal lifts to achieve the target void ratio. Four replicate specimens of the soil were prepared for thermal conductivity and destructive water content measurements at the top, middle, and bottom of the specimen after 1 day, 3 days, 7 days and 10 days of oven drying at 50 °C. Specimens removed for λ measurements at 1, 3, 7, and 10 days were allowed to cool at room temperature for two hours prior to inserting the TR-1 probe. Once inserted, the probe was allowed to equilibrate to the soil temperature for an additional 15 min.

2.3.4 Preliminary Comparison

Yao et. al. (2014) compared three different laboratory approaches, including modified hanging column, staged-drying, and multiple-specimen procedures. Table 2-2 summarizes approximate time to obtain TCDCs using these approaches. The modified hanging column procedures produce the most robust (effectively continuous) TCDC, and has the advantage of concurrently obtaining the soil water characteristic curve (SWCC). Both the TCDC and SWCC

are required for modeling coupled heat and moisture transport in many geotechnical applications. The multiple-specimen approach involving several sub-samples compacted over a range of moisture content required the least amount of time (< 1 day), but produced a far less robust TCDC including an average of about 12 discrete measurement points. There is also uncertainty regarding the effects of compaction-induced changes to soil fabric that should be increasingly important to consider for clay-rich soils. The staged-drying approach adapted from the approach of Woodward and Tinjum (2013) involving incremental oven drying of samples at 50 °C required about 10 days to produce TCDCs containing about 24 discrete measurements. Thermal conductivity values measured using the modified hanging column method at moisture contents greater than critical saturation were consistently lower than values obtained the other two methods. There is then a crossover point such that the modified hanging column method produces thermal conductivity values higher than the other two methods. Potentially high thermal conductivity measurements in the staged-drying apparatus are attributed to elevated temperature (~18 °C - 46 °C) compared with the other two methods (~23 °C - 24 °C). Potentially low thermal conductivity measurements obtained using the modified hanging column method are attributed to potential errors associated with moisture movement exacerbated by high hydraulic conductivity. Potentially low thermal conductivity obtained using the multiple-specimen and staged-drying methods at low saturation are attributed to errors associated with contact resistance and sample disturbance exacerbated for dry soils.

2.4 SUMMARY

This chapter provides a thorough review of experimental techniques and procedures for measuring thermal conductivity of unsaturated soils. The reviewed experimental techniques included steady-state method (e.g., guarded hot plate method) and transient sensor techniques (e.g.,

transient line source, transient plane source and modified transient line source methods). The reviewed experimental procedures include multiple-specimen, modified hanging column and staged-drying methods. These reviews will help to develop further experimental programs for proposed studies.

2.5 REFERENCES

- ASTM. (2013). "Standard test method for steady-state heat flux measurements and thermal transmission properties by means of the guarded-hot-plate apparatus." *C177-13*, West Conshohocken, PA.
- ASTM. (2013). "Standard practice for calculating thermal transmission properties under steady state conditions." *C1045-07*, West Conshohocken, PA.
- Bristow, K. L. (2002). "Thermal conductivity." *Methods of soil analysis. Part 4. Physical methods, soil science society of America book* series, 5, J. H. Dane and G. C. Topp, eds., Soil Society of America, Madison, WI.
- Bristow, K. L. (1998). "Measurement of thermal properties and water content of unsaturated sandy soil using dual-probe heat-pulse probes." *Agric. For. Meteorol.* 89(2), 75-84.
- Bristow, K. L., Kluitenberg, G. J., and Horton R. (1994). "Measurement of soil thermal properties with a dual-probe heat-pulse technique." *Soil Sci. Soc. Am. J.*, 58(5), 1288-1294.
- Campbell, G. S. (2011), "Producing Thermal Dryout Curves for Buried Cable Applications."

 Application Note 13994-01 AN, Decagon Devices, Inc., Pullman WA.
- Campbell, G.S., Jungbauer, J.D., Bidlake, W.R., and Hungerford, R.D. (1994). "Predicting the Effect of Temperature on Soil Thermal Conductivity." Soil Science, 158(5), 307-313.
- Carslaw, H.S. and J.C. Jaeger, (1959). *Conduction of Heat in Solids*. 2nd Edition. Oxford, London.

- de Vries, D. A. (1952). "A nonstationary method for determining thermal conductivity of soil in situ." *Soil Sci.*, 73(2), 83-90.
- Farouki, O. T. (1981). *Thermal Properties of Soils* (No. CRREL-MONO-81-1). COLD REGIONS RESEARCH AND ENGINEERING LAB HANOVER NH.
- Gustafsson, S. E. (1991). "Transient plane source techniques for thermal conductivity and thermal diffusivity measurements of solid materials." *Rev. Sci. Instrum.*, 62(3), 797-804.
- Hopmans, J.W., and Dane, J.H. (1986). "Thermal Conductivity of Two Porous Media as a Function of Water Content, Temperature, and Density." *Soil Science Society of America Journal*, Vol. 142 (4): 187-195.
- Kersten, M. S. (1949). *LABORATORY RESEARCH FOR THE DETERMINATION OF THE THERMAL PROPERTIES OF SOILS*. MINNESOTA UNIV MINNEAPOLIS ENGINEERING EXPERIMENT STATION.
- Likos, W. J., Olson, H. S., and Jaafar, R. (2012). "Comparison of Laboratory Methods for Measuring Thermal Conductivity of Unsaturated Soils." *GeoCongress* 2012
- Lu, N. and Dong, Y. (2015). "Closed-Form Equation for Thermal Conductivity of Unsaturated Soils at Room Temperature." *J. Geotech. Geoenviron. Eng.*, 10.1061/(ASCE)GT.1943-5606.0001295, 04015016.
- Mathis, N.E., (1999). "New transient non-destructive technique measures thermal effusivity and diffusivity." *Proc.*, *25th International thermal conductivity conference*, Technomic Publishing Co., Lancaster, PA, 3-14.
- Sakaki, T., Limsuwat, A., Smits, K. M., and Illangasekare, T. H. (2008). "Empirical Two-Point A-Mixing Model for Calibrating the ECH2O EC-5 Soil Moisture Sensor in Sands." *Water Resources Research*, 44(4).

- Sepaskhah, A. R., and Boersma, L. (1979). "Thermal conductivity of soils as a function of temperature and water content." *Soil Sci. Soc. Am. J.*, *43*(3), 439-444.
- Smits, K. M., Sakaki, T., Limsuwat, A., and Illangasekare, T. H. (2010). "Thermal Conductivity of Sands under Varying Moisture and Porosity in Drainage Wetting Cycles." *Vadose Zone Journal*, *9*(1), 1-9.
- Stalhane, B., and Pyk, S. (1931). "New method for determining the coefficients of thermal conductivity." *Tek. Tidskr.*, 61(28), 389-393.
- Woodward, N. R., Tinjum, J. M., and Wu, R. (2013). "Water migration impacts on thermal resistivity testing procedures," *Geotechnical Testing Journal*, Vol. 36, No. 6, pp. 1-8.
- Woodward, N. R. and Tinjum, J. M. (2012). "Impact of Moisture Migration on Thermal Resistivity

 Testing in Unsaturated Soil." *GeoCongress 2012*
- Yao, J., Oh, H., Likos, W.J., and Tinjum, J.M. (2014). "Three laboratory methods for measuring thermal resistivity dryout curves of coarse-grained soils," *Geotechnical Testing Journal*, 37(6), 1056-1067.

2.6 TABLES

Table 2-1. Comparison of five techniques for measuring soil thermal conductivity

Technique	Methodology	Advantage	Potential Limitation	λ Range (W/m-K)
GHP	Steady-state	 No calibration needed; May use for large sample containing gravels 	 Labor intensive; Longer testing time; May have uncertainties due to moisture migration when testing unsaturated samples. 	
TLS	Transient	 Easy to use; Require less testing time; Minimal moisture redistribution due to small heat output and relative low heating time. 	 Difficult to test samples containing gravel; Probe insertion may cause disturbance to samples May have uncertainties due to contact resistance between sensor and sample 	0.1 to 4.0 ^b
TPS	Transient	 Require less testing time; May use for large sample test; Can test heterogeneous and anisotropic sample. Non-destructive 	May have uncertainties due to contact resistance between sensor and sample Relatively Higher cost	0.005 to 1800°
MTPS	Transient	 Easy to use; Require very small testing time; Require less sample preparation time Non-destructive 	 May have uncertainties due to contact resistance between sensor and sample Difficult to test samples containing gravel; Sensor surface may be fragile. 	0 to 500 ^d

^aFrom Yüksel (2016).

^bFrom Decagon Devices, Inc.

^cFrom Thermtest, Inc.

^cFrom C-Therm Technologies, Ltd.

Table 2-2. Comparison of approximate time to obtain TCDCs

Test Method	Modified Hanging Column (h)	Staged-drying (h)	Multiple-specimen (h)
Preparation time	2	2	2
Testing time	539 ^a	240	2
Total time	541	242	4

^aTotal test time required for drainage phase (96 h) and evaporation phase (443 h).

2.7 FIGURES

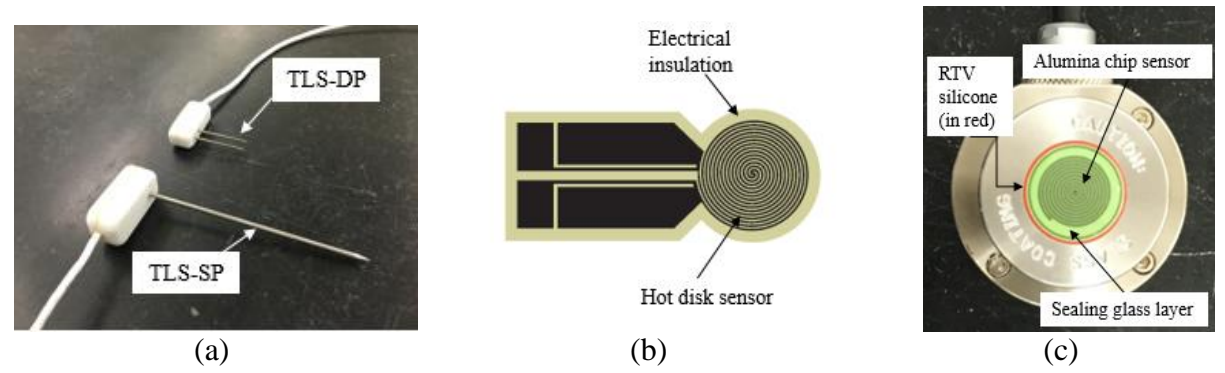


Figure 2-1. Transient sensing techniques: (a) TLS sensors in TLS-SP (single probe) and TLS-DP (dual probe) configuration; (b) TPS sensor (Krupa and Malinarič, 2014); (c) MTPS sensor.

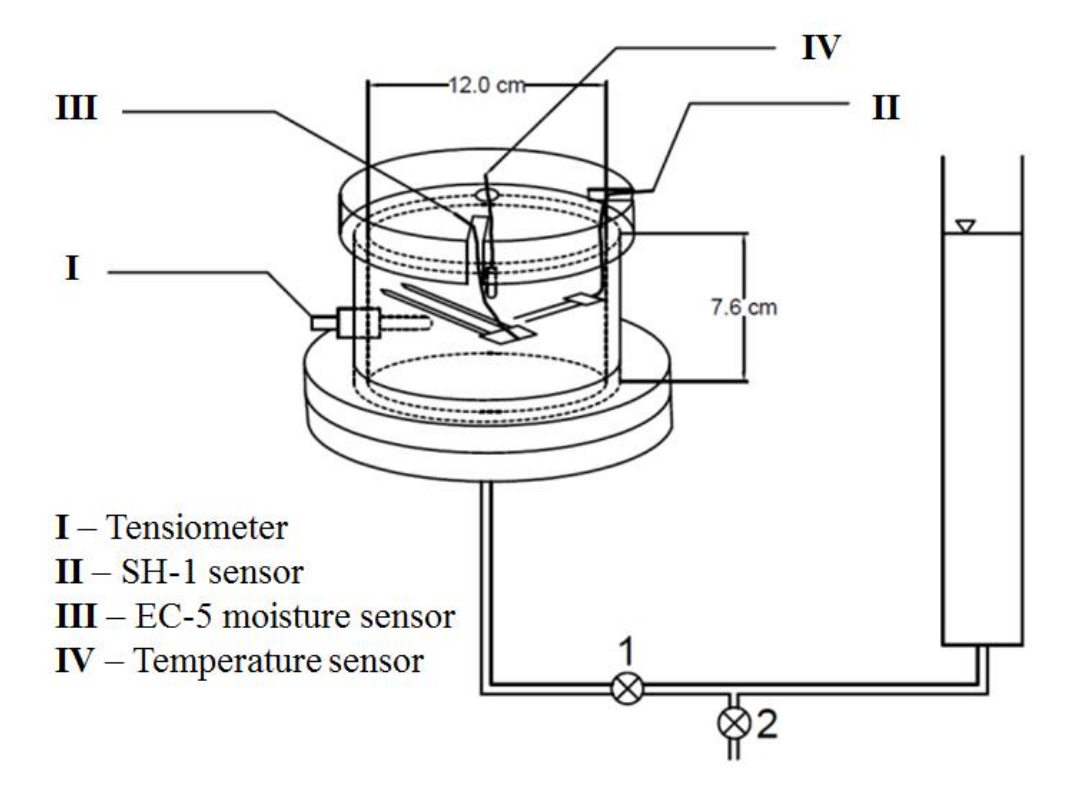


Figure 2-2. Schematic of modified hanging column apparatus (after Smits et al. 2010).

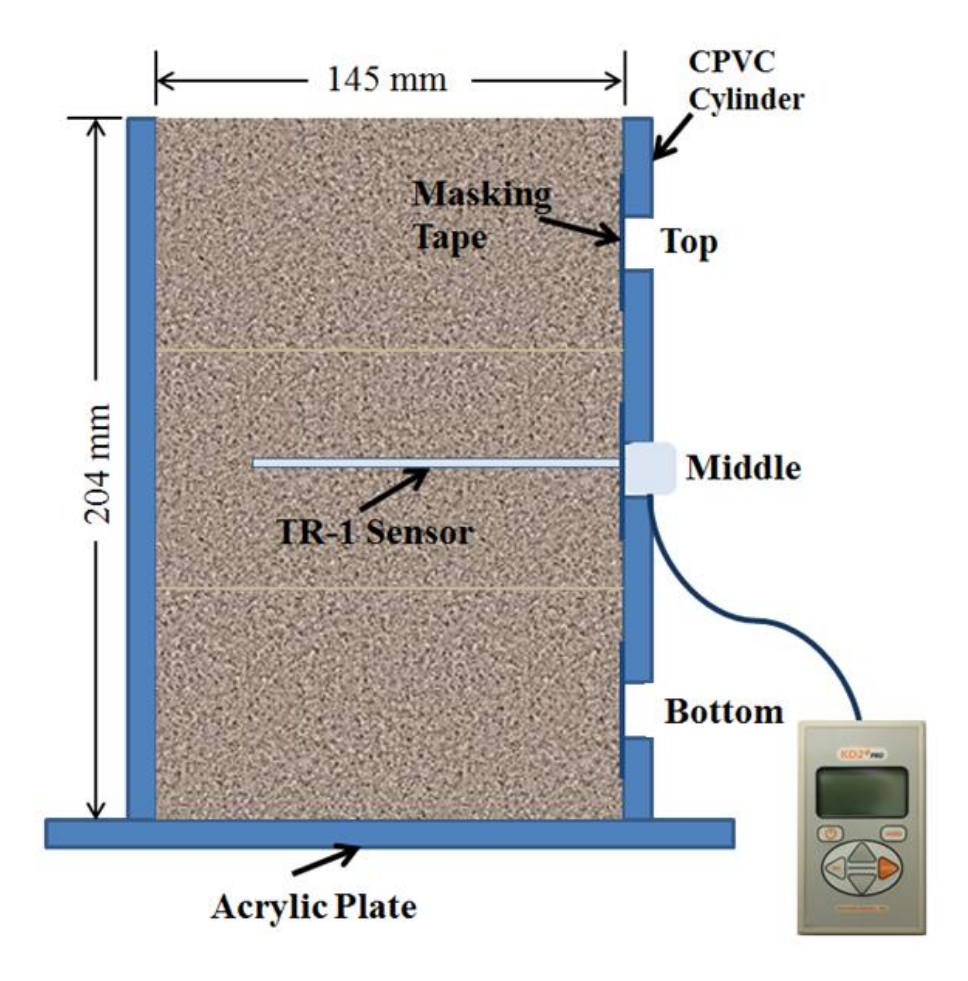


Figure 2-3. Schematic of staged-drying test apparatus (after Woodward and Tinjum, 2013).

CHAPTER THREE

TRANSIENT PLANE AND LINE SOURCE METHODS FOR SOIL THERMAL CONDUCTIVITY

ABSTRACT: Experiments were conducted to compare two sensing techniques for measuring thermal conductivity of unsaturated soils: (i) a modified transient plane source (MTPS) method for non-destructive measurements using a planar, interfacial heat reflectance sensor; and (ii) a transient line source (TLS-SP) method utilizing an embedded single-probe heat source. Measurement protocols for coarse-grained and fine-grained soils were developed. Thermal conductivity dry out curves (TCDCs) were measured for five soil types, including poorly-graded sand, well-graded sand with silt, silty sand, silt, and clay. The MTPS sensor consistently produced higher thermal conductivity for degrees of saturation greater than about 50%, but lower thermal conductivity for saturations less than 50%. Saturated thermal conductivity measured using the MTPS sensor ranged from 8% to 26% greater than values measured using the TLS-SP sensor. Dry thermal conductivity measurements were comparable (< 5% difference) for fine-grained soils, but were consistently and appreciably greater using the TLS-SP for coarse-grained soils. Mechanisms responsible for these differences include thermally-induced water migration, latent heat transfer, sensor-soil contact resistance, gravity-induced water migration, and specimen heterogeneity. Secondary experiments indicated that the effects of gravity-induced water migration were insignificant within the short (< 5 min) time frame elapsed between sample preparation and measurement.

3.1 INTRODUCTION

Soil thermal properties are important in many geotechnical engineering applications, including backfill design for buried power cables, nuclear waste repositories, energy piles, ground-

source heat exchangers, and subsurface thermal energy storage systems. Soil thermal properties are not constant, but rather may change appreciably with changes in soil structure from applied stress or with changes in pore fluid saturation (*S*) from wetting and drying. The effects of changes in saturation are often the most appreciable given the large contrast in the thermal properties of the solid, liquid, and gas phases, and because changes in saturation can readily occur in the near-surface soil environment (*e.g.*, Farouki, 1981).

The three primary mechanisms for heat transfer through soils include conduction, radiation, and convection. While radiation or convection can be important in saturated or unsaturated soils of relatively large grain size ($D_{10} \approx 10$ mm) or in hydrogeological settings marked by significant fluid flow, conduction is the dominant heat transport mechanism for most sand, silt, and clay-sized materials over a wide range of saturation and settings (Johansen, 1975; Fillion *et al.*, 2011). Pathways for heat conduction include direct conduction through the soil solids, which depends primarily on mineralogy of the solid phase, direct conduction through the pore fluids (*i.e.*, air or water), which depends on the thermal conductivity of each fluid, conduction through solid-solid contacts, which depends on grain size distribution, contact resistance, and porosity, and conduction through solid-fluid-solid bridges, which is important for unsaturated soils and depends primarily on the soil-water retention characteristics and degree of saturation (*e.g.*, Yun and Santamarina, 2008).

Fourier's law and the first law of thermodynamics govern one-dimensional heat conduction in a material:

$$\rho c_p \frac{\partial T}{\partial t} = \nabla \cdot (\lambda \nabla T) + G' \tag{3-1}$$

where ρc_p is volumetric heat capacity (J·m⁻³K⁻¹), T is temperature (K), t is time (s), λ is thermal conductivity (W·m⁻¹K⁻¹), and G' is heat generation per unit volume (W·m⁻³). Volumetric heat

capacity is a measure of a material's ability to store heat, while thermal conductivity is a measure of a material's ability to conduct heat. These properties depend on many factors for soils, including mineralogy, particle shape, particle and pore microstructure, bulk density, moisture content, and temperature (e.g., de Vries, 1963; Shiozawa and Campbell, 1990). In unsaturated soils, latent heat transfer from water vaporization and condensation at air-water interfaces can also be an important factor, particularly at low saturation ($S < \sim 0.40$) or at elevated temperatures ($T > \sim 40$ °C to 50°C) (e.g., Campbell et~al., 1994; Shahraeeni and Or, 2012; Smits et~al., 2013). These effects are often captured using an effective thermal conductivity that includes the combined effects of direct heat conduction and latent heat transfer.

For a homogenous and isotropic material under conditions of no heat generation, eq. (3-1) can be simplified to the steady state form:

$$\dot{q} = \lambda \nabla T \tag{3-2}$$

where \dot{q} is heat flux density (W·m⁻²) and λ becomes the predominant material property governing heat conduction. Thermal conductivity of typical soil solids varies from about 1.0 W·m⁻¹K⁻¹ to 9.0 W·m⁻¹K⁻¹ depending on mineralogy, whereas λ for water and air are 0.6 W·m⁻¹K⁻¹ and 0.025 W·m⁻¹K⁻¹, respectively (*e.g.*, Farouki, 1981). Changes in the relative volume fraction of each phase can thus significantly affect bulk thermal conductivity of the multiphase unsaturated soil system. The corresponding relationship between λ and S, which is referred to herein as the thermal conductivity dry-out curve (TCDC), is an important constitutive function for problems involving heat transport in unsaturated soils. A large number of experimental, analytical, and computational approaches for measuring or estimating the TCDC have been explored (*e.g.*, Farouki, 1981; Campbell *et al.*, 1994; Côté and Konrad, 2005; Smits *et al.*, 2010; Likos, 2014a, 2014b; Yao *et al.*, 2014; Lu and Dong, 2015).

This section presents results from laboratory experiments conducted to compare two sensing techniques for measuring thermal conductivity and the TCDC of unsaturated soils: (*i*) a modified transient plane source (MTPS) method for non-destructive measurements using a planar, interfacial heat reflectance sensor; and (*ii*) a transient line source (TLS-SP) method using an embedded single-probe heat source. Thermal conductivity and thermal conductivity dry out curves (TCDCs) are measured and compared for five representative soil types, including poorly-graded sand, well-graded sand with silt, silty sand, silt, and clay. Advantages and limitations are identified and recommendations for measuring TCDCs using each sensor and for different soil types (coarse-grained and fine-grained) are provided.

3.2 MATERIALS AND METHODS

3.2.1 Test Materials

Three coarse-grained soils and two fine-grained soils were selected for comparison of TCDCs measured using TLS-SP and MTPS sensors. The three coarse-grained soils included poorly-graded sand (SP), silty sand (SM) and well-graded sand with silt (SW-SM). The SP and SM were natural soils obtained from the University of Wisconsin-Madison soils bank (Bareither *et al.*, 2008). The SW-SM was prepared by mixing sand with silt-sized fines. The two fine-grained soils included low-plasticity clay (CL) and silt with sand (ML). These were natural soils obtained from field sites associated with the United States Environmental Protection Agency's (USEPA) Alternative Cover Assessment Program (ACAP) (Gurdal *et al.*, 2003).

Table 3-1 summarizes grain size and index properties including D_{50} , D_{10} , coefficient of uniformity (C_u) , coefficient of curvature (C_c) , fines content, solid specific gravity (G_s) , liquid limit (LL), plastic limit (PL), plasticity index (PI = LL-PL), and maximum dry density (γ_{dmax}) . Grain-size distribution (GSD) curves were obtained from mechanical sieve analysis and are plotted as

Figure 3-1. For soils containing more than 5% fines, the portion passing the No. 40 sieve was sampled for PL and LL tests according to ASTM D4318. Specific gravity (G_s) and maximum dry density (γ_{dmax}) were determined according to ASTM D854 and ASTM D698, respectively. Figure 3-2 is a plot of soil-water retention curves (SWRC) in the form of matric suction (ψ) versus S_s . SWRCs for the coarse-grained soils were obtained using an instrumented Tempe Cell apparatus (Yao *et al.*, 2014). The SWRCs for the fine-grained soils were constructed from van Genuchten (1980) modeling parameters (S_r , α , n, and m) reported by Gurdal *et al.* (2003), as summarized on Table 3-1. The VG model is in the form:

$$\frac{S - S_r}{1 - S_r} = \left[\frac{1}{1 + (\alpha \psi)^n}\right]^m \tag{3-3}$$

where residual saturation S_r , n, and m are empirical fitting parameters optimized to best fit the experimental data.

3.2.2 TCDC Measurement Sensors and Approaches

Commercially available MTPS and TLS-SP sensors were used to measure TCDCs of the test soils. Table 3-2 is a summary of manufacturer-reported specifications for each sensor. The active sensing area of the MTPS sensor was 1.7 cm in diameter and required that the surface of the test material be smooth. The TLS-SP probe was 0.24 cm in diameter and 10 cm in length and could be inserted directly into relatively soft soils or into a pre-drilled pilot hole for hard soils. Thermal grease was applied to both sensor surfaces to minimize errors from contact resistance between either the MTPS and the soil surface or the TLS-SP needle and the surrounding soil.

While no specific approach has been standardized for measuring TCDCs of soils, a variety of multiple-specimen (Campbell, 2011), staged-drying (Steinmanis, 1982; Salomone and Kovacs, 1983), and instrumented cell approaches (*e.g.*, Smits *et al.*, 2010; Yao *et al.*, 2014) have been

demonstrated. Woodward *et al.* (2013) and Likos *et al.* (2012) report results from experiments designed to examine issues inherent to such approaches, including moisture migration induced by gravity, pressure, or temperature, drying temperature, drying time, sensor location, sensor orientation, and sample heterogeneity.

Procedures for measuring TCDCs of the fine-grained soils (CL, ML) followed a single-specimen staged-drying approach, where λ for a saturated specimen was first obtained, followed by incremental measurements as the specimen was allowed to dry. Procedures for the coarse-grained soils (SP, SW-SM, SM) followed a multiple-specimen approach, where several subsamples were compacted to different saturations and used to obtain individual measurements of λ and construct the TCDC. In general, the single-specimen approach requires longer test durations to accommodate the incremental drying process (several days or weeks), but results in a TCDC along a well-defined drying path for a single undisturbed specimen. Although the multiple-specimen approach can be completed in one day, the TCDC data set can be relatively sparse (depending on the number of subsamples), the different compaction water contents among the subsamples introduces potential alterations to soil fabric, and it can be difficult to compact each subsample to the same target density (e.g., Woodward et al., 2013).

Following the multiple-specimen testing approach for the three sands, oven-dry (105 °C) soil was first compacted by hand into a 1000-cm³ beaker at a target void ratio (e_{test}) of either 0.40 or 0.60 (Table 3-1). Compaction was done in four lifts while modifying the effort to achieve a total specimen volume of 1000 cm³ at the target void ratio. The MTPS sensor was placed on top of the soil surface and a 500 g weight was placed on the top of the sensor to enforce better contact (Figure 4a). The sensor was connected to a controller unit and data acquisition system for measuring λ using a material calibration built into the system software. The MTPS sensor was then removed,

and the TLS-SP probe was inserted vertically into the soil at the center of the location where the MTPS sensor was previously placed. The dry sand was then poured into a larger container, mixed with a carefully controlled amount of water to reach target water content, and then re-compacted into the beaker to the same void ratio for another series of measurements using both sensors. This was typically repeated for a total of nine subsamples, including a final measurement at 100% saturation. Soil from the vicinity of the MTPS and TLS-SP sensors was sampled for gravimetric water content determination immediately after each measurement. Deviation in void ratio among the subsamples was within $\pm 5\%$. The dimensions of the test container were selected following manufacturer recommendations to allow a minimum of 1.5 cm of material parallel to the TLS-SP sensor in all directions.

Staged-drying procedures for the fine-grained soils were slightly different for measurements made using the two sensors. For measurements using the TLS-SP sensor, moist soil was first prepared by mixing it with enough water to achieve optimum water content and sealed in a plastic bag for 24 hours. The soil was then compacted to reach maximum dry density and corresponding target void ratio, which ranged from 0.58 to 0.67 depending on the soil (Table 3-1). The specimen and compaction mold were then submerged in de-aired water under vacuum to reach saturation. The TLS-SP sensor was inserted vertically into the center of the compacted specimen to obtain the first thermal conductivity measurement. The specimen and mold were then placed into a 60 °C oven without removing the probe, removed from the oven every 24 hours, and allowed to cool to room temperature before measuring thermal conductivity and the incremental change in mass due to drying.

For staged-drying measurements using the MTPS sensor, the soil was first compacted and saturated following the same procedures as above, but then carefully cut into a cylindrical sub-

specimen with 3.5-cm diameter and 0.5-cm thickness. Because the sampling volume of the MTPS sensor is very small, use of a thin specimen was considered necessary to minimize the effects of non-uniform evaporative drying at the surface. The sub-specimen was placed directly in contact with the MTPS sensor surface and a 500-g weight was placed on top of the specimen to enhance contact (Fig. 3-3b). Thermal conductivity and corresponding water content were measured along a subsequent drying path by allowing the assembly to air-dry for timed increments of 0.5, 1, 2, 4, 8, 16, 24, and 48 hours. After the 48-h increment, the assembly was placed in a 60 °C oven for another 48 hours to obtain a final λ measurement after allowing the specimen to cool to room temperature.

3.3 RESULTS AND DISCUSSION

3.3.1 Measured Thermal Conductivity Dry-out Curves

Figure 3-4 is a series of TCDCs measured using the MTPS and TLS-SP sensors for the five soils. General characteristics of each TCDC are comparable to observations made in previous studies for coarse-grained and fine-grained soils (*e.g.*, Sepaskhah and Boersma, 1979; Smits *et al.*, 2010; Lu and Dong, 2015). Table 3-3 summarizes λ at saturation (λ_{sat}) and λ under dry conditions (λ_{dry}) measured using the two sensors, along with averages from the two measurements. The parameters S_f and m reported on Table 3-3 are modeling parameters optimized to best fit the measured TCDCs according to the model proposed by Lu and Dong (2015) in the form:

$$\frac{\lambda - \lambda_{dry}}{\lambda_{sat} - \lambda_{dry}} = 1 - \left[1 + \left(\frac{S}{S_f}\right)^m\right]^{1/m - 1} \tag{3-4}$$

where S_f is the degree of saturation at the onset of the funicular regime and m is a pore fluid connectivity parameter. Optimizations of eq. (3-4) to the measured TCDC data are included on Figure 3-4. Mathematically, S_f represents the inflection point in a sigmoidal-shaped TCDC and m

captures the rate of change in λ with saturation (Lu and Dong, 2015). For the series of soils considered here, the coefficient of determination (R^2) quantifying the goodness of fit to the experimental data was not less than 0.942.

As shown on Figure 3-4, thermal conductivity for each soil is a maximum under saturated conditions (λ_{sat}). Average values of λ_{sat} from the two sensors ranges from 1.79 W/m-K to 3.28 W/m-K, with lower values corresponding to the fine-grained soils. This observation is attributed to the lower λ of typical clay minerals ($\lambda \sim 2.92$ W/m-K), which is about one third of that of quartz comprising most sandy soils ($\lambda \sim 8.8$ W/m-K) (de Vries, 1963; Campbell, 1985). As saturation decreases, λ decreases in a manner that generally mirrors the sigmoidal shape of the soil-water retention curves (Fig. 3-2). There are three saturation regimes defining a typical SWRC for soil along a path of decreasing saturation: (i) a capillary regime at relatively low suction where the soil remains effectively saturated; (ii) a funicular regime at intermediate saturation characterized by an unsaturated yet continuous water phase; and (iii) a pendular regime at low saturation characterized by an isolated and discontinuous water phase. For clayey soils, an additional water-retention regime dominated by short-ranged hydration of the mineral surfaces at high matric suction also becomes important.

Conceptually, the TCDCs for soil reflects these soil-water retention regimes (Likos, 2014a; Lu and Dong, 2015). Thermal conductivity at saturation and in the capillary regime is at a maximum because heat is transmitted largely through saturated grain-water-grain pathways and the effect of any small volume of air, which is likely to exist in the form of occluded bubbles, does not substantially reduce the effective heat transfer (Smits *et al.*, 2009). Thermal conductivity in the funicular regime decreases because the more conductive liquid phase is displaced by a less conductive gas phase. Here the grain-water-grain heat transfer paths decrease and heat also flows

through the less conductive grain-air-grain paths. At even lower saturation, λ can decrease sharply at some critical saturation (S_{crit}), which may be interpreted to reflect transition into the pendular water retention regime. Because the liquid phase at this point is no longer continuous, heat transport is dominated by relatively weak conduction through grain-to-grain contacts and through diminishing grain-water-grain contacts formed by isolated interparticle liquid bridges. Additional loss of latent heat transport may occur due to reduced recirculation of evaporated water, which further decreases the effective heat transfer (Campbell et al., 1994). At saturations less than S_{crit} , λ reaches a minimum value ultimately corresponding to dry conditions λ_{dry} . Dry thermal conductivity depends primarily on mineralogy of the solid phase and porosity, and can be significantly affected by contact resistance among particles. For the soils considered here, λ_{dry} for the fine-grained soils is appreciably higher than for the coarse-grained soils (Table 3-3), despite what is likely a lower thermal conductivity of clay minerals comprising the solid fraction. Higher conductivity observed for the fine-grained soils is thus potentially attributable to less contact resistance among the solid grains and between the sensor surface and soil (i.e., smaller grains result in a smoother sensor-soil interface), as well as to the presence of adsorbed water films that remain at very low saturation from the high surface area and activity of the clay mineral surfaces (e.g., Lu and Dong, 2015).

Critical saturation for the three coarse-grained soils (Fig. 3-4) varies from about 0.10 to 0.30, which is within the range commonly observed for sands (*e.g.*, Smits *et al.*, 2010; Likos, 2014b). Critical saturation for the fine-grained soils appears to be much higher, but is not obvious because the reduction in thermal conductivity with saturation is more gradual, most notably for the CL soil (Fig. 3-4d). Larger and less-well defined critical saturation for the fine-grained soils reflects their higher surface area, adsorbed water on the mineral surfaces, and generally larger

variability in pore size and geometry compared to sandy soils, which is also reflected in the water retention curves (Lu and Dong, 2015). Overlap between water retention dominated by short-range surface adsorption and by capillary condensation in larger pores is expected to extend to relatively high saturation (perhaps $S \sim 0.5$) for clayey materials, and thus results in a more gradual transition of thermal conductivity. Results from Lu and Dong (2015) for 25 soil types indicate that higher values of the modeling parameters m and S_f are weakly correlated to clay content, which is consistent with what is observed here (Table 3-3).

3.3.2 Sensor Comparison

Comparison of the TCDCs obtained using the MTPS and TLS-SP sensors indicates that measured λ can be appreciably different and that these differences are systematic. Saturated thermal conductivity measured using the MTPS sensor for all five test soils ranges from 8% to 26% greater than λ_{sat} measured using the TLS-SP sensor. The MTPS sensor produces higher λ than the TLS-SP sensor for S greater than about 0.5, but lower λ for S less than about 0.5. This trend is most evident for the three coarse-grained soils but is also observed to a lesser extent for the CL soil. Differences between sensor measurements for the ML soil are the most appreciable, but as described subsequently, this is potentially attributable to desiccation cracking of the thin specimen that was observed during the staged-drying test using the MTPS sensor. Dry thermal conductivity λ_{dry} measured using the TLS-SP sensor is consistently and significantly greater (90% - 215%) than values measured using the MTPS sensor for the three coarse-grained soils, but the difference is less than 5% for the two fine-grained soils.

Figure 3-5 is a comparison of λ measurements at the same saturations using the MTPS and TLS-SP sensors. It is evident that the λ values from MTPS sensor are generally greater than those from TLS-SP sensor in zone 1, which exclusively includes results (closed circles) for coarse-

grained soils at relatively high saturation (S > 0.5). Results from the MTPS sensor become consistently lower than the TLS-SP sensor in zone 3, which exclusively includes results for both coarse-grained and fine-grained soils (closed triangles and closed squares) at low saturations (S < 0.2 for coarse-grained soils and S < 0.5 for fine-grained soils). Finally, zone 2 includes results for fine-grained soils at high saturations (S > 0.5) and coarse-grained soils at intermediate saturations (S < 0.5) and there are no systematic differences observed between the two sensors.

There are a number of potential reasons for the differences observed between the MTPS and TLS-SP sensors. These include the effects of thermally-induced water migration, latent heat transfer, contact resistance, gravity-induced water migration, and specimen heterogeneity. Longer heating times and higher temperatures change can be advantageous for transient heat pulse methods (i.e., both sensor types considered here) because larger temperature changes can be more precisely resolved, are less sensitive to drift, and are less sensitive to contact resistance, but can result in thermally-induced fluid migration from the sensing volume that can change thermal properties of the material being measured. Lower λ evident in the TCDCs from the TLS-SP sensor at high saturation for the soils considered here can potentially be attributed to thermally-induced migration of water away from the sensor and corresponding reduction in λ because the maximum heating temperature change (ΔT_{max}), and pulse time of TLS-SP sensor (~150 s) is higher than that of MTPS sensor (~3 s), although this has not been confirmed experimentally. It should also be noted that thermally induced water flow may occur at different rates and magnitudes for different soils and depend on the initial degree of soil saturation. Figure 3-6 displays the relationship between ΔT_{max} and S for TLS-SP and MTPS sensors for three coarse-grained soils. The value of ΔT_{max} increases with S, and is higher with the TLS-SP sensor than the MTPS sensor at the same S, most significantly at low saturation (S < 0.2). For coarse-grained materials that are relatively dry,

latent heat transfer may also give rise to higher thermal conductivity if the heat input is relatively large. This effect could potentially cause overestimation of λ using the TLS-SP sensor for the sandy soils at low saturation, which is what is observed here, but the importance of this mechanism has also not been confirmed.

Both sensing methods rely on good thermal contact between the sensor and soil. For granular materials, good thermal contact is generally less of an issue closer to saturation, but in dry granular materials, particularly for materials with relatively large grain sizes, contact resistance from an air phase distributed within discrete solid contacts can lead to lower effective thermal conductivity. The lower measurements of λ obtained using the MTPS sensor for saturations less than about 50% are potentially attributable to contact resistance caused by air pockets between the soil and the planar sensor surface. The difference is most notable for the sandy soils, where larger air pockets would be expected to develop in the predominantly larger pores. Although a thin layer of thermal grease was applied to the surface of both sensors, a thicker layer of thermal grease may be required to more effectively fill the open pores on rough soil surfaces. For the MTPS sensor, however, a thicker layer of grease could potentially cause significant error because the MTPS sensing volume is very small (i.e., the grease would comprise a larger portion of the sensing volume). Differences observed between the MTPS and TLS-SP sensors for the fine-grained soils below about 50% saturation are similar to those observed for the coarse-grained soils, but are comparatively small. This could be because even the thin layer of thermal grease that was applied to the sensor surfaces may have sufficiently improved thermal contact between the relatively smooth surface of the clay and the sensor surface. The large differences between the MTPS and TLS-SP results observed for the ML soil (Fig. 3-4e) are likely due to surface cracking that was

observed during drying, which would be expected to cause underestimation of λ for the MTPS sensor placed in contact with large air voids on the cracked surface.

The effects of gravity-induced water redistribution and specimen heterogeneity (e.g., density variation) may also be responsible for observed differences between the TLS-SP and MTPS sensors. A sensor inserted vertically into a specimen (e.g., the TLS-SP) may be in contact with soil over a range of water contents due to downward migration of water with time (e.g., Woodward et al., 2013). Thermal conductivity of the drier soil within the upper portion of the specimen could thus be lower than that of the more moist soil within the lower portion of the specimen. Gravity-induced water redistribution would be expected to be more significant for coarse-grained soils, both because their water retention characteristics result in a larger range of water content over a narrow range of suction (specimen height) and because their higher hydraulic conductivity, especially at higher saturations, would lead to more rapid water redistribution that could occur between the time of specimen preparation and the time of measurement. In addition, insertion of the TLS-SP sensor may cause more local disturbance of density within the specimen than non-destructive placement of MTPS sensor. Therefore, specimen heterogeneity in terms of density can potentially cause the differences between the TLS-SP and MTPS sensors. Heterogeneity and anisotropy induced during the sample preparation (e.g., layering in compacted samples) may also result in bias for horizontal heat transfer and vertical heat transfer, which could have different implications to the MTPS sensor, where heat transfer is primarily vertical, and the TLS-SP sensor, where heat transfer is primarily horizontal.

If gravity-induced moisture migration had a significant effect on the MTPS and TLS-SP measurements, then thermal conductivity values obtained using the MTPS sensor for the coarse-grained soils might be expected to be relatively low since the measurements were made by placing

the sensor on the top of the specimen. The TLS-SP measurements, on the other hand, would effectively represent an average thermal conductivity along the length of the vertically inserted probe. The fact that the MTPS results are consistently larger than the TLS-SP results at higher saturation, however, suggests that either gravity-induced moisture migration was not significant, that there is another mechanism responsible for the observed differences, or that there is an inherent bias in results obtained using each approach.

A secondary set of experiments was conducted to examine time-dependent changes to thermal conductivity measured using the MTPS sensor placed on a top soil surface. Measurements were taken for three specimens of the SP test soil prepared to three different target saturations and monitored for up to one hour after sample preparation. Figure 3-7 shows measured changes in thermal conductivity for specimens initially prepared to average degrees of saturation of 0.3, 0.5, and 0.8. The initial λ at the top surface of the specimen prepared to S = 0.3 was 2.924 W/m-K and decreased to 2.919 W/m-K after one hour, a difference of less than 0.2%. Initial λ for the specimen prepared to S = 0.5 was 1.833 W/m-K and decreased to 1.765 W/m-K, a difference of 3.7%. Initial λ for the specimen prepared to S = 0.8 was 1.368 W/m-K and decreased to 1.310 W/m-K, a difference of 3.5%. Thus, while the downward trends in measured λ are likely to reflect the effects of gravity drainage, changes up to as long as one hour after sample preparation were considerably small. Since the measurements reported in Figure 5 were started intermediately after the specimens were packed into the beaker (within 5 minutes). It is concluded that gravity drainage was likely to have had little effect on the thermal conductivity dry-out curves.

3.4 SUMMARY

Five different types of soils including three coarse-grained and two fine-grained soils were tested to compare a single-probe transient line source (TLS-SP) sensor and a modified transient plane source (MTPS) sensor for measuring thermal conductivity dryout curves. Measurement protocols for each sensor type applied to coarse-grained and fine-grained soils were developed. Comparison between TCDCs obtained using the MTPS and TLS-SP sensors for the coarse-grained soils indicates that the MTPS sensor consistently produces higher λ for saturation greater than about 0.5, but lower λ for saturation less than about 0.5. Saturated thermal conductivity measured using the MTPS sensor for the five soils ranges from 8% to 26% greater than λ_{sat} measured using the TLS-SP sensor. Dry thermal conductivity measurements using both sensors are comparable (< 5% difference) for the fine-grained soils, but those obtained using the TLS-SP are consistently and appreciably greater for the three coarse-grained soils. Mechanisms responsible for differences observed between the two sensor types include the effects of thermally-induced water migration, contact resistance, gravity-induced water migration, and specimen heterogeneity. Lower λ evident at high saturation and higher λ evident at low saturation using the TLS-SP sensor are potentially attributed to thermally-induced water migration and latent heat transfer, respectively, but these mechanisms have not been experimentally confirmed. Lower measurements of λ obtained using the MTPS sensor for saturations less than about 50% are potentially attributable to contact resistance caused by air pockets between the soil and the planar sensor surface. Secondary experiments indicated that the effects of gravity-induced water redistribution were insignificant within the time frame from sample preparation to measurement.

3.5 REFERENCES

- ASTM. (2012). "Standard test methods for laboratory compaction characteristics of soil using standard effort," *D698-12*, West Conshohocken, PA
- ASTM. (2011). "Standard practice for classification of soils for engineering purposes (unified soil classification system)." *D2487*, West Conshohocken, PA.
- ASTM. (2010). "Standard test methods for liquid limit, plastic limit, and plasticity index of soils." *D4318-10*, West Conshohocken, PA.
- ASTM. (2010). "Standard test methods for specific gravity of soil solids by water pycnometer." *D854-10*, West Conshohocken, PA.
- ASTM. (2007). "Standard test method for particle-size analysis of soils." *D422-63*, West Conshohocken, PA.
- Bareither, C., Edil, T., Benson, C., and Mickelson, D. (2008). "Geological and physical factors affecting the friction angle of compacted sands." *J. Geotech. Geoenviron. Eng.*, 10.1061/(ASCE)1090-0241(2008)134:10(1476), 1476-1489.
- Bouguerra, A., Laurent, J. P., Goual, M. S., and Queneudec, M. (1997). "The measurement of the thermal conductivity of solid aggregates using the transient plane source technique." *J. Phys. D: Appl. Phys.*, *30*(20), 2900.
- Boumaza, T., and Redgrove, J. (2003). "Use of the transient plane source technique for rapid multiple thermal property measurements." *Int. J. Thermophys.*, 24(2), 501-512.
- Campbell, G. S., Jungbauer, J. D., Bidlake, W. R., and Hungerford, R. D. (1994). "Predicting the effect of temperature on soil thermal conductivity." *Soil Sci.*, 158(5), 307-313.
- Côté, J. and Konrad, J. M. (2005). "A generalized thermal conductivity model for soil and construction materials," *Canadian Geotechnical Journal*, 42, 443-458.

- C-Therm Technologies. (2015). "C-Therm TCi operator manual" C-Therm Technologies, Ltd., Fredericton, NB Canada.
- Decagon Devices. (2014). "KD2 Pro thermal properties analyzer" Operator's Manual. Decagon Devices, Inc., Pullman WA.
- de Vries, D.A. (1963). "Thermal properties of soils." *Physics of Plant Environment*, W.R. van Wijk ed., North Holland Pub. Co., Amsterdam, 210-235.
- Farouki, O. T. (1981). "Thermal properties of soils." CRREL Monograph 81-1, U.S. Army COE, Cold Regions Research and Engineering Laboratory, Hanover, NH.
- Fillion, M.-H., Côté, J., Konrad, J.-M. (2011). "Thermal radiation and conduction properties of materials ranging from sand to rock-fill," *Canadian Geotechnical Journal*, 48: 532-542.
- Gurdal, T., Benson, C. and Albright, W. (2003). "Hydrologic properties of final cover soils from the Alternative Cover Assessment Program." Geo Engineering Report 03-02, Geo Engineering Program, University of Wisconsin-Madison.
- Johansen, O. (1975). "Thermal conductivity of soils." Ph.D. thesis, Institute for Kjoleteknikk, Trondheim, Norway.
- Krupa, P., and Malinarič, S. (2014). "Using the transient plane source method for measuring thermal parameters of electroceramics." World Academy of Science, Engineering and Technology, International Journal of Mathematical, Computational, Physical, Electrical and Computer Engineering, 8(5), 733-738.
- Likos, W., Olson, H., and Jaafar, R. (2012). "Comparison of laboratory methods for measuring thermal conductivity of unsaturated soils," *Proc. GeoCongress* 2012: 4366-4375, doi: 10.1061/9780784412121.449

- Likos, W.J. (2014a). "Modeling thermal conductivity dryout curves from soil-water characteristic curves," *Journal of Geotechnical and Geoenvironmental Engineering*, 140(5), doi: 10.1061/(ASCE)GT.1943-5606.0001078, 04013056.
- Likos, W.J. (2014b). "Pore-scale model for thermal conductivity of unsaturated sand," *Journal of Geotechnical and Geological Engineering*, doi: 10.1007/s10706-014-9744-9.
- Log, T., and Gustafsson, S. E. (1995). "Transient plane source (TPS) technique for measuring thermal transport properties of building materials." *Fire and materials*, 19(1), 43-49.
- Lu, N. and Dong, Y. (2015). "Closed-Form Equation for Thermal Conductivity of Unsaturated Soils at Room Temperature." *J. Geotech. Geoenviron. Eng.*, 10.1061/(ASCE)GT.1943-5606.0001295, 04015016.
- Presley, M. A., and P. R. Christensen (1997). "Thermal conductivity measurements of particulate materials 2. Results." *J. Geophys. Res.*, 102(E3), 6551–6566.
- Rides, M., Morikawa, J., Halldahl, L., Hay, B., Lobo, H., Dawson, A., and Allen, C. (2009). "Intercomparison of thermal conductivity and thermal diffusivity methods for plastics." *Polymer Testing*, 28(5), 480-489.
- Sepaskhah, A. R., and Boersma, L. (1979). "Thermal conductivity of soils as a function of temperature and water content." *Soil Sci. Soc. Am. J.*, *43*(3), 439-444.
- Shahraeeni, E., and Or, D. (2012). "Pore scale mechanisms for enhanced vapor transport through partially saturated porous media," *Water Resources Research*, 48, W05511.
- Shiozawa, S., and Campbell, G. S. (1990). "Soil thermal conductivity." *Remote Sens. Rev.*, 5(1), 301-10.

- Smits, K. M., Sakaki, T., Howington, S. E., Peters, J. F., and Illangasekare, T. H. (2013). "Temperature dependence of thermal properties of sands across a wide range of temperatures (30–70C)." *Vadose Zone J.*, 12(1).
- Smits, K. M., Sakaki, T., Limsuwat, A., and Illangasekare, T. H. (2010). "Thermal conductivity of sands under varying moisture and porosity in drainage wetting cycles." *Vadose Zone J.*, 9(1), 1-9.
- Thermtest. (2016) "Thermal constants analyzer-hot disk TPS 3500" TPS3500 Brochure,
 Thermtest Inc., Fredericton, NB Canada.
- van Genuchten, M.T. (1980). "A closed form equation for predicting the hydraulic conductivity of unsaturated soils," *Soil Science Society of America Journal*, 44: 892-890.
- Woodward, N. R., Tinjum, J. M., and Wu, R. (2013). "Water migration impacts on thermal resistivity testing procedures," *Geotechnical Testing Journal*, Vol. 36, No. 6, pp. 1-8, https://doi.org/10.1520/GTJ20120151. ISSN 0149-6115
- Yao, J., Oh, H., Likos, W.J., and Tinjum, J.M. (2014). "Three laboratory methods for measuring thermal resistivity dryout curves of coarse-grained soils," *Geotechnical Testing Journal*, 37(6), pp. 1056-1067, doi:10.1520/GTJ20140120.
- Yun, T. S. and Santamarina, J. C. (2008). "Fundamental study of thermal conduction in dry soils," *Granular Matter*, 10: 197-207.
- Yüksel N. (2016). The review of some commonly used methods and techniques to measure the thermal conductivity of insulation materials, *Insulation materials in context of sustainability*, Amjad Almusaed (Ed.), Intech, doi: 10.5772/64157.

3.6 TABLES

Table 3-1. Comparison of five techniques for measuring soil thermal conductivity

Soil Sample (USCS)	Grain Properties						Atterberg Limit			Density parameters		Van Genuchten (1980) parameters			
	<i>D</i> ₅₀ (mm)	<i>D</i> ₁₀ (mm)	C_u	C_c	Fines (%)	G_s	LL	PL	PI	$\frac{\gamma_{dmax}}{(kN/m^3)}$	e _{test}	α (kPa ⁻¹)	S_r	n	m
SP	0.22	0.15	1.6	1.0	1.1	2.66	-	-	-	16.44	0.60	0.21	0.08	5.09	0.80
SW-SM	0.46	0.08	8.7	1.4	9.1	2.68	-	-	-	19.39	0.40	0.21	0.00	2.05	0.51
SM	0.11	0.05	2.6	1.1	20.8	2.68	-	-	ı	17.27	0.60	0.10	0.10	3.77	0.73
CL	0.006	-	-	-	93.1	2.80	46	24	22	17.7	0.58	0.01	0.00	1.33	0.25
ML	0.034	0.0025	17.6	2.9	82.2	2.78	22	20	2	17.6	0.67	0.01	0.00	1.50	0.33

Table 3-2. Summary of MTPS and TLS-SP sensor specifications (manufacturer reported)

Sensor	MTPS	TLS-SP				
Sangar Typa	Modified Transient Plane	Transient Line Source				
Sensor Type	Source	(Single Probe)				
Sensor Geometry	Planar Circular Surface	Single Needle Probe				
Sensor Geometry	(1.7-cm diam.)	$(0.24\text{-cm diam.} \times 10\text{-cm length})$				
λ range (W/m-K)	$0-0.6^{\dagger}$	0.1 - 4.0				
k range (W/III-K)	0 - 10					
Accuracy	±5%	$\pm 0.02 \text{ (W/m-K)} (\lambda = 0.1 - 0.2)$				
Accuracy	±370	$\pm 10\% \ (\lambda = 0.2 - 4.0)$				
Sensing Time (s)	0.8 - 2.5	300 (default)				
Operating Temperature (°C)	-50 - 200	-50 – 150				

†with material-specific calibration modules

Table 3-3. Saturated thermal conductivity, dry thermal conductivity, and Lu and Dong (2015) modeling parameters for five test soils.

	S	Saturated and	l Dry T	hermal Co	nductivity	Lu and Dong (2015)						
Soil Sample	λ_s	at (W/m-K)		$\lambda_{dry}\left(ext{W/m-K} ight)$			S_f			m		
	MTPS	TLS-SP	Avg	MTPS	TLS-SP	Avg	MTPS	TLS-SP	Avg	MTPS	TLS-SP	Avg
SP	3.13	2.88	3.00	0.13	0.25	0.19	0.11	0.04	0.08	1.90	1.59	1.75
SW-SM	3.55	3.01	3.28	0.13	0.41	0.27	0.18	0.09	0.13	2.20	2.00	2.10
SM	3.13	2.31	2.72	0.13	0.25	0.19	0.17	0.06	0.12	2.03	1.70	1.87
CL	1.97	1.61	1.79	0.76	0.81	0.78	0.34	0.22	0.28	2.91	2.75	2.83
ML	1.85	1.73	1.79	0.60	0.59	0.60	0.44	0.13	0.29	4.08	2.65	3.36

3.7 FIGURES

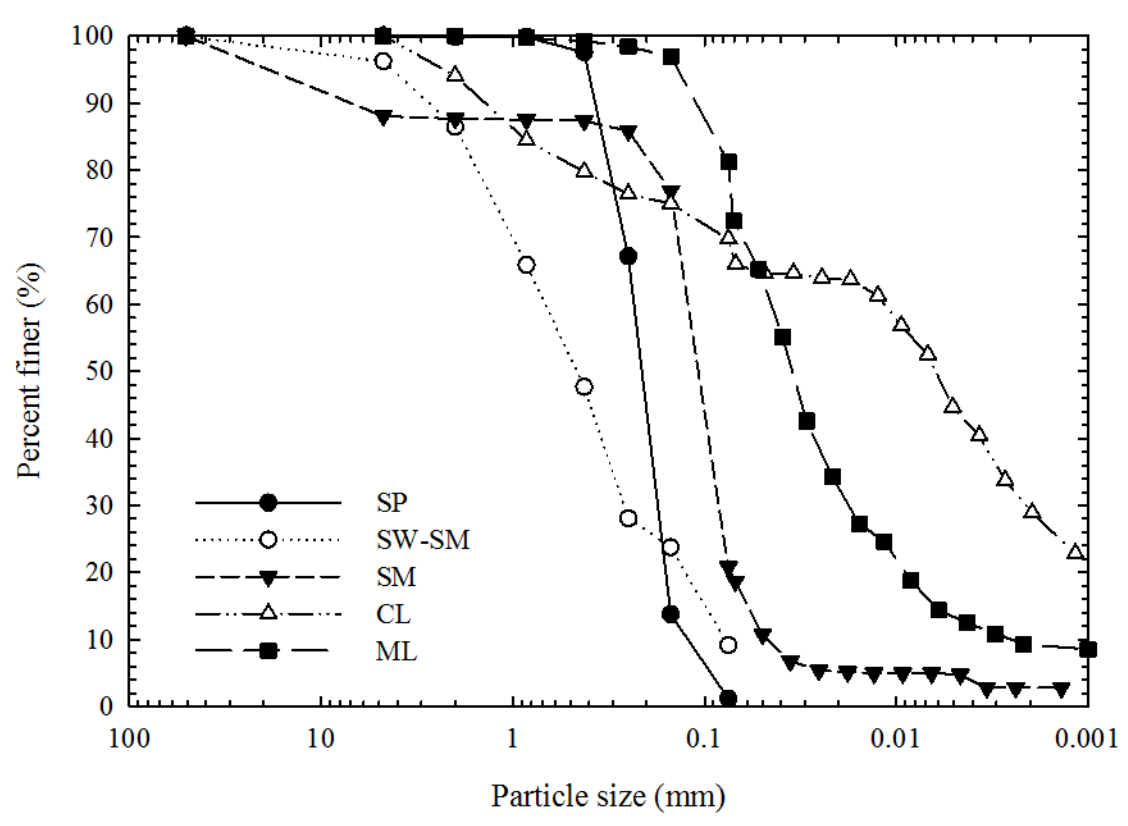


Figure 3-1. Grain size distribution curves for five test soils.

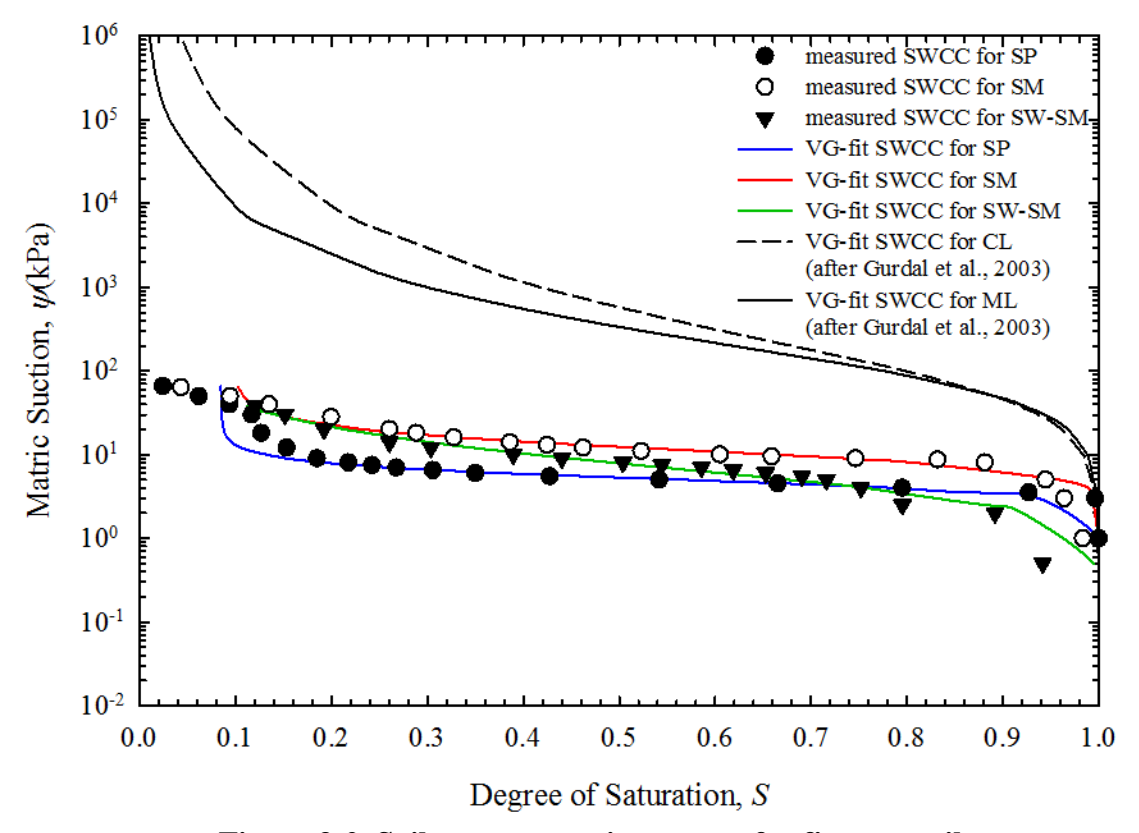


Figure 3-2. Soil-water retention curves for five test soils.

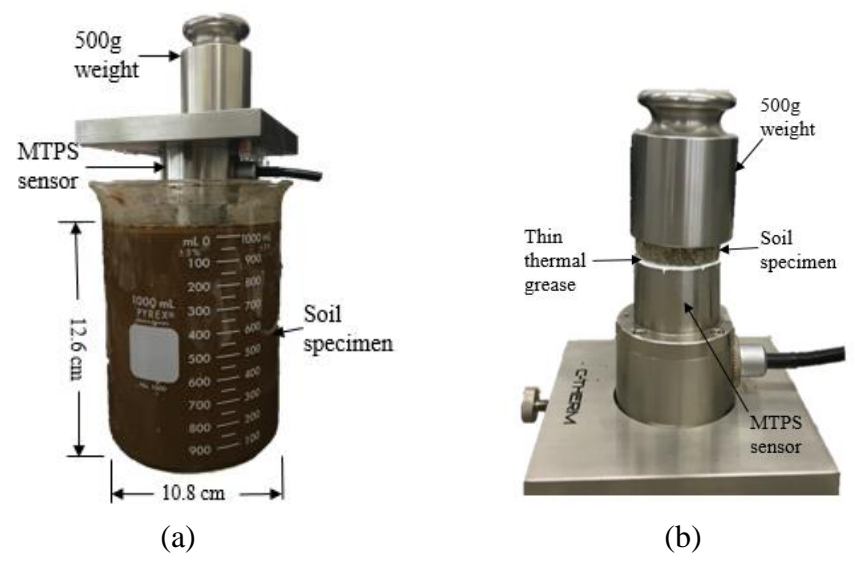


Figure 3-3. Schematic of MTPS sensor set-up for (a) multiple-specimen test procedure and (b) single-specimen test procedure.

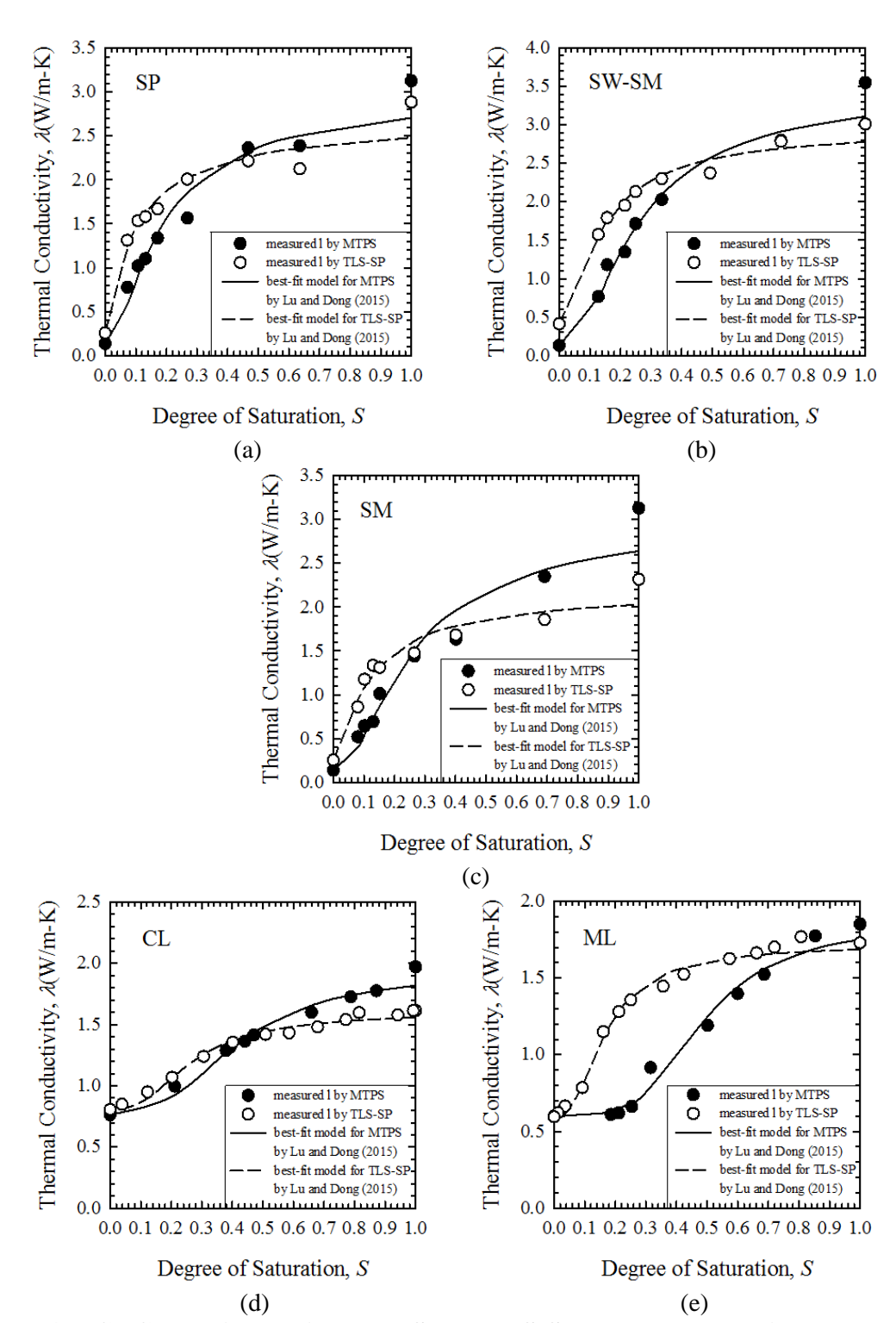


Figure 3-4. TCDCs obtained using MTPS and TLS-SP sensors along with Lu and Dong (2015) models for five test soils: (a) SP; (b) SW-SM; (c) SM; (d) CL; (e) ML.

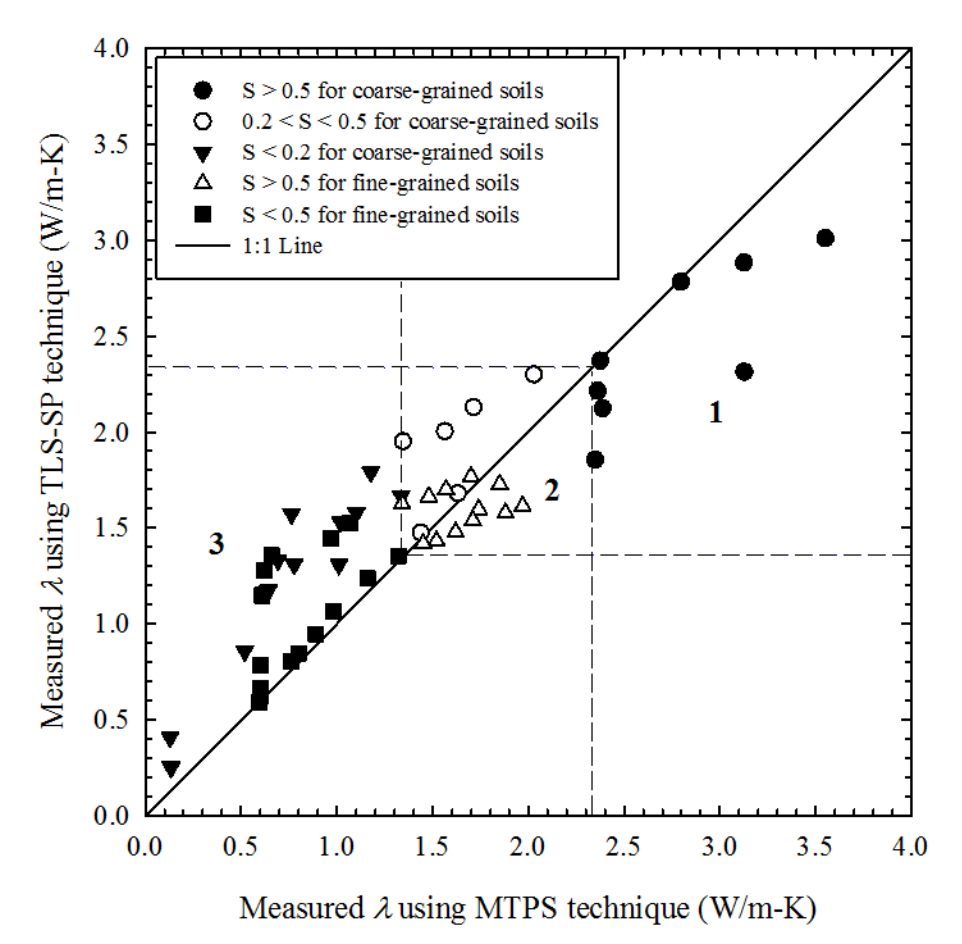


Figure 3-5. Comparison of measured thermal conductivity using TLS-SP and MTPS sensors.

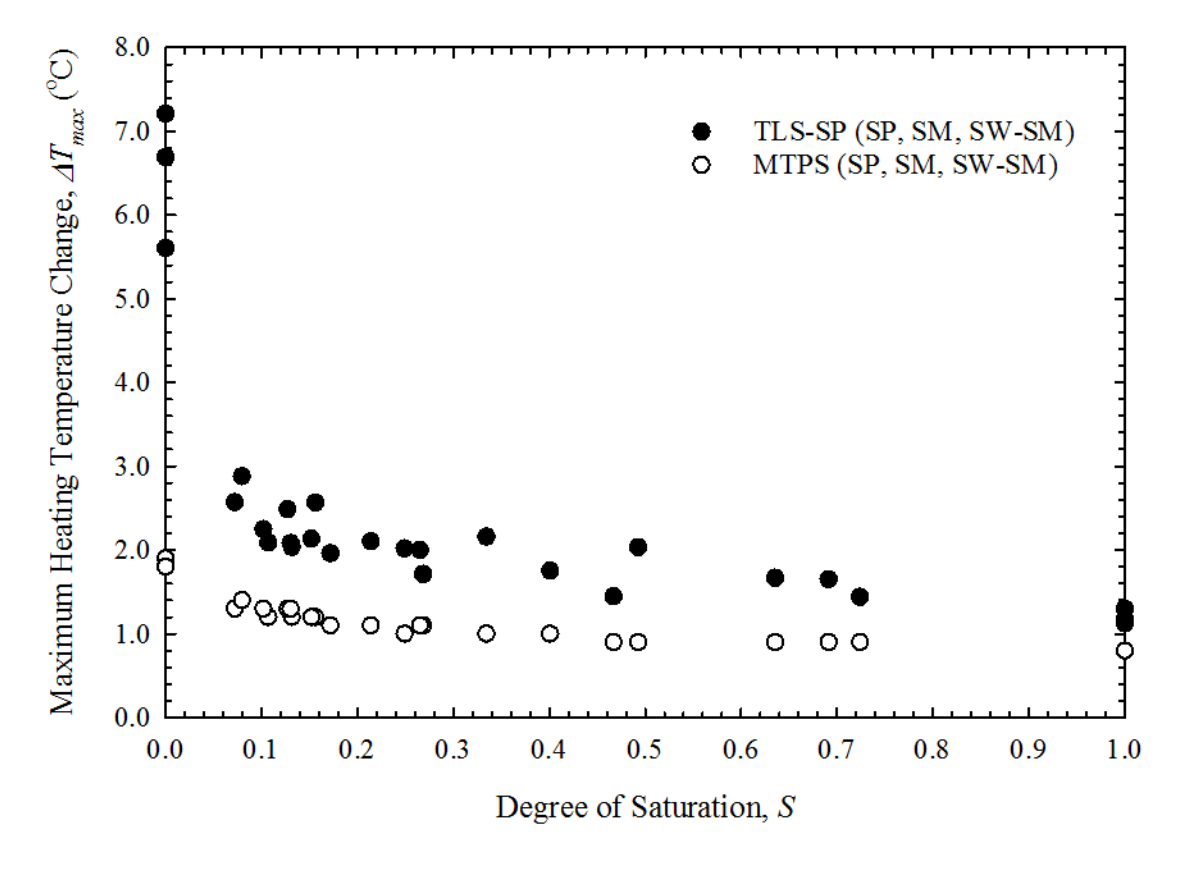


Figure 3-6. Relationship between maximum heating temperature and degree of saturation with TLS-SP and MTPS sensors for coarse-grained soils.

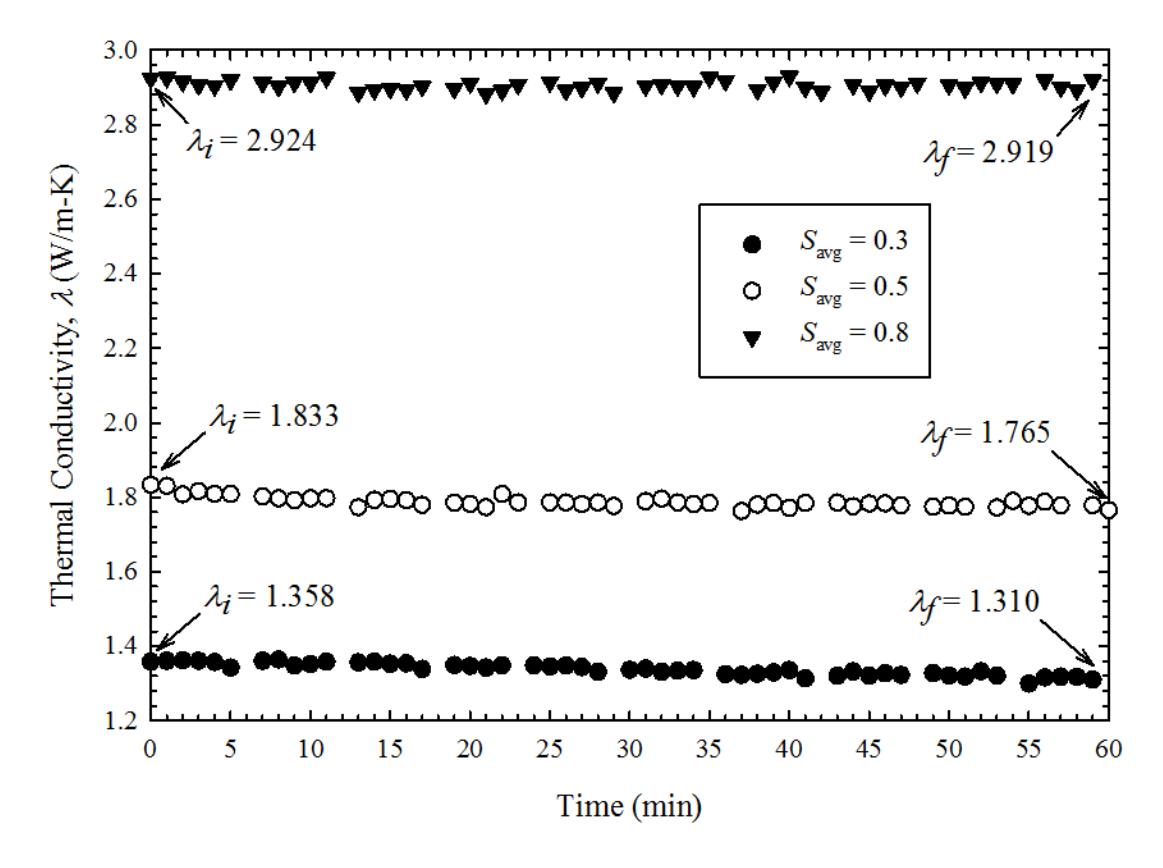


Figure 3-7. Thermal conductivity measured using MTPS sensor at top soil surface (SP) over time.

CHAPTER FOUR

THERMAL CONDUCTIVITY OF UNSATURATED SANDS AT MODERATELY ELEVATED TEMPERATURES (25°C TO 75°C)

ABSTRACT: Thermal conductivity dry out curves (TCDCs) representing the relationship between thermal conductivity and pore water saturation have been measured for two sandy soils under elevated temperatures. Experiments were conducted using an evaporative technique in a temperature-controlled oven at temperatures up to 75°C for concurrent thermal conductivity, temperature, and volumetric water content measurements. Thermal conductivity of both sands at low to intermediate saturations ($S \sim 0.1$ to 0.5) increases appreciably at elevated temperature. Maximum thermal conductivity occurs at 75°C and around the point of critical saturation ($S_c \sim 0.1 - 0.13$), where thermal conductivity is about twice that at room temperature (~23°C). This is attributed to the influence of latent heat transfer from vapor diffusion at air-water interfaces, which have a maximum surface area within this saturation regime. A new empirical model is proposed for predicting thermal conductivity dry out curves at elevated temperatures. Modeled TCDCs show good agreement with experimental results. Performance of the model is evaluated by comparison with existing models for TCDCs at elevated temperatures.

4.1 INTRODUCTION

The importance of soil thermal conductivity (λ) has been increasingly recognized in many geotechnical engineering aspects. Examples include ground-source heat exchangers, energy foundations, underground storage systems, high-level radioactive waste disposal facilities, and backfill for buried power cables (Fan *et al.*, 2007; Brandl, 2006; Pollock, 1986; Brandon *et al.*, 1989). Thermal conductivity of soil minerals varies from 1.0 to 9.0 W/m-K, whereas λ values for water and air are 0.6 and 0.024 W/m-K, respectively (Johansen, 1975; Côté and Konrad, 2005).

Since heat concurrently flows through these three contrasting phases, effective soil thermal conductivity depends on the thermal properties, relative volume fraction, and microstructure of each phase within the multiphase system. The non-linear relationship between soil thermal conductivity and degree of saturation (*S*) is often referred as the thermal conductivity dry-out curve (TCDC) (Likos, 2013). Dependencies of the TCDC on porosity, saturation, and grain size characteristics have been investigated in many previous studies (Johansen, 1975; Farouki, 1981; Hopmans and Dane, 1986; Smits *et al.*, 2010). At non-elevated temperature (~25°C), soil thermal conductivity is at a maximum for the fully saturated condition, decreases with decreasing saturation, dramatically decreases at some critical saturation or "knee-point," and ultimately reaches some minimum at the fully dried condition (Smits *et al.*, 2010; Likos, 2013).

The effects of temperature (T) on soil thermal properties have also been examined in previous studies (e.g., Sepaskhah and Boersma, 1979; Campbell et~al., 1994; Tarnawski and Gori, 2002; Smits et~al., 2013). Sepaskhah and Boersma (1979) measured thermal conductivity of three different soils at 25°C and 45°C and 12 different water contents. Results showed that ratios between thermal conductivity at 45°C (λ_{45}) and at 25°C (λ_{25}) were approximately 2.17, 2.75 and 2.96 for loamy sand at saturation of 22%, loam at S=27%, and silty clay loam at S=35%. Campbell et~al. (1994) conducted similar experiments at elevated temperatures ranging from 30 to 90 °C and found that thermal conductivity of moist soils at 90 °C was 3 to 5 times higher than that at 30 °C. Smits et~al. (2013) utilized sensor-based technologies to continuously measure water saturation and thermal conductivity of silica sands at elevated temperatures from 30 °C to 70 °C. They showed that thermal conductivity increased noticeably when temperatures were greater than 50 °C and at lower saturation, but that the effects of elevated temperature remained small for T between 30°C and 50°C.

Two different sandy soils including a poorly graded sand and a well graded sand with silt are used in this study to determine TCDCs at temperatures ranging from 25°C to 75°C. An empirical model is proposed based on the experimental observations and similar results available in the literature (Campbell *et al.*, 1994; Smits *et al.*, 2013). The proposed model is compared with five other empirical models incorporating the effects of water saturation and temperature for estimating TCDCs (de Vries, 1963; Campbell *et al.*, 1994; Tarnawski *et al.*, 2000a; Tarnawski *et al.*, 2000b; Gori and Corasaniti, 2002).

4.2 BACKGROUND

Neglecting convective flux, heat transfer through partially saturated soil (J_s) is governed by conductive and latent heat transfer according to:

$$J_s = -\lambda_c \nabla T + H J_v \tag{4-1}$$

where λ_c is thermal conductivity from conductive heat transfer, ∇T is the temperature gradient, H is the latent heat of water vaporization, and J_v is the vapor flux. According to Fick's law, vapor flux through soils is expressed by the following equation (Penman, 1940; Jackson *et al.*, 1963; *Cass et al.*, 1984):

$$J_v = -\alpha \theta_a D \nabla \rho \tag{4-2}$$

where α is a dimensionless tortuosity factor, θ_a is the volumetric air content, D is the diffusion coefficient of water vapor in air, and $\nabla \rho$ is the water vapor density gradient. Previous studies have shown that temperature changes have a greater effect on effective soil thermal conductivity due to latent heat from vapor diffusion than on thermal conductivity form conductive heat transfer (de Vries, 1963; Campbell *et al.*, 1994). This is attributed to the fact that a larger temperature dependency of the vapor diffusion parameters $(H, D, \text{ and } \nabla \rho)$ is expected as compared to that of the thermal conductivities of the three independent phases (solid, water and air).

Philip and de Vries (1957) introduced a mechanistic enhancement factor (η) into eq. (5-2) to account for two factors that can occur during vapor diffusion in soil containing air-water interfaces: (i) the local temperature gradient across air-filled pores can be larger than the overall temperature gradient across the bulk soil sample; and (ii) water condensation on one side of a liquid bridge and evaporation from the other side of a liquid bridge can cause an increase in the effective cross-sectional area for vapor flow. This is illustrated in Figure 4-1. When water vapor condenses at A and evaporates from B, the radius of interface curvature would increase at A and decrease at B. The change in interfacial curvature induces a capillary flow in the direction from A to B. This process would eventually decrease the overall tortuosity and path distance for vapor diffusion (i.e., an enhancement to the effective cross-sectional area for vapor flow). Considering these two mechanisms, the mechanistic enhancement factor (η) defined by Philip and de Vries (1957) in the form:

$$\eta = \frac{[\theta_a + f(\theta_a)\theta_w]}{\alpha\theta_a} \frac{(\nabla T)_a}{(\nabla T)} \tag{4-3}$$

where θ_w is the volumetric water content, $(\nabla T)_a$ is the local temperature gradient through the pores, ∇T is the overall temperature gradient through the bulk soil, and $f(\theta_a)$ is a function dependent on volumetric air content in the form:

$$f(\theta_a) = \begin{cases} 1; & \theta_a \ge \theta_k \\ \frac{\theta_a}{\theta_k}; & \theta_a < \theta_k \end{cases}$$
 (4-4)

where θ_k is the volumetric air content where continuity of water films occurs.

Thermal Conductivity Dry-out Curves at Elevated Temperatures

Figure 4-2 shows a series of conceptual TCDCs for soils at elevated temperatures. The TCDCs are divided into 3 distinct regimes based on observations and understanding from previous studies (Campbell, *et al.*, 1994; Smits *et al.*, 2010; Likos, 2013; Lu and Dong, 2015). In regime I,

thermal conductivity from conductive heat transfer (λ_c) decreases slowly as S decreases. This occurs because the continuous water phase in the large pores is being displaced by less conductive air, which effectively forces conductive heat transfer through longer and fewer grain-water-grain pathways. Effective thermal conductivity due to vapor diffusion (λ_v) in this regime, however, would increase as S decreases because there is more pore air and continuous liquid bridges (Figure 4-1), which allows water vapor to more effectively diffuse through the soil. The increasing rate of λ_v is dependent on the intensity of the vapor diffusion, which would increase at higher temperature. The overall thermal conductivity in regime I may thus decrease or increase as S decreases depending upon the magnitude of the temperature.

Previous studies of the TCDC have identified a critical saturation (S_c), where thermal conductivity decreases rapidly at lower saturations (Likos, 2013; Lu and Dong, 2015). When S_c approaches S_c in regime I, λ_v is expected to be at its peak because the vapor diffusion is at maximum through the pore air space and liquid bridges. Since S_c closely corresponds to residual saturation (S_r), where the funicular regime starts to transition into pendular regime, the point of maximum vapor diffusion could be interpreted to occur at a condition where the largest air-water interfacial area is available for vapor diffusion (Likos and Jaafar, 2013). At relatively high temperature, the net effect can be that the overall thermal conductivity reaches a peak value, where latent heat transfer due to vapor diffusion is more dominant than pure conductive transfer.

As S drops below S_c into regime II, λ starts to decrease dramatically because the water phase is no longer continuous and forms isolated liquid bridges between the soil grains. Conductive heat transfer is less effective through the more tortuous grain-water-grain pathways. Hydraulic conductivity is also very low since the liquid bridges are isolated and have retreated into narrower pore throats. This reduces vapor diffusion by inhibiting vapor recirculation through condensation

and re-evaporation cycles. A decreasing vapor density gradient could also reduce latent heat transfer from vapor diffusion through the continuous air phase. In regime III between S = 0 and $S = S_d$, changes in λ are relatively small and close to λ_{dry} . Liquid bridges disappear and the remaining water is primarily in the form of thin films tightly absorbed on particle surfaces (Campbell *et al.*, 1994). At non-elevated temperature, heat transfer in this regime primarily occurs by conduction through grain-to-grain contacts and λ is at a minimum. Higher fines content, however, could result in a longer "tail" within this regime due to the presence of more adsorbed water. At elevated temperatures, the slope of regime III could thus be larger because higher temperature can more effectively vaporize a portion of tightly absorbed water films.

Existing TCDC Models at Elevated Temperatures

de Vries (1963) developed a mixing model to estimate effective soil thermal conductivity by conceptualizing soil particles dispersed in a continuous air or water phase:

$$\lambda = \frac{x_w \lambda_w + \sum_{i=1}^{n} k_i x_i \lambda_i + k_a x_a \lambda_a}{x_w + \sum_{i=1}^{n} k_i x_i + k_a x_a} \tag{4-5}$$

where x is the volume fraction of each phase, k is the ratio of the average temperature gradient in the particle (solid) phase to the average temperature gradient in the continuous medium (*i.e.*, air or water), and n is the number of different minerals comprising the soil solids. Subscripts w, a and i denote water, air and the ith component of each mineral, respectively. Air conductivity λ_a is considered an effective thermal conductivity of humid air inside the pores and includes the thermal conductivity of dry air (λ_{da}) and thermal conductivity due to latent heat from vapor diffusion (λ_v):

$$\lambda_a = \lambda_{da} + \lambda_v \tag{4-6}$$

$$\lambda_v = h \frac{HD}{R_v T} \frac{P}{P - p_{vs}} \frac{\partial p_{vs}}{\partial T} \tag{4-7}$$

where h is the relative humidity, R_v is the gas constant of water vapor, T is the absolute temperature, P is the atmospheric pressure, and p_{vs} is the saturated partial water vapor pressure. Campbell *et al.*

(1994) and Tarnawski *et al.* (2000a) proposed revised mixing models using a similar conceptualization. Gori and Corasaniti (2002) proposed a model by conceptualizing a cubic soil particle surrounded by various amount of water and air. Despite the differences among these four mixing models, the effect of latent heat transfer captured by eq. (4-6) and (4-7) was used to account for the effects of elevated temperature in each case.

4.3 PROPOSED MODEL

Tarnawski *et al.* (2000b) developed an empirical function for the Kersten number (K_e) and incorporated it into Johansen's (1975) normalized thermal conductivity approach used to interpolate between dry (λ_{dry}) and saturated (λ_{sat}) soil thermal conductivity:

$$\lambda = \lambda_{dry} + K_e(\lambda_{sat} - \lambda_{dry}) \tag{4-8}$$

The K_e proposed by Tarnawski *et al.* (2000b) was linked to saturation (S) and temperature (T) in the form:

$$K_e = \frac{a + bT + cS + dS^2}{1 + eT + fS + gS^2} \tag{4-9}$$

where a, b, c, d, e, f and g are fitting parameters and it was suggested that K_e needs to be linearly interpolated when saturation is below about 0.125.

A similar approach is proposed here. Based upon mechanistic understanding of TCDCs at elevated temperatures as summarized in Figure 4-1, the experimental TCDCs presented subsequently, and results from previous studies for similar soils (Campbell, *et al.*, 1994; Smits *et al.*, 2013), a new empirical K_e function is proposed as follows:

$$K_{e} = \begin{cases} 0; & S \leq S_{d} \\ \sqrt{\frac{S - S_{d}}{1 - S_{d}}} + \omega \left[\frac{S}{\sigma}\right]^{\chi - 1} \exp\left[-\left(\frac{S}{\sigma}\right)^{\chi}\right]; & S > S_{d} \end{cases}$$

$$(4-10)$$

where m is a matrix connectivity term to account for conductive heat transfer, ω is a temperature dependent factor, χ is a pore throat connectivity factor, and σ is a dimensionless parameter in the form:

$$\sigma = S_c \sqrt[\chi]{\frac{\chi}{\chi - 1}} \tag{4-11}$$

When $S > S_d$, eq. (4-10) superimposes thermal conductivity contributions from both conductive heat transfer and latent heat due to vapor diffusion.

4.4 MATERIALS AND METHODS

Two sands were selected to evaluate the temperature effects on thermal conductivity of soils and the proposed model performance: poorly graded sand (SP4) and well-graded sand with silt (SW-SM2). Figure 4-3 shows grain-size distributions obtained using mechanical sieve analysis (ASTM D422). Table 4-1 summarizes grain size parameters D_{50} , D_{10} , C_u , C_c , fines content, and solid specific gravity (G_s).

Soil-water characteristic curves (SWCCs) and TCDCs were concurrently obtained along an initial drying path (drainage from S=1) using an instrumented hanging column apparatus initially developed by Smits *et al.* (2010). Detailed testing procedures described in Yao *et al.* (2014) were modified to measure TCDCs at elevated temperatures. First, the tensiometer for matric suction measurement and the hanging column apparatus for controlling suction were removed to conveniently accommodate the set-up into a temperature-controlled oven. The dielectric moisture sensor was changed from the EC-5 (Decagon Devices, Pullman, WA), as described by Yao *et al.* (2014), to the 5TM sensor (Decagon Devices) because the 5TM moisture sensor could tolerate higher temperature (80 °C) and could simultaneously measure temperature. To prepare specimens, the required amount of water to achieve full saturation at void ratio e_{test} (Table 1) was first poured into a cylindrical cell. Sand was then poured directly into the water through a plastic funnel. This

was done in four equal lifts to achieve the target void ratio (*e*_{test}). The final specimen height was 13cm. The 5TM moisture sensor and a dual-needle thermal conductivity sensor (SH-1, Decagon Devices) were embedded in the sand between the 2nd and 3rd layers. After packing, extra water was poured on top of the saturated sand, and the top of the cell was sealed with plastic film. This additional water was required to maintain the sand at 100% saturation during temperature equilibration after placing the specimen in a temperature-controlled. After the temperature equilibration process (~24 h), the plastic film was removed so that evaporation could occur. The temperature of the sand, oven, volumetric water content, and thermal conductivity were concurrently measured to obtain TCDCs during the evaporation process. These procedures were repeated for five target elevated temperatures of 35, 45, 55, 65, and 75°C.

4.5 RESULTS AND DISCUSSION

Figure 4-4 shows measured TCDCs and SWCCs for the SP4 and SW-SM2 at different elevated temperatures. At room temperature (~22.8°C), the thermal conductivity remains relatively constant until the saturation decreases to about 0.77 and 0.60 for SP4 and SW-SM2, respectively. After this flat regime, the thermal conductivity decreases slowly in a generally linear trend with decreasing saturation for both sands. Then the thermal conductivity of each sand abruptly decreases after a critical saturation (S_c). The values of S_c for SP4 and SW-SM2 are approximately 0.1 and 0.13 respectively. Residual saturations (S_r) observed from the SWCCs are 0.15 and 0.2 for SP4 and SW-SM2, which are slightly higher than the values of S_c . S_r was obtained graphically by drawing tangent lines through the upper and lower portions on SWCC. Finally, at about S_d = 0.02 and 0.05 for SP4 and SW-SM2, the thermal conductivity tends to level off to a constant dry thermal conductivity. The larger S_d value for SW-SM2 at room temperature is interpreted to reflect its higher fines content (~9.1%) as previously described.

Thermal generally conductivity increases as temperature increases at a low to intermediate saturation for both sands (\sim 0.2 to 0.5). However, some discrepancies were observed at some elevated temperatures, especially for measurements at 35.6 °C for SP4. Between S=1 and S=0.25, the thermal conductivity at 35.6 °C is appreciably higher than that at 46.6 °C. This discrepancy might be due to the variations and heterogeneity of the soil bulk densities when preparing the soil specimens for different temperatures. When the soils are fully saturated or fully dried, the thermal conductivity measurements are similar between different elevated temperatures. This is attributable to the relative small temperature dependency of the water, dry air and soil particles. The maximum difference of thermal conductivity measurements between different elevated temperatures occurs near $S=S_c$ for both sands. At $S=S_c$, the thermal conductivity measurements at about 75 °C are approximately 2.3 and 2 times larger than those at room temperature for SP4 and SW-SM2 respectively. The "tails" observed in TCDCs at room temperatures for both soils become shorter at higher temperature, which is consistent with the conceptual TCDCs described in background section.

Measured TCDCs were fit with the proposed model (dashed lines in Fig. 4-4). There is good agreement between the measured and modeled TCDCs for both sands and at each temperature. The model requires seven fitting parameters (λ_{sat} , λ_{dry} , S_c , S_d , m, χ , and ω). The fitting values for λ_{sat} and λ_{dry} were taken directly from measured values at these extremes. Five parameters (S_c , S_d , m, χ , and ω) were optimized by implementing the model into a spreadsheet and using a multivariable solver to best match the measured TCDC modeled TCDCs at 75 °C. Values of m, χ , and S_c optimized by best-fitting the TCDCs at 75 °C were held constant to model the TCDCs at lower temperatures by optimizing ω and S_d (i.e., only these two parameters are required to capture temperature dependency). Table 4-2 summarizes the best-fit parameters. It is interesting that the

matrix connectivity term (m) is larger than the pore throat connectivity term (χ) because conductive heat transfer may occur through both soil grains and pore spaces while vapor can only diffuse through pore spaces. Figure 4-5 shows the relationship between the temperature-dependent factor (ω) and temperature for both sands, which can be well defined by a power law model. This observation is consistent with the notion that the intensity of vapor diffusion positively correlates with temperature.

Previous models were also fit to the experimental TCDCs. Coefficients of determination (R^2) were calculated to evaluate the quality of fitting for each model at different temperatures based on the following equation:

$$R^2 = 1 - \frac{\sum (\lambda - \tilde{\lambda})^2}{\sum (\lambda - \bar{\lambda})^2} \tag{4-12}$$

where $\tilde{\lambda}$ is the modeled thermal conductivity and $\bar{\lambda}$ is the mean measured thermal conductivity. Table 4-3 summarizes R^2 for each model at different temperatures. Overall, the proposed model has the largest average R^2 for both sands. The Tarnawski *et al.* (2000b) model also performs well $(R^2 > 0.9)$ for both sands. The Gori and Corasaniti (2002) model provides the poorest fit $(R^2 < 0.5)$ especially at lower temperature (~22.8°C to 46.5°C).

4.6 SUMMARY

Sands including a poorly graded sand and a well-graded sand with silt were tested to evaluate the effects of elevated temperature on TCDCs. Maximum thermal conductivity was observed at 75 °C and near the critical saturation point ($S \sim 0.1$) for both sands. This was attributed to effective vapor transport at higher temperature and at the point of saturation where air-water interface area for vapor evaporation-condensation is largest. A new empirical model was proposed based on conceptual TCDCs at elevated temperatures. Average coefficient of determination (R^2) over the range of measured temperature was 0.95 for both sands.

4.7 REFERENCES

- ASTM D 422-63. (2007). "Standard test method for particle-size analysis of soils."
- Brandl, H. (2006). "Energy foundations and other thermo-active ground structures." *Geotechnique*, 56(2), 81–122.
- Brandon, T.L., Mitchell, J.K., and Cameron, J.T. (1989). "Thermal instability in buried cable backfills." *J. of Geotechnical Engineering*, ASCE, 115(1), 38-55.
- Campbell, G.S., Jungbauer, J.D., Bidlake, W.R., and Hungerford, R.D. (1994). "Predicting the effect of temperature on soil thermal conductivity." *Soil Science*, 158(5), 307-313.
- Cass, A., Campbell, G. S., and Jones, T. L. (1984), "Enhancement of thermal water vapor diffusion in soil". *Soil Science Society of America Journal*, 48(1), 25–32.
- Côté, J., and Konrad, J. M. (2005). "A generalized thermal conductivity model for soils and construction materials." *Canadian Geotechnical Journal*. 42(2), 443-458.
- de Vries, D.A. (1963). "Thermal properties of soils." *Physics of Plant Environment*. W.R. van Wijk (ed.). North Holland Pub. Co. Amsterdam: 210-235.
- Fan, R., Jiang, Y., Yao, Y., Shiming, D., and Ma, Z. (2007). "A Study on the performance of a geothermal heat exchanger under coupled heat conduction and groundwater advection." *Energy*, 32(11), 2199-2209.
- Farouki, O. T. (1981). *Thermal properties of soils* (No. CRREL-MONO-81-1). COLD REGIONS RESEARCH AND ENGINEERING LAB HANOVER NH.
- Gori, F., and Corasaniti, S. (2002). "Theoretical prediction of the soil thermal conductivity at moderately high temperatures." *Journal of heat transfer*, 124(6), 1001-1008.

- Hopmans, J.W., and Dane, J.H. (1986). "Thermal conductivity of two porous media as a function of water content, temperature, and density." *Soil Science Society of America Journal*, Vol. 142 (4): 187-195.
- Jackson, R.D., Nielson, and D. R., Nakayama, F. S. (1963). "On diffusion laws applied to porous materials." USDA-ARS, ARS 41-86, Washington, D.C.
- Johansen, O. (1975). "Thermal conductivity of soils." Ph.D. thesis, Institute for Kjoleteknikk, Trondheim, Norway.
- Likos, W. (2013). "Modeling thermal conductivity dryout curves from soil-water characteristic curves." *J. Geotech. Geoenviron. Eng.*, 10.1061/(ASCE)GT.1943-5606.0001078, 04013056.
- Likos, W. J., and Jaafar, R. (2013). "Pore-scale model for water retention and fluid microstructure of partially saturated coarse-grained soil." J. *Geotech. Geoenviron. Eng.*, 10.1061/(ASCE)GT.1943-5606.0000811, 724–737.
- Lu, N. and Dong, Y. (2015). "Closed-form equation for thermal conductivity of unsaturated soils at room temperature." *J. Geotech. Geoenviron. Eng.*, 10.1061/(ASCE)GT.1943-5606.0001295, 04015016.
- Penman, H.L. (1940). "Gas and vapour movements in soil: I. The diffusion of vapours through porous solids." *The Journal of Agricultural Science*, 30, 437–462.
- Philip, J. R., and de Vries, D.A. (1957). "Moisture movement in porous materials under temperature gradients." *Transactions of American Geophysical Union*, 38(2), 10.
- Pollock, D. W. (1986). "Simulation of fluid flow and energy transport processes associated with high-level radioactive waste disposal in unsaturated alluvium." *Water Resources Research*, 22(5), 765-775.

- Sepaskhah, A. R., and Boersma, L. (1979). "Thermal conductivity of soils as a function of temperature and water content." *Soil Science Society of America Journal*. 43(3), 439–444.
- Smits, K. M., Sakaki, T., Howington, S. E., Peters, J. F., and Illangasekare, T. H., 2013, "Temperature dependence of thermal properties of sands across a wide range of temperatures (30–70C)," *Vadose Zone Journal*, Vol. 12
- Smits, K. M., Sakaki, T., Limsuwat, A., and Illangasekare, T. H. (2010). "Thermal conductivity of sands under varying moisture and porosity in drainage-wetting Cycles." *Vadose Zone Journal*, *9*(1), 1-9.
- Tarnawski, V.R., and F. Gori. (2002). "Enhancement of the cubic cell soil thermal conductivity model." *International Journal of Energy Research*. 26:143–157.
- Tarnawski VR, Gori F, Wagner B, Buchan GD. (2000). "Modeling approaches to predicting thermal conductivity of soils at high temperatures." *International Journal of Energy Research*. 24:403-423.
- Tarnawski, V.R., W.H. Leong, and K.L. Bristow. (2000). "Developing a temperature dependent Kersten function on for soil thermal conductivity." *International Journal of Energy Research.* 24:1335–1350.
- Yao, J., Oh, H., Likos, W. J., and Tinjum, J. M. (2014). "Three laboratory methods for measuring thermal resistivity dryout curves of coarse-grained soils." *J. ASTM Geotech. Test.*, 37(6), 1-12.

4.8 TABLES

Table 4-1. Summary of index properties for two sands.

Specimen	USCS	D_{50} (mm)	D_{10} (mm)	C_u	C_c	Fines (%)	G_s	e_{test}
SP4	SP	0.22	0.15	1.6	1	1.1	2.66	0.6
SW-SM2	SW-SM	0.46	0.08	8.7	1.4	9.1	2.68	0.47

Table 4-2. Summary of the results for best-fitting parameters

Specimen	m	χ	S_c	ω @22.8 °C	S _d @22.8 °C
SP4	5.07	1.15	0.05	0.000	0.024
SW-SM2	6.40	1.30	0.09	0.065	0.090

Table 4-3. Summary of \mathbb{R}^2 at different temperatures of each model for two soils

			R^2	for SP4				R^2 for SW-SM2							
T (°C) Proposed	Proposed	do Vrios	Campbell	Tarnawski	Gori and	Tarnawski _T	T (°C)	Proposed model	do Vrios	Campbell	Tarnawski	Gori and	Tarnawski		
	model	(1963)	et al.	et al.	Corasaniti	et al.	1 (0)		(1963)	et al.	et al.	Corasaniti	et al.		
	model	(1903)	(1994)	(2000a)	(2002)	(2000b)		model		(1994)	(2000a)	(2002)	(2000b)		
22.8	0.96	0.97	0.97	0.84	0.00*	0.96	22.8	0.90	0.90	0.93	0.88	0.08	0.93		
35.6	0.90	0.53	0.39	0.00*	0.00*	0.94	39.7	0.99	0.78	0.77	0.86	0.00*	0.97		
46.6	0.94	0.97	0.88	0.62	0.00*	0.84	46.1	0.98	0.88	0.62	0.87	0.25	0.93		
54.6	0.96	0.94	0.83	0.49	0.04	0.94	54.9	0.97	0.61	0.06	0.88	0.73	0.83		
65.5	0.95	0.77	0.67	0.34	0.50	0.81	65.4	0.93	0.62	0.67	0.83	0.82	0.85		
74.0	0.97	0.81	0.70	0.69	0.68	0.89	76.3	0.95	0.30	0.00*	0.82	0.39	0.92		
Avg.	0.95	0.83	0.74	0.50	0.20	0.90	Avg.	0.95	0.68	0.51	0.86	0.38	0.90		

^{*} zero R^2 was manually assigned because the calculated negative R^2 does not exist

4.9 FIGURES

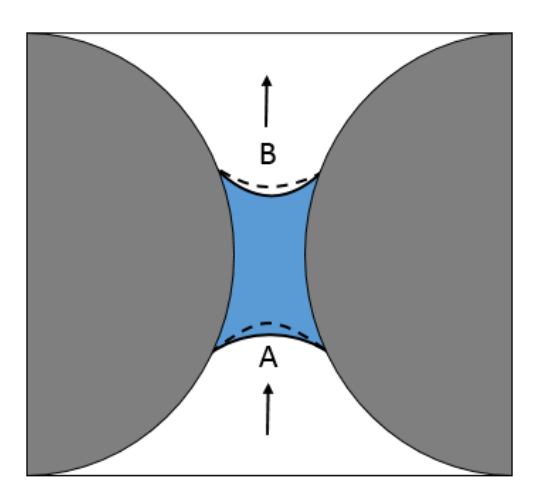


Figure 4-1. Schematic of capillary-assisted vapor diffusion

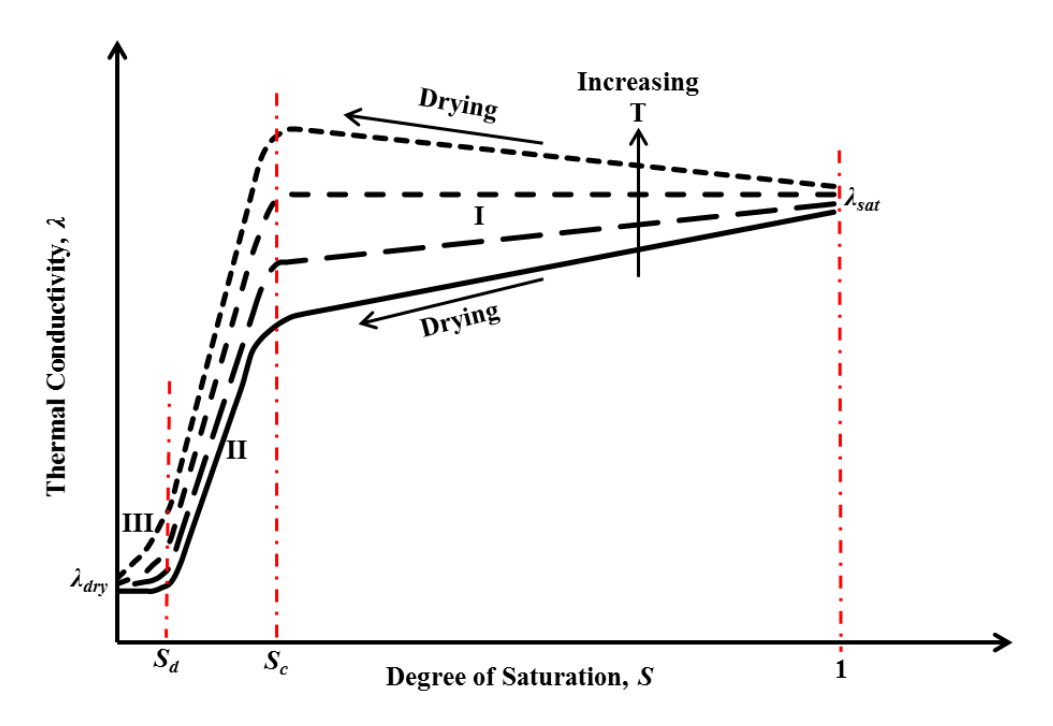
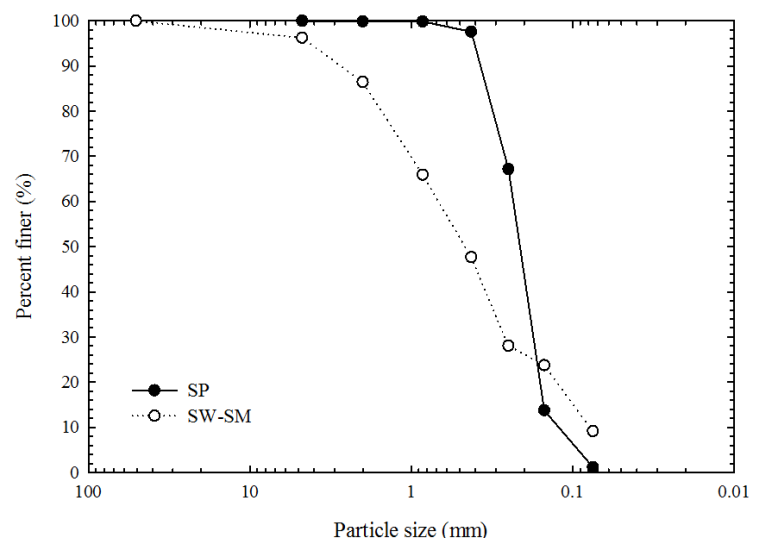
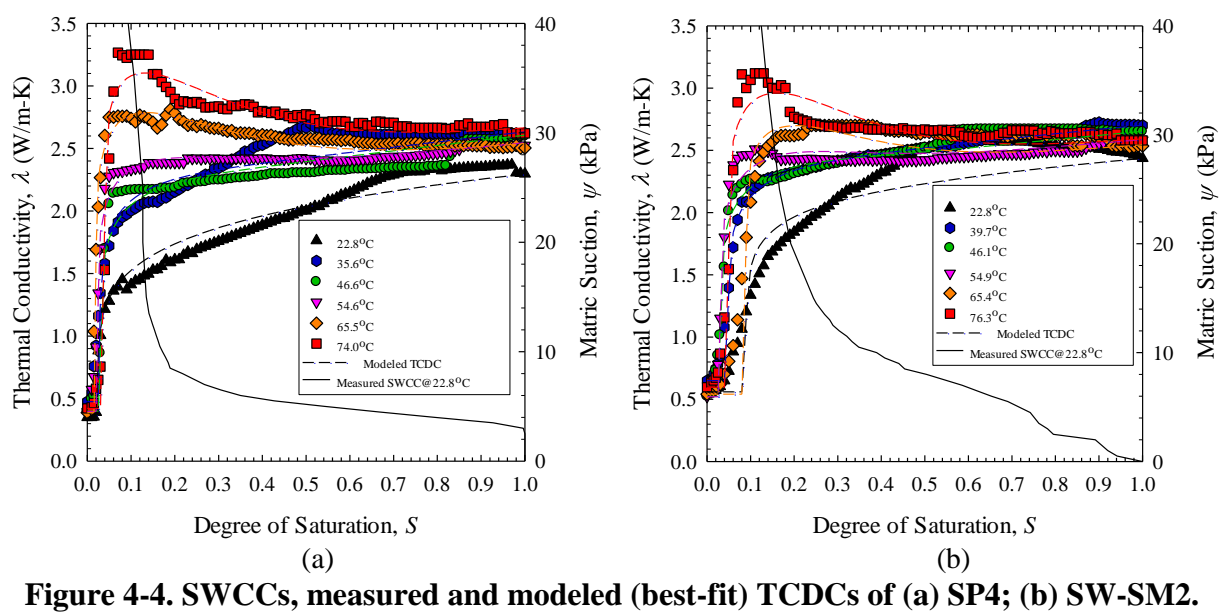


Figure 4-2. Conceptual TCDCs at elevated temperatures





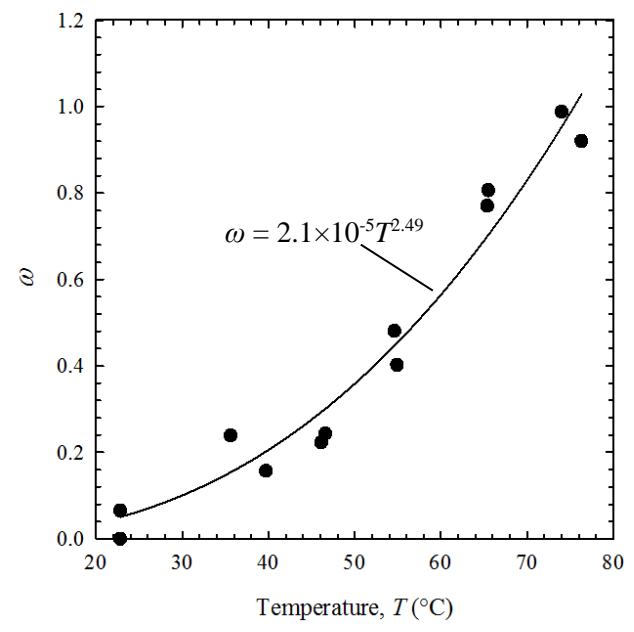


Figure 4-5. Relationship between $\boldsymbol{\omega}$ and temperature for both sands.

CHAPTER FIVE

THERMAL CONDUCTIVITY OF COMPACTED CLAYS

ABSTRACT: Thermal conductivity dryout curves (TCDCs) were measured for four different clayer soils. A single-needle thermal probe following single-specimen staged-drying method was used to measure the thermal conductivity of each soil compacted dry and wet of optimum. Results indicate that soils with higher clay content compacted wet of optimum (WOPT) generally have higher thermal conductivity than those compacted dry of optimum (DOPT). Lower thermal conductivity for DOPT of more clay-rich soils are potentially attributed to larger inter-clod voids for DOPT, which may responsible for less effective heat conduction through clods. Mercury Intrusion Porosimetry (MIP) tests conducted on one of the clay-rich sample indicated that the DOPT sample had higher percentage of larger inter-clod voids than the WOPT sample.

5.1 INTRODUCTION

A comprehensive understanding of soil thermal properties is of great importance in many geological and geotechnical applications involving thermal analysis. For example, in high-level radioactive nuclear waste repositories, compacted bentonite has been considered as a buffer material to isolate radioactive waste from surrounding host rock formation (Knutsson, 1983; Pusch, 1992; Delage, et. al., 2010). In this application, accurate measurement and prediction of thermal conductivity of compacted bentonite is a key component for analyzing long-term coupled thermohydro-mechanical-chemical (THMC) phenomena. Other applications involving soil thermal properties may include underground storage systems, backfill design for buried power cables, energy piles, and shallow ground-source heat exchangers (Shelton, 1975; Abdel-Hadi and Mitchell, 1981; Brandl, 2006; Fan et al, 2007).

Soil thermal conductivity is not a constant, but rather depend on minerology, particle size and gradation, density, microstructures, pore water saturation, temperature, and stress. For finegrained soils, especially clayey soils, different micro- and macro-structures may exist with different remolding water content. Lambe (1958) proposed that clay samples compacted at the dry side of optimum would tend to have flocculated or edge-to-face structure, while clay samples compacted at the wet side of optimum wound tend to have dispersed or parallel structure, as shown in Figure 5-1a. This theory, often referred as particle orientation theory, assumes remolding water content would affect the orientation of individual clay particles during compaction. Olsen (1962) proposed another theory that suggested the clay particles group together and form clusters prior to compaction. These clusters, often referred as clods or "aggregates", would be harder at lower remolding water content (i.e., dry side of optimum) than those at higher remolding water content (i.e., wet side of optimum). Therefore, harder clods compacted dry of optimum would result in larger inter-clod voids compared to softer clods compacted wet of optimum, as illustrated in Figure 5-1b. Previous studies have suggested no evidence for particle-orientation theory, but rather strong evidence for clods theory (Sloane and Kell, 1966; Diamond, 1971; Garcia-Bengochea, 1979; Benson and Daniel, 1990; Delage et. al., 1996). These studies also indicated that hydraulic conductivity of clay compacted wet of optimum would be lower compared to that compacted dry of optimum because of the clods theory.

In this section, each of four natural clayey soils was compacted at a dry and a wet of optimum, respectively. Thermal conductivity of each specimen was measured over the full range of saturation to produce thermal conductivity dryout curves (TCDC). The main purpose of this study is to evaluate the difference between thermal conductivity of clay compacted dry of optimum

and wet of optimum. An existing model is also evaluated for estimating thermal conductivity dryout curves.

5.2 MATERIALS AND METHODS

Four fine-grained soils selected for this study include two lean clays with sand, one sandy lean clay and one lean clay. These were natural soils obtained from field sites associated with the United States Environmental Protection Agency's (USEPA) Alternative Cover Assessment Program (ACAP) (Gurdal et. al., 2003). Table 5-1 summarizes grain size and index properties including D_{50} , mass fraction of clay, silt and sand, solid specific gravity (G_s), liquid limit (LL), plastic limit (PL), plasticity index (PI = LL-PL), maximum dry density (γ_{dmax}) and optimum water content (*w_{opt}*). Figure 5-2 shows grain size distribution (GSD) curves obtained from wet sieve and hydrometer analysis according to ASTM D6913 and D7928. From the GSD curves and Atterberg limits, all four soils were classified as CL by Unified Soil Classification System (ASTM D2487). Specific gravity (G_s) was determined according to ASTM D854. Figure 5-3 shows compaction curves for these four soils. Compaction tests were performed by standard Procter method described in ASTM D698. The values of maximum dry density (γ_{dmax}) were determined from the peak of the compaction curves. The van Genuchten (1980) modeling parameters (S_r , α , n, and m) for constructing soil-water retention curves were reported by Gurdal et al. (2003), as summarized on Table 5-1. The VG model is in the form:

$$\frac{S - S_r}{1 - S_r} = \left[\frac{1}{1 + (\alpha \psi)^n} \right]^m \tag{5-1}$$

where residual saturation S_r , n, and m are empirical fitting parameters optimized to best fit the experimental data.

Procedures for measuring TCDCs of four fine-grained soils followed a single-specimen staged-drying approach. In order to create compacted specimens at dry side of optimum and wet side of optimum with identical dry unit weights, a target dry unit weight (Table 5-2) was chosen for each soil, and corresponding target water contents (Table 5-2) at dry side of optimum (w_{dopt}) and wet side of optimum (w_{wopt}) could be visually obtained from compaction curves for each soil. Then moist soil was prepared by carefully mixing oven-dried soil with enough water to achieve target water content and sealed in a plastic bag for 24 hours. Prior to compaction, a sub-sample was taken from the hydrated soils for checking actual water content (reported in Table 5-2). The soil was then carefully compacted into the compaction mold in three equal lifts to reach target dry unit weight. The actual dry unit weight reported in Table 5-2 was calculated based on actual water content and weight of moist soil compacted in the mold. The specimen and compaction mold were then submerged in de-aired water under vacuum to reach saturation. The TLS-SP sensor was inserted vertically into the center of the compacted specimen to obtain the first thermal conductivity measurement. The specimen and mold were then placed into a 60 °C oven without removing the probe, removed from the oven every 24 hours, and allowed to cool to room temperature before measuring thermal conductivity and the incremental change in mass due to drying. For every specimen, the drying process was stopped when less than 0.1 g change in mass within 24 hours, at which soil was assumed to reach zero saturation. This process was repeated for four selected soils compacted wet and dry of optimum.

Mercury Intrusion Porosimetry (MIP) test

Two DC18 specimens compacted dry and wet of optimum were prepared at associated target unit weight shown in Table 5-2. Then cubic samples (1 cm by 1 cm) were cut from the center of the compacted specimens. The cubic samples underwent 60 °C oven-drying for 48 hours to

reach fully-dried condition. Then the pore size distributions were analyzed by a Micromeritics Auto IV 9510 MIP device at University of Texas-Arlington Geoscience Lab. This MIP device is capable of measuring pore diameters from 0.003 to 1100 microns. The detailed procedure for this test was given by ASTM D4404.

5.3 RESULTS AND DISCUSSION

Figure 5-5 shows a series of measured TCDCs of four soils compacted dry of optimum (DOPT) and wet of optimum (WOPT). General characteristics of each TCDC are comparable to observations in previous studies on clayey samples (e.g., Sepaskhah and Boersma, 1979; Campbell, 1994; Lu et. al., 2007). Thermal conductivity at saturation (λ_{sat}) is at a maximum for each soil. As reported in Table 5-3, the average λ_{sat} values between DOPT and WOPT for APT29, ALT28 and DC18 are similar to each other, but relatively lower than that for LC8. This is consistent with the observations from Chapter 3 and attributed to higher clay content and lower sand content for ALT29, ALT28 and DC18 than LC8 (Table 5-1). Thermal conductivity of quartz ($\lambda \sim 8.8 \text{W/m-K}$) comprising most sands is approximately three times of that of clay minerals ($\lambda \sim 2.9 \text{W/m-K}$) (de Varies 1963). As saturation decreases, thermal conductivity for each soil decreases slowly until reaching a saturation where thermal conductivity starts to decrease more rapidly. This saturation is often referred as critical saturation that is the transitional boundary between the funicular regime and pendular regime, as illustrated in Chapter 3. As shown in Figure 5-5, the transition from funicular to pendular regime for ALT29, ALT28 and DC18 appears to be more gradual and smoother than for LC8. Additionally, critical saturation for ALT29, ALT28 and DC18 varying from 0.42 to 0.5 is noticeably larger than that for LC8. More gradual transition and larger critical saturation for ALT29, ALT28 and DC18 are attributable to their higher clay content (i.e., higher

specific surface area) and generally larger variability in pore size and geometry compared to LC8 with less clay content (Lu and Dong, 2015).

As saturation continues to decrease in the pendular regime, thermal conductivity tends to level off at some saturation for each soil. This saturation is referred as cut-off saturation by Campbell (1994), where water vapor recirculation is minimized and water molecule is absorbed on fine particles through short-range hydration. Any further reduction of saturation results in minimum change in thermal conductivity; thus forms flat tail for TCDC. In order to capture this cut-off saturation (S_o), measured TCDCs for each soil compacted dry and wet of optimum were best-fit with Campbell (1985) model using the following equations:

$$\lambda = \lambda_{sat}g + \lambda_{drv}(1 - g) + 2.8n(nS - ng) \tag{5-2}$$

$$g = \frac{1}{1 + (\frac{S}{S_0})^{-5}} \tag{5-3}$$

where n is the porosity, and g is an empirical weighing factor. The model requires four fitting parameters (λ_{sat} , λ_{dry} , S_o , n). The fitting values for λ_{sat} and λ_{dry} were taken directly from measured values at these extremes. The porosity (n) was calculated based on the dry unit weight and specific gravity given in Table 5-2. Therefore, a single fitting parameter, S_o , were optimized by implementing the model into a spreadsheet and using a multivariable solver to best match the measured TCDC with modeled TCDCs

The optimized cut-off saturation (S_o) and the average coefficient of determination (R^2) for each soil were included in Table 5-3. As shown in Figure 5-4, it is evident that Campbell (1985) model does not fit well with TCDCs for LC8 because the best-fit R^2 value for LC8 is 0.76 which is appreciably lower than those for ALT29, ALT28 and DC18. This is likely attributed to lack of flexibility for Campbell (1985) model which was used to fit TCDC with single fitting parameter

to capture poorly defined flat tail of LC8 TCDCs. Examination of S_o and clay content of ALT29, ALT28 and DC18 indicates that ALT28 with highest S_o also has the highest clay content of 30.13%. Campbell (1985) found the correlation between S_o and clay content (m_c) in the form:

$$S_o = (0.3073m_c + 0.0334)/n (5-4)$$

Figure 5-5 shows the eq. (5-4) correlations between S_o and m_c when n equals to 0.35, 0.37 and 0.39, respectively. For ALT29, ALT28 and DC18, the best-fit S_o and m_c results plotted as closed symbols did not agree well with the correlation, and eq. (5-4) overestimated the cut-off saturations.

Comparison of the TCDCs between soils compacted dry and wet of optimum in Figure 5-4 indicates that λ_{dopt} is generally lower than λ_{wopt} for ALT29, ALT28 and DC18, but remain relatively similar for LC8. Figure 5-6 is a comparison of λ_{dopt} and λ_{wopt} measurements at the same saturations. Closed symbols denote λ measurements for ALT29, ALT28 and DC18 with the average clay content of 29%, while open symbols denote λ measurements for LC8 with the clay content of 5%. Most of λ values for ALT29, ALT28 and DC18 fall above the 1:1 line and are best fit with a 1.07:1 trend line. This indicates that λ_{wopt} values are approximately 7% higher than λ_{dopt} values for ALT29, ALT28 and DC18. On the other hand, near 1:1 correspondence is evident between λ_{dopt} and λ_{wopt} for LC8. These observations likely reflect the fact that soils with higher clay content yield different soil microstructures when compacted dry and wet of optimum. WOPT samples tend to yield smaller inter-clod voids than those DOPT samples. This may result in more efficient pathways for heat transfer through clod to clod, thus leading to relatively larger thermal conductivity for WOPT samples. Figure 5-7 displays pore-throat size distribution (PSD) curves of DOPT and WOPT samples for DC18. The characteristics of PSD curves for DOPT and WOPT samples are in general accordance with previous studies (e.g., Garcia-Bengochea, 1981; Acar and

Olivieri, 1989; Delage et. al., 1996). The PSD curves show that pore-throat diameters range from about 0.003 to 400µm. The PSD curve for DOPT sample tends to be relatively multimodal with top three peaks at 2.1, 3.6 and 10.3µm, while PSD curve for WOPT sample tends to be relatively unimodal with peak at 1.8µm. Comparison of the PSD curves between DOPT and WOPT samples indicates that WOPT sample yields lower percentage of smaller inter-clod pores than DOPT sample. This could potentially lead to smaller thermal conductivity for soils with high clay content when compacted dry of optimum than wet of optimum.

5.4 SUMMARY

Four different clayey soils, each compacted dry and wet of optimum were tested with single-needle thermal probe for measuring thermal conductivity dryout curves. Results of TCDCs for these soils indicate that soils with higher clay content (clay~30%) have lower saturated thermal conductivities, and more gradual shape in TCDCs than the soil with lower clay content (clay~5%). Comparison between TCDCs obtained for dry and wet of optimum specimens indicates that soils with higher clay content compacted wet of optimum (WOPT) generally have higher thermal conductivity than those compacted dry of optimum (DOPT). On the other hand, for the soil with lower clay content, thermal conductivity values between WOPT and DOPT are comparable. Lower λ for DOPT of clay-rich soils are potentially attributed to larger inter-clod voids for DOPT, which are responsible for less effective heat conduction through clods. Mercury Intrusion Porosimetry (MIP) test were conducted on one of the clay-rich sample, and results indicated that the DOPT sample had higher percentage of larger inter-clod voids than the WOPT sample.

5.5 REFERENCES

- Abdel-Hadi, O. N., and Mitchell, J. K. (1981). "Coupled heat and water flows around buried cables." *J. Geotech. Engrg. Div.*, 107(11), 1461–1487.
- Acar, Y. B., and Olivieri, I. (1989). Pore fluid effects on the fabric and hydraulic conductivity of laboratory-compacted clay. *Transportation Research Record*, (1219).
- ASTM D 7928. (2017). "Standard Test Method for Particle-Size Distribution (Gradation) of Fine-Grained Soils Using the Sedimentation (Hydrometer) Analysis"
- ASTM D 854. (2014). "Standard Test Methods for Specific Gravity of Soil Solids by Water Pycnometer"
- ASTM D 698. (2012). "Standard Test Methods for Laboratory Compaction Characteristics of Soil Using Standard Effort (12,400 ft-lbf/ft³ (600 kN-m/m³))"
- ASTM D 2487. (2011). "Standard Practice for Classification of Soils for Engineering Purposes (Unified Soil Classification System)."
- ASTM D 4404. (2010). "Standard Test Method for Determination of Pore Volume and Pore Volume Distribution of Soil and Rock by Mercury Intrusion Porosimetry"
- ASTM D 6913. (2009). "Standard Test Methods for Particle-Size Distribution (Gradation) of Soils Using Sieve Analysis"
- Benson, C. H., and Daniel, D. E. (1990). Influence of clods on the hydraulic conductivity of compacted clay. *Journal of Geotechnical Engineering*, 116(8), 1231-1248.
- Brandl, H. (2006). "Energy Foundations and Other Thermo-Active Ground Structures." Geotechnique, 56(2), 81–122.

- Campbell, G. S., Jungbauer, J. D., Bidlake, W. R., and Hungerford, R. D. (1994). "Predicting the effect of temperature on soil thermal conductivity." *Soil Sci.*, 158(5), 307-313.
- Campbell, G. S. (1985). Soil Physics with BASIC: Transport Models for Soil-Plant Systems (Vol. 14). Elsevier Science
- Delage, P., Cui, Y. J., and Tang, A. M. (2010). "Clays in radioactive waste disposal." *Journal of Rock Mechanics and Geotechnical Engineering*, 2(2), 111-123.
- Delage, P., Audiguier, M., Cui, Y. J., and Howat, M. D. (1996). Microstructure of a compacted silt. *Canadian Geotechnical Journal*, *33*(1), 150-158.
- de Vries, D.A. (1963). Thermal Properties of Soils. *Physics of Plant Environment*. W.R. van Wijk (ed.). North Holland Pub. Co. Amsterdam: 210-235.
- Diamond, S. (1971). Microstructure and Pore Structure of Impact-Compacted Clays. *Clays and Clay Minerals*, 19, 239-249.
- Fan, R., Jiang, Y., Yao, Y., Shiming, D., and Ma, Z. (2007). "A Study on the Performance Of a Geothermal Heat Exchanger under Coupled Heat Conduction and Groundwater Advection." *Energy*, 32(11), 2199-2209.
- Garcia-Bengochea, I., Lovell, C. W., and Altschaeffl, A. G., "Pore Distribution and Permeability of Silty Clays," *Journal of the Geotechnical Engineering Division*, ASCE, Vol. 105, No. GT7, 1981, pp. 839-856.
- Gurdal, T., Benson, C. and Albright, W. (2003). "Hydrologic properties of final cover soils from the Alternative Cover Assessment Program." Geo Engineering Report 03-02, Geo Engineering Program, University of Wisconsin-Madison.

- Knutsson, S., 1983. On the thermal conductivity and thermal diffusivity of highly compacted bentonite. SKB Report, Swedish Nuclear Fuel and Waste Management Co., SKB 83 72, October 1983.
- Lambe, T. W., "The Engineering Behavior of Compacted Clay," *Journal of the Soil Mechanics and Foundation Division*, ASCE, Vol. 84, No. SM2, 1958, pp.1654-1-1654-34.
- Lu S, Ren TS, Gong YS, Horton R (2007) An Improved Model for Predicting Soil Thermal Conductivity from Water Content at Room Temperature. *Soil Sci. Soc. Am. J.* 71:8–14
- Lu, N. and Dong, Y. (2015). "Closed-Form Equation for Thermal Conductivity of Unsaturated Soils at Room Temperature." *J. Geotech. Geoenviron. Eng.*, 10.1061/(ASCE)GT.1943-5606.0001295, 04015016.
- Olsen, H. W., "Hydraulic Flow through Saturated Clays," *Clays and Clay Minerals*, Vol. 9, 1962, pp. 131-161.
- Pusch, R. (1992). "Use of bentonite for isolation of radioactive waste products." *Clay Miner*. 27(3), 353-361.
- Sepaskhah, A. R., and Boersma, L. (1979). "Thermal conductivity of soils as a function of temperature and water content." *Soil Sci. Soc. Am. J.*, *43*(3), 439-444.
- Shelton, J. (1975). Underground Storage of Heat in Solar Heating Systems. *Solar Energy*, 17(2), 137-143.
- Sloane, R. L., and Kell, T. R. (2013). The fabric of mechanically compacted kaolin. In *Clays and Clay Minerals: Proceedings of the Fourteenth National Conference, Berkeley, California* (p. 289). Elsevier.
- van Genuchten, M.T. (1980). "A closed form equation for predicting the hydraulic conductivity of unsaturated soils," *Soil Science Society of America Journal*, 44: 892-890.

5.6 TABLES

Table 5-1. Summary of index properties for four clayey soils.

Soil ID	Grain Properties					Atterberg Limit		-	Compaction Parameters		Van Genuchten (1980) parameters			
	D ₅₀ (mm)	Clay (%)	Silt (%)	Sand (%)	G_s	LL	PL	PI	$\gamma_{d\text{max}}$ (kN/m^3)	<i>W_{opt}</i> (%)	α (kPa ⁻¹)	S_r	n	m
ALT29	0.0062	28.88	40.87	30.25	2.80	46	24	22	17.72	16.76	0.0133	0.00	1.33	0.25
ALT28	0.0046	30.13	53.84	16.03	2.76	44	26	18	17.80	14.60	0.0021	0.00	1.43	0.30
DC18	0.0091	27.50	72.02	0.48	2.71	40	13	27	16.54	16.24	0.0039	0.00	1.45	0.31
LC8	0.0740	5.30	45.13	49.57	2.64	29	21	8	17.62	12.54	0.0031	0.00	1.19	0.16

Table 5-2. Summary of target and actual dry unit weight (γ_d) and water content (w) for clay specimens

Soil ID	Towart	Target w			Actual w			Actual γ_{dtest}		
	Target γ_d (kN/m ³)	$W_{dopt} \ (\%)$	w_{wopt} (%)		$W_{dopt} \ (\%)$	W_{wopt} $(\%)$		$\gamma_{d(dopt)} \ (kN/m^3)$	$\gamma_{d(wopt)}$ (kN/m^3)	
ALT29	17.34	14.13	18.44		14.36	18.30		17.29	17.35	
ALT28	17.50	12.28	17.60		12.17	17.92		17.50	17.47	
DC18	16.31	14.80	20.30		14.82	20.89		16.19	16.20	
LC8	17.11	10.29	14.80		10.29	14.77		17.09	17.12	

Table 5-3. Saturated thermal conductivity, dry thermal conductivity, critical saturation, and Campbell (1985) modeling parameters for four test soils.

		Saturated	l and Dry	Thermal con	ductivity	Critical	Campbell (1985) Model Parameters					
Soil ID	λ	sat (W/m-K	(2)	λ_{c}	dry (W/m-K	(2)	Saturation		Avg.			
	DOPT	WOPT	AVG	DOPT	WOPT	AVG	, S_{crit}	DOPT	WOPT	AVG	R^2	
ALT29	1.61	1.64	1.63	0.81	0.84	0.82	0.42	0.25	0.19	0.22	0.99	
ALT28	1.63	1.64	1.63	0.73	0.84	0.79	0.50	0.34	0.21	0.28	0.97	
DC18	1.82	1.83	1.83	0.82	0.89	0.85	0.44	0.27	0.15	0.21	0.95	
LC8	2.93	2.54	2.74	0.73	0.75	0.74	0.23	0.36	0.21	0.29	0.76	

5.7 FIGURES

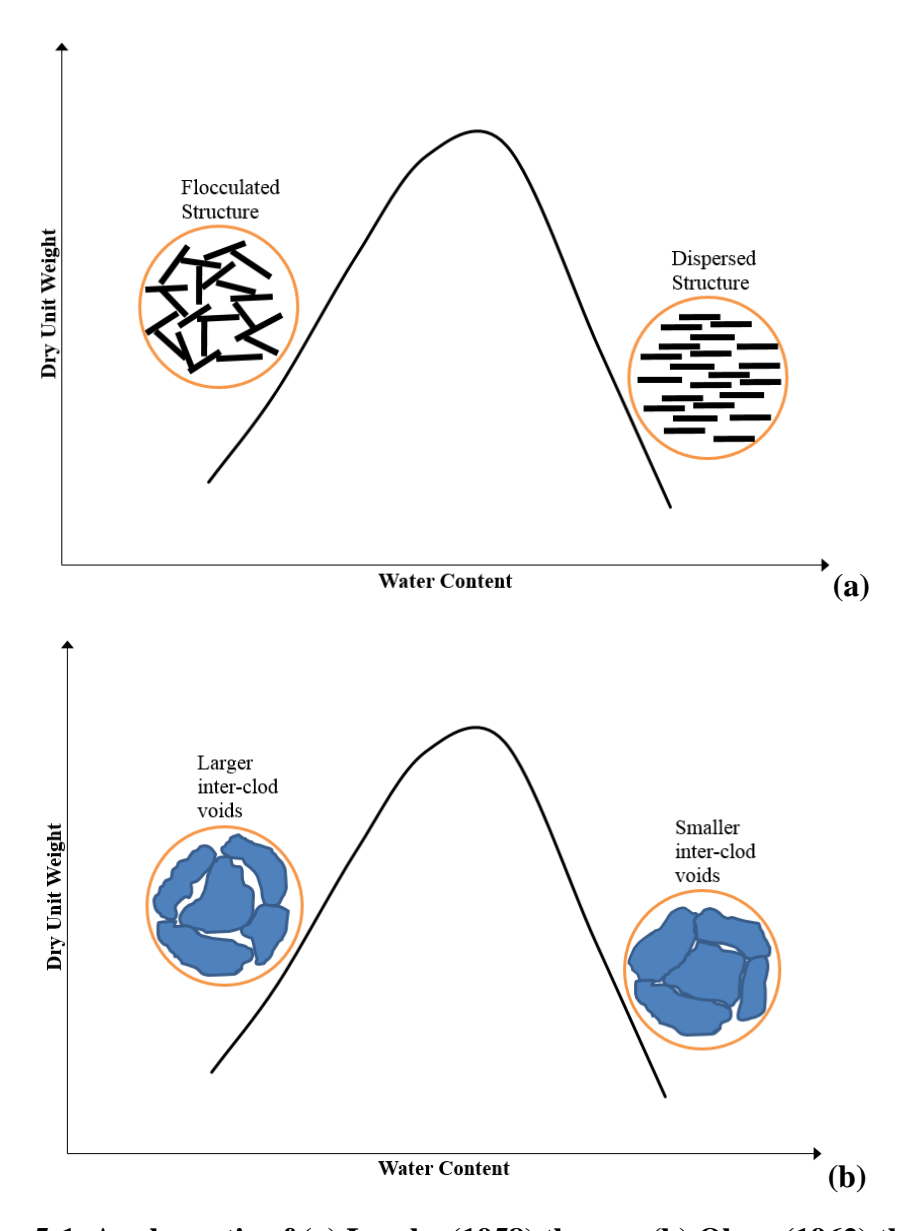


Figure 5-1. A schematic of (a) Lambe (1958) theory; (b) Olsen (1962) theory.

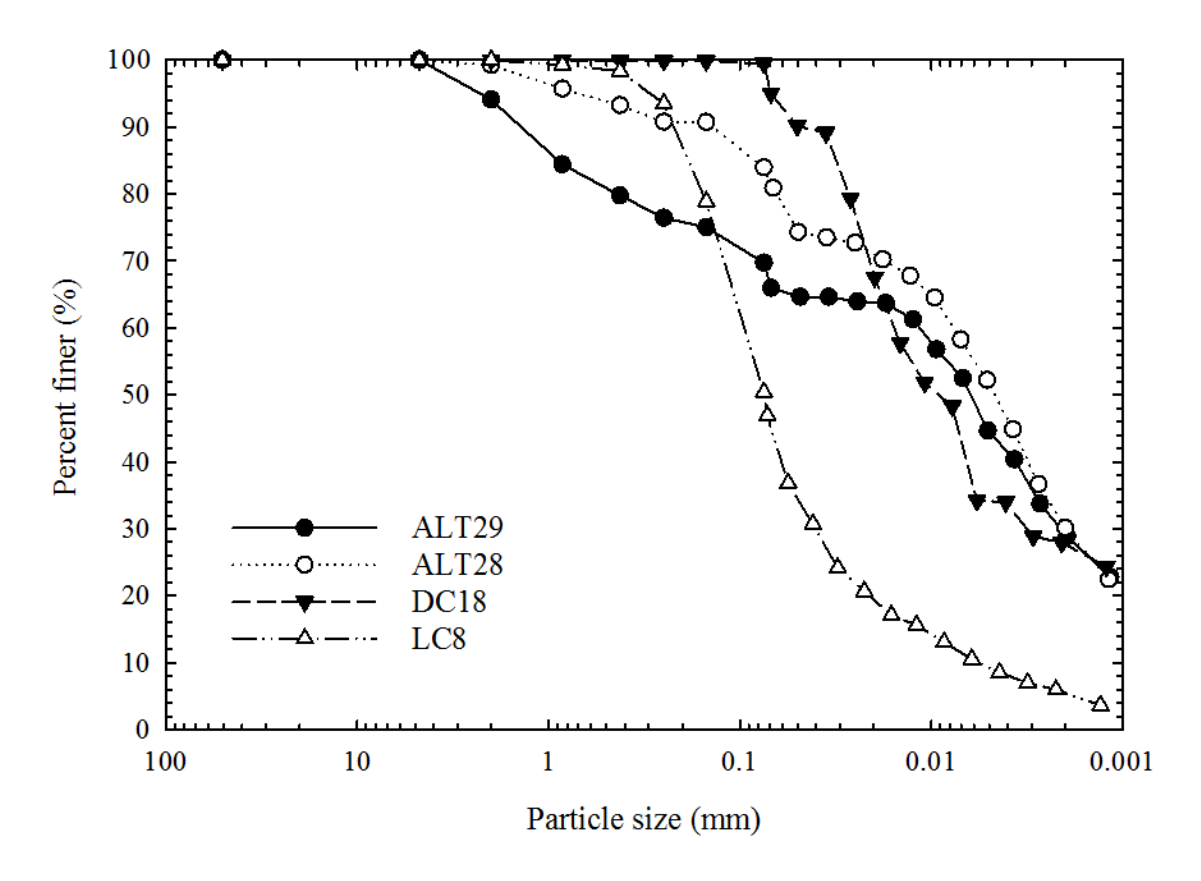


Figure 5-2. Grain size distribution curves of four clayey soils

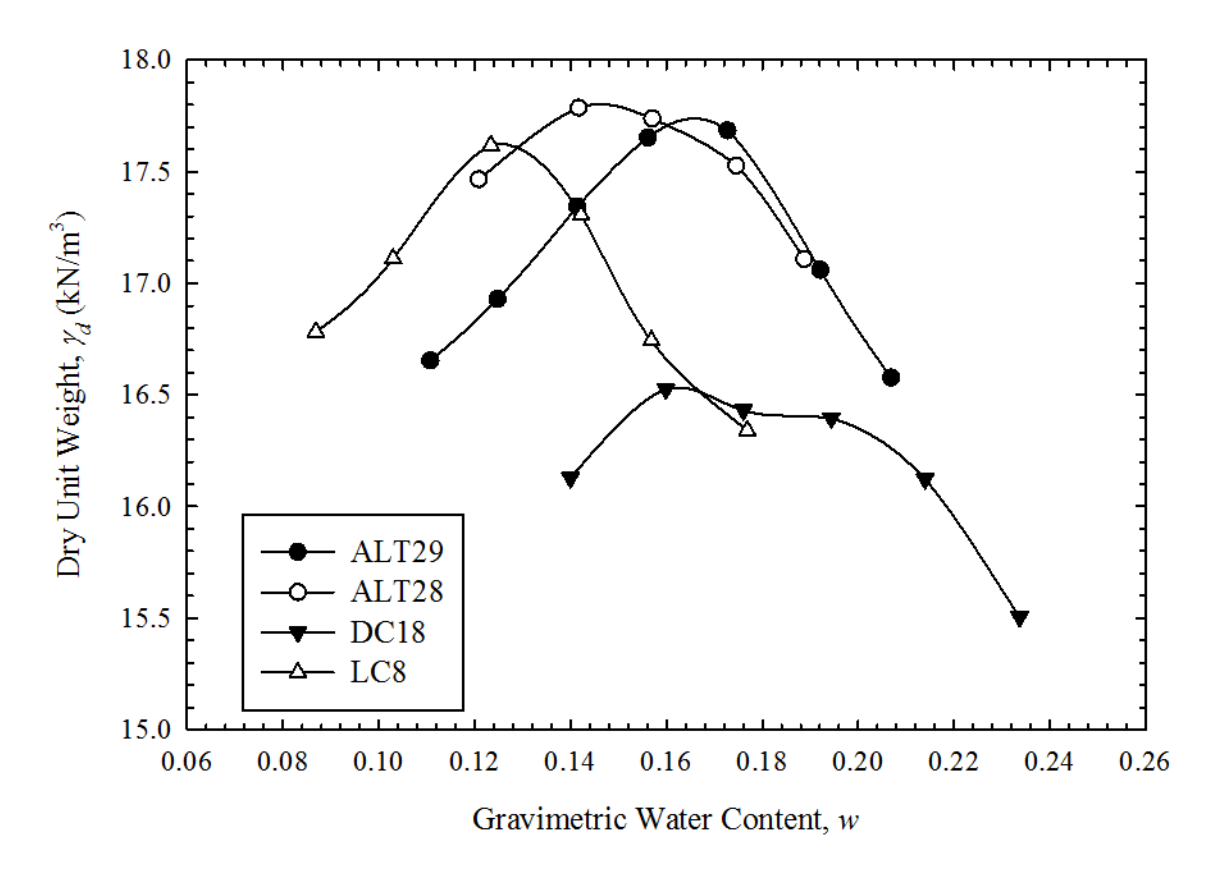


Figure 5-3. Standard Proctor compaction curves of four clayey soils

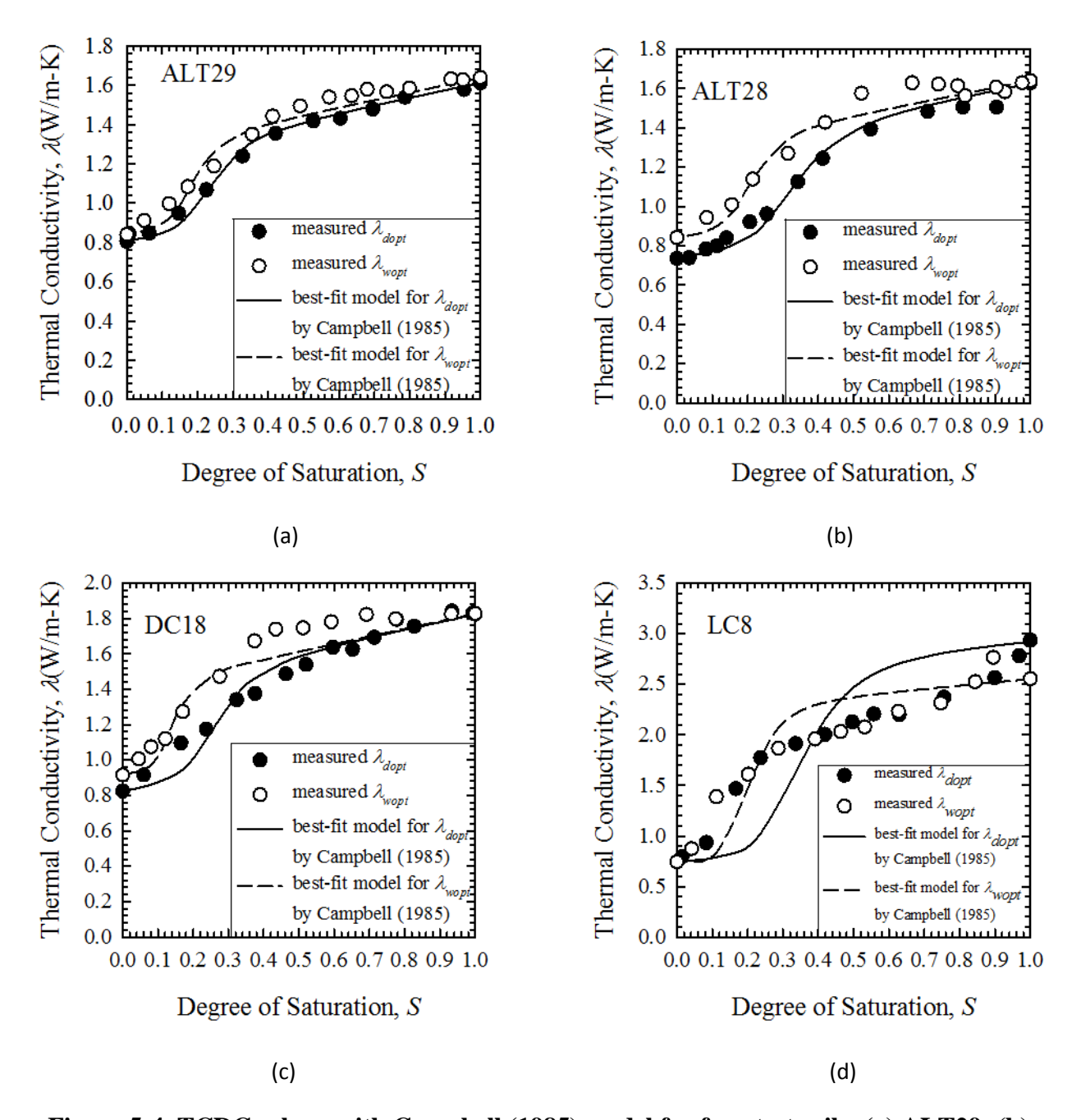


Figure 5-4. TCDCs along with Campbell (1985) model for four test soils: (a) ALT29; (b) ALT28; (c) DC18; (d) LC8.

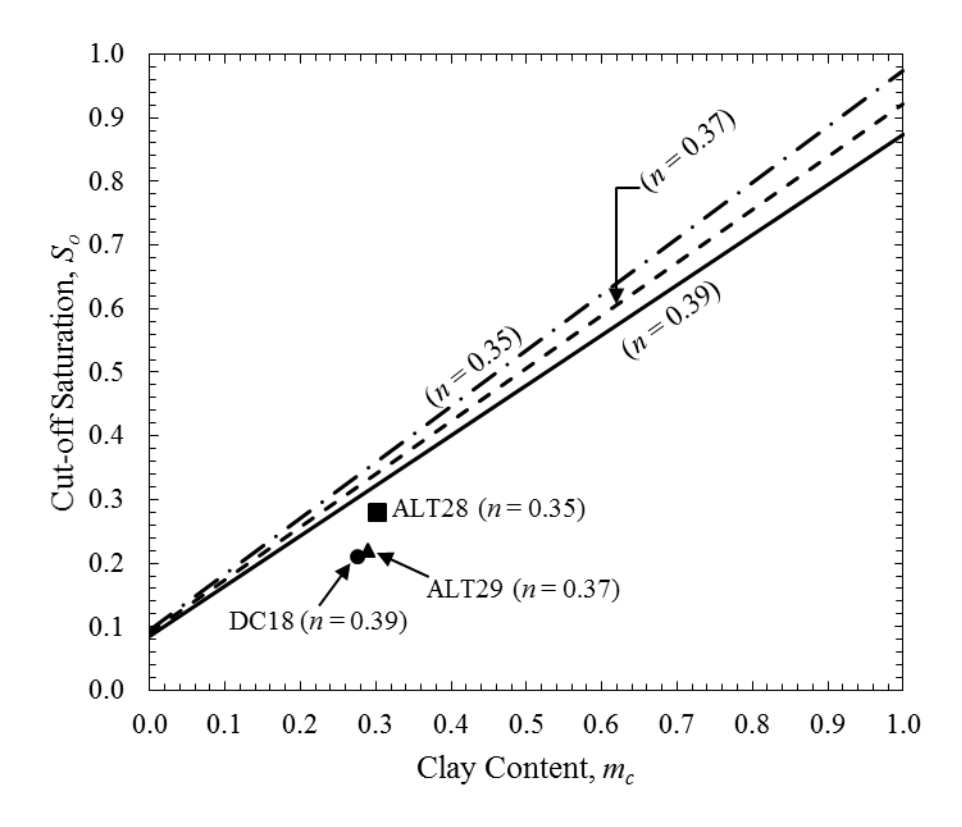


Figure 5-5. Relationships between cut-off saturation and clay content from Campbell (1985) correlation (in dash and solid lines) and actual fitting results from this study (in solid markers)

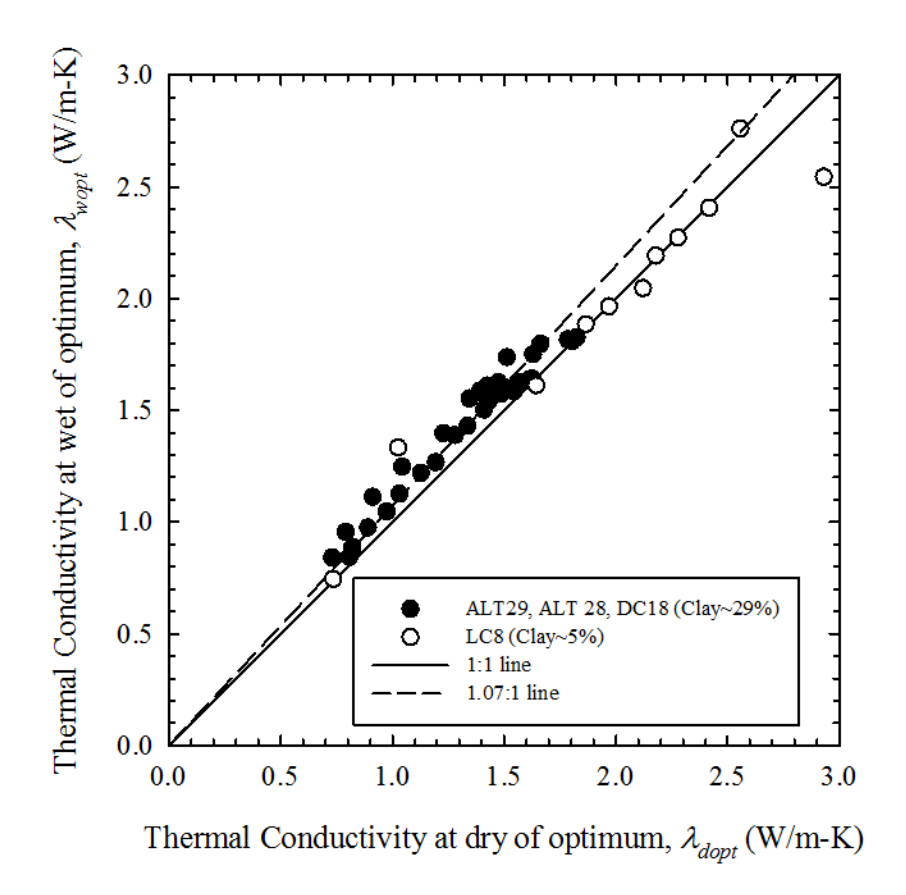


Figure 5-6. Comparison of measured thermal conductivity at wet and dry of optimum.

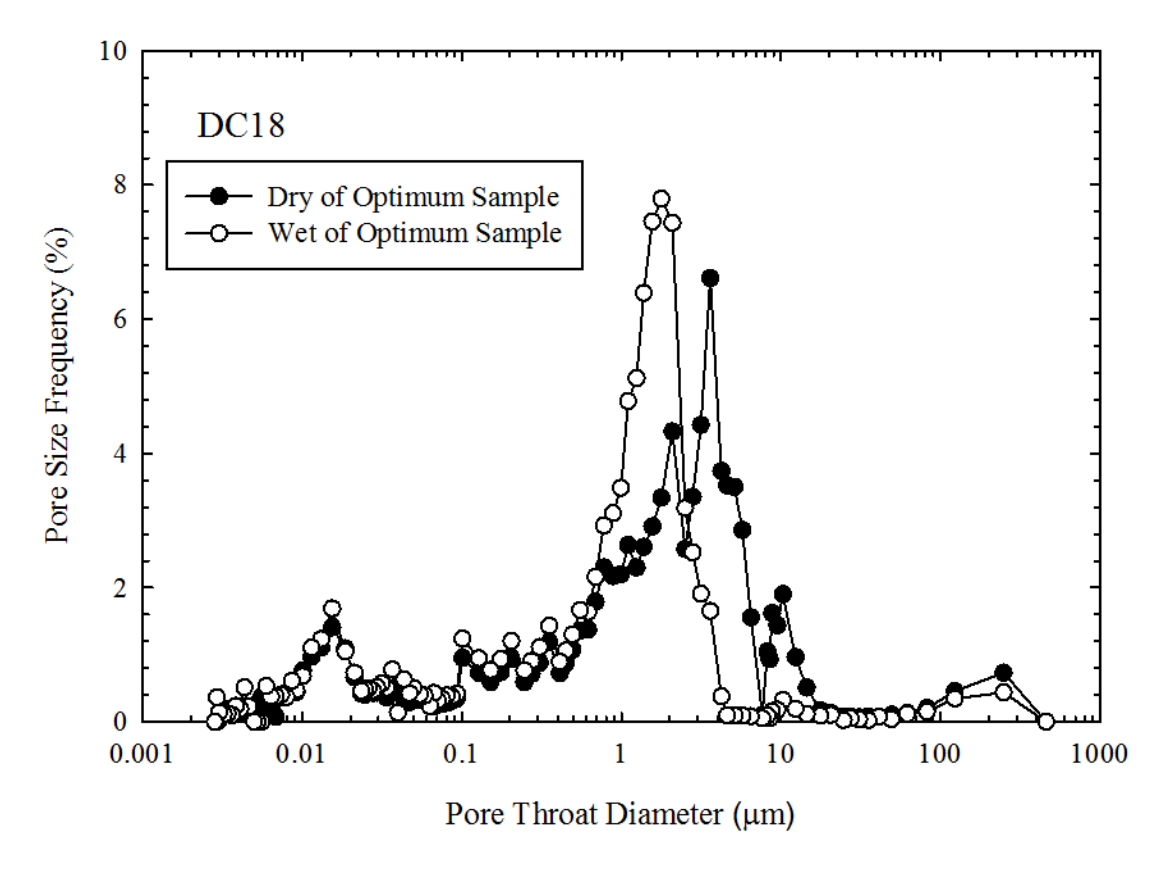


Figure 5-7. Pore size frequency from Mercury Intrusion Porosimetry test for DC18

CHAPTER SIX

COUPLED EFFECTS OF TEMPERATURE AND STRESS LEVEL ON THERMAL CONDUCTIVITY OF UNSATURATED SOILS.

ABSTRACT: Soil thermal conductivity is a function of pore water saturation, temperature and stress level. A suction-controlled thermo-mechanical (SCTM) method has been developed to measure thermal conductivity of unsaturated soils at different temperatures (5.5 °C to 75.5 °C), isotropic normal stresses (35 kPa to 400 kPa), and wetting conditions. The apparatus consists of three main testing systems including temperature-control, pressure-control, and sensor and data acquisition systems. This method permits quantification of thermal conductivity of soils under the influence of stress level and temperature (i.e. construction and environmental conditions). A poorly-graded sand is used to investigate the effects of temperature and stress level on thermal conductivity of unsaturated sands. The thermal conductivity increases appreciably as stress and temperature increases at intermediate saturations ($S \sim 0.3$ to 0.75). Maximum thermal conductivity occurs at 75.5 °C and 400 kPa when S = 0.54 where the value of thermal conductivity is about twice that at 5 °C and 35 kPa. Hysteresis in thermal conductivity with respect to wetting-drying, loading and unloading and heating and cooling was also observed.

6.1 INTRODUCTION

In recent years, soil thermal behavior has received increasing research interest due to its wide applications in the growing field of energy geotechnics, mostly notable in thermo-active structures such as piles, diaphragm walls, retaining walls, embankments, bridge decks and tunnels that utilize ground-source geothermal resources for heating or cooling (Brandl, 2006; Bowers and Olgun, 2014; Laloui *et al.*, 2014). Other energy-related applications include high-level nuclear waste repository, buried high-voltage power cables, and underground thermal energy storage

(Brandon *et al.*, 1989; Alonso *et al.*, 2008; Baser and McCartney, 2015). In these applications, the thermal process is often coupled with complex hydraulic and mechanical processes in soils involving changes in temperature, suction, saturation and stress state. For example, the heat exchange between energy pile and surrounding soil usually causes cyclic temperature change ($\Delta T \sim \pm 15$ °C) which may induce changes in stress state and strain for the soils adjacent to the energy pile (Laloui *et al.*, 2006).

François and Laloui (2008) summarize the primary interactions (labeled as 1 through 4 in Figure 6-1) between thermal, mechanical and hydraulic processes. For the interaction between thermal and mechanical processes, temperature change will result in soil expanding or contracting and depends on the soil type, initial relative density (D_r) or overconsolidation ratio (OCR), confining stress, loading history, heat direction, and draining conditions (Campanella and Mitchell, 1968; Agar et al. 1986). For saturated clay and silt, several previous studies (Towhata et al., 1993; Cekerevac and Laloui, 2004; Abuel-Naga et al., 2007; Vega and McCartney, 2015) found that with temperature increasing (25°C to 85°C) under drained conditions, normally consolidated and lightly overconsolidated (OCR ~ 1.5 to 2) soils consistently contract, while highly overconsolidated (OCR ~ 12) soils initially expand followed by contracting after some transition temperature (55°C to 85°C), which is also dependent on OCR. For saturated sand under drained conditions, Ng et al. (2016) observed the opposite behavior, where loose ($D_r \sim 20\%$) and medium dense ($D_r \sim 70\%$) sands first contracted as temperature increased between 23°C and 35°C and then expanded as temperature continued to increase between 35°C and 50°C. Meanwhile, denser sand $(D_r \sim 90\%)$ only expanded with increasing temperature from 23°C to 50°C. Mitchell and Soga (2005) described two major mechanisms responsible for thermally induced strain (ε_v^T) based on the following relationship:

$$\varepsilon_v^T = \frac{[\Delta V_{dr} - (\alpha_w V_w + \alpha_s V_s)\Delta T]}{V_m} \tag{6-1}$$

where ΔV_{dr} is the volume of drained pore water, α_w and α_s are respectively the volumetric thermal expansion coefficient of water and mineral solid, V_w and V_s are respectively the volume of water and mineral solid, and V_m is the total volume of the bulk sample. First, the solid minerals and pore water will elastically expand with increasing temperature. This is usually considered as reversible strain in total thermally induced strain of the soil. However, the excess pore water pressure will develop because the thermal expansion coefficient of water is about 15 times larger than that of mineral solid (Cui *et al.*, 2000). The significance of this excess pore water pressure also depends on the hydraulic conductivity of the sample. At a given heating rate, the lower the hydraulic conductivity, the longer the time for the excess pore water to dissipate (i.e., longer time for sample bearing lower effective stress). Dissipation of this excess pore water pressure will cause an irreversible plastic strain to the soil sample. The second mechanism is that temperature increase will induce a decrease in inter-particle shearing resistance, resulting in collapse of the soil structure and consequently reduction of void ratio of the sample. This is typically considered as another irreversible strain to the soil.

As discussed above, changes in temperature will greatly affect the stress-strain behavior of soils, but the question towards whether the coupled temperature and stress-strain behavior will affect thermal conductivity of unsaturated soils (illustrated as dotted arrows in Figure 6-1) remains unanswered. Most studies for measuring soil thermal conductivity have been conducted at either ambient temperature (Smits *et al.*, 2010; McCartney *et al.*, 2013; Dong *et al.*, 2015) or low (*e.g.*, geostatic) stress (Yao *et al.*, 2014) or with completely dried soil particles (Yun and Santamarina, 2008; Nasirian et al., 2015), despite the fact that most applications involve coupled thermo-hydro-

mechanical processes (consider an energy pile). In this study, a new suction-controlled thermomechanical (SCTM) method has been developed to measure thermal conductivity of unsaturated sand with carefully controlled temperature (5°C to 75°C), isotropic normal stresses (35 kPa to 400 kPa) and wetting conditions. The primary objective of this study is to investigate the coupled effects of temperature and stress level on the thermal conductivity of unsaturated sand. Hysteresis in thermal conductivity with respect to wetting-drying and loading-unloading is also investigated.

6.2 EXPERIMENTAL PROGRAM

6.2.1 Experimental Set-up

Figure 6-2(a) and (b) show a schematic and a photo of the overall experimental set-up for the suction-controlled thermo-mechanical (SCTM) apparatus. This set-up consists of three main parts including temperature-control system, pressure-control system, and sensor and data acquisition system. The temperature-control system, as detailed in Figure 6-3, is adopted from the heating-cooling system in Soleimanbeigi et. al. (2014). The system has the capability of achieving target temperatures between 5 °C and 90 °C to an accuracy of ± 0.5 °C. Temperatures above or below room temperature are obtained by circulating heated or cooled water in the copper coil from a separate heating or cooling water bath using a pump. The copper coil as shown in Figure 6-3 is placed spirally around the specimen inside the pressure chamber. Silicone tubing with ability to withstand maximum temperature up to 260 °C is used to connect the copper coil through the pump to the water bath. The water bath used for heating direction is heated by a 500-W electrical heating element submerged in the water, while the water bath used for cooling direction is cooled by another copper coil that has cold coolant (~ -23 °C) circulated from a refrigerator using a another pump. During the heating or cooling cycle, temperatures in the bath (T_{bath}) and specimen surface (T_{ss}) are measured by two type-K thermocouples, and monitored by a Labview program through a multiplexer. The Labview program is also used to control the electrical power of the pump and heating or cooling in water bath in order to achieve the target specimen temperature. In order to minimize the heat exchange between the temperature-control system and ambient, the water bath, pressure chamber and silicon tubing are wrapped with fiber glass and foam insulation.

For the pressure-control system, the pressure cell is completely filled with de-aired water, and the top valve (denoted as I in Figure 6-2) is connected with a pressure panel that can monitor the volume of water coming out of the pressure chamber and supply the pressure between -85 and 500 kPa through switching between a vacuum pump and an elevated air-pressure regulator. Matric Suction in the specimen is controlled using the axis-translation technique (Hilf, 1956). Elevated air pressure is supplied through a tube with valve III onto the top of the specimen. A 3-bar (300kPa) high-air-entry (HAE) ceramic disk is integrated into the based pedestal, and the saturated space beneath the ceramic disk is connected with a drainage line through valve V to a jar placed on a high-accuracy (0.01g) electric balance to collect and measure the mass of water outflow. Between valve V and the jar, there is also a Y-shape tube (Figure 6-2(b)) to trap the air bubbles coming out of soil sample. The elevation of the water level in jar is kept the same height as the bottom of the soil specimen. Thus, a set of suction stresses are applied on the specimen by changing the elevated air pressure through the top cap.

The sensor and data acquisition system includes three different sensors connected to their data acquisition systems detailed in Figure 6-4. This allows concurrent and continuous measurements of thermal conductivity, volumetric water content and matric suction. The TR-1 thermal probe is a 10-cm-long, 2.4-mm-diameter, single-needle probe used in conjunction with the KD2-Pro thermal conductivity analyzer (Decagon Devices, Pullman, WA) for measuring soil thermal conductivity. The TR-1 sensor head is accommodated into a 4.0-cm × 2-cm × 1.5-cm

rectangular groove in the top cap. The tensiometer is a small-tip ceramic cup connected through a nylon tube to a differential transducer and data-logger system for measuring matric suction of soils. The nylon tube and ceramic cup are completely saturated with de-aired water before measurements of matric suction. The 5TE moisture sensor is a 3-probe dielectric moisture sensor (Decagon Devices, Pullman, WA) for measuring volumetric water content and temperature of the specimen. The nylon tube for tensiometer, and cables of TR-1 and 5TE sensors were accommodated through special fittings with O-rings inside to prevent loss of cell pressure and exchange of water between soil and cell.

6.2.2 Thermal Calibration

Since changes in temperature and cell pressure may cause volume changes of the pressure cell, cell water, water drainage lines and the ceramic disk, the system is calibrated in order to capture the actual volume change of soil specimen due to temperature and pressure changes. The calibration procedures were adopted from Cekerevac *et al.* (2005). First, an aluminum cylinder with a known volumetric coefficient of thermal expansion (7.1×10⁻⁵ m³/m³-K, Kaiser Aluminum Technical Data Sheet) was selected as a "dummy" specimen. The diameter and height of this aluminum cylinder are respectively 10.16 cm and 15.2 cm, which are exactly same as the dimension of the soil specimen plus the top cap. The set-up for thermal calibration is shown in Figure 6-5. The aluminum cylinder is placed on top of the base pedestal. The thermocouple used for monitoring the temperature of soil sample wall is attached to the wall of aluminum cylinder. After the cell is assembled and filled with de-aired water, all drainage lines and the water compartment beneath the ceramic disk are saturated with de-aired water. The calibration process starts at room temperature (~20 °C) by increasing the cell pressure with a loading-unloading cycle between 35 kPa and 500 kPa. Then the same loading-unloading cycle is followed after heating and

cooling to each target temperature (20 °C – 47.5 °C – 75.5 °C – 47.5 °C – 20 °C – 5.5 °C – 20 °C). The volume of water outflow or inflow from the pressure cell is measured by a graduated burette on pressure-controlling panel. The calibrated volume change of instrument (ΔV_{ins}) due to temperature and cell pressure changes is calculated by the following equation:

$$\Delta V_{ins} = \Delta V_{read} - \alpha_A V_A \Delta T \tag{6-2}$$

where ΔV_{read} is the reading of volume change from the graduated burette due to temperature and pressure changes, α_A is the volumetric coefficient of aluminum cylinder, V_A is the volume of aluminum cylinder, and ΔT is the change of temperature. The reference point for zero ΔV_{cal} is at 20 °C and 35 kPa. Figure 6-6(a) and (b) shows the calibrated volume change with respect to the cell pressure at each temperature for heating and cooling directions, respectively.

6.2.3 Specimen Preparation

SP sand from Chapter 3 is selected for measuring thermal conductivity with controlled changes in suction, effective stress, temperature, loading direction and wetting direction. The index properties including grain size properties (D_{50} , D_{10} , C_u , C_c , G_s) and Van Genuchten (1980) parameters are reported in Table 3-1. The minimum and maximum void ratio for this sand are 0.51 and 0.75, respectively. Prior to the specimen set-up, the ceramic disk is saturated with de-aired water following the procedure suggested by Fredlund and Raharjdo (1993). Then the water compartment beneath the pedestal is saturated with de-aired water by flushing water through drainage lines from valve VI to V (Figure 6-4).

In order to properly set up a sandy specimen, a forming jacket with a neoprene rubber membrane inside is placed over the base pedestal as displayed in Figure 6-7(a). A filter paper is placed on top of the base pedestal to prevent loss of fines through bottom. The airspace between

the inside face of the forming jacket and the membrane is evacuated by applying vacuum through the side hole of the forming jacket. A specific amount of oven-dried sand is then carefully compacted into the forming jacket in four equal layers to reach a target void ratio ($e \sim 0.65$) with the final specimen height of 12 cm. After a second layer is compacted, the tensiometer and 5TE moisture sensors are inserted halfway into the specimen. Then the third and fourth layer are compacted with the tensiometer and 5TE moisture sensor in Figure 6-7(b) held upright. Once the specimen has been formed, a 10-cm-diameter filter paper is placed on top of the specimen, and the TR-1 thermal probe is inserted into the middle of the specimen with the top specimen cap in place. The membrane ends are rolled over the top cap and base pedestal, and the specimen is sealed with O-rings placed on each end where the membrane is adhered to the top cap and base pedestal (Figure 6-8). The top connection line is attached to the top specimen cap. Then a partial vacuum of -35 kPa is applied to the specimen through the top, and the forming jacket is removed. A caliper is used to check the diameter and the height of the specimen after -35 kPa vacuum is applied. The average diameter and height of the specimen are 10.06 cm and 11.9 cm, respectively. Considering the volume of sensors, the actual void ratio of the soil specimen is 0.638 based on the measured dimensions.

After the sensor cables and the nylon tube of tensiometer are fit through the special fittings with O-rings inside on the top plate of the chamber, the pressure chamber is assembled and completely filled with de-aired water. Then the drainage lines through valve VI and V and the water compartment shown in Figure 6-4 are flushed again with de-aired water.

6.2.4 Specimen Saturation

The method suggested by Rad and Clough (1984) was used to saturate the soil specimen until B-value is larger than 0.95. The general idea of this method is to lower the air pressure inside

soil specimen below the atmosphere pressure and saturate the soil with minimum increase in back pressure by letting the water percolate through the vacuumed specimen. A schematic of the sample saturation set-up is shown in Figure 6-9. This set-up consists of two reservoirs with an upper reservoir connected to the bottom and a lower reservoir to the top of soil specimen. The elevation difference between the upper and the lower reservoirs is approximately 1.5 m. These two reservoirs are 50% filled with de-aired water and controlled at the same vacuum pressure initially at -35 kPa by a vacuum regulator (labeled as G2). The cell pressure is controlled by another vacuum regulator (labeled as G1) and is initially set as zero. Since the vacuum used for sand packing is also -35 kPa, the initial effective stress in specimen is 35 kPa. The valve II is kept closed and valve III is open for the air pressures inside soil and the lower reservoir to reach equilibrium. The vacuum pressures inside the cell and two reservoirs are simultaneously increased at the same rate until cell pressure and the reservoir pressure reach -50 kPa and -85 kPa, which indicates the effective stress on specimen is maintained constant at 35 kPa. These two vacuum pressures are kept for about 1 h so that air pressure inside the soil reaches -85 kPa and distributes as evenly as possible. Then the valve II is opened to enable the de-aired water from upper reservoir to percolate through the soil specimen, as driven by the elevation head difference between upper and lower reservoirs. This water percolation process usually takes 10 min to saturate the specimen. After that, the valve III is closed and valve II is left open for another 5 min to ensure pressure equilibrium inside the soil specimen. In order to check the B-value, both valve II and III remain closed, and the cell vacuum pressure is decreased to -25 kPa; thus leading to an excess pore water pressure because of the undrained condition. This excess pore water pressure is measured by a differential pressure transducer, and the B-value is calculated using the equation as follows:

$$B = \frac{\Delta u}{\Delta \sigma_3} \tag{6-3}$$

where $\Delta \sigma_3$ is the change of cell pressure. After the B-value is checked at this step, the vacuum pressure of the upper reservoir is reduced to -60 kPa, and valve II is open again until the change of the water level in upper reservoir is negligible, resulting in effective stress back to equilibrium at 35 kPa. This process is repeated with 25-kPa increments in cell pressure until B-value reaches 95%. In this study, B value reached 96% when cell pressure was increased from 0 to 25 kPa. The final cell pressure is adjusted to 35 kPa while the back pressure is changed to zero by reconnecting the drainage line through valve II to the pressure control panel and reopening valve II.

6.2.5 Testing Procedures

To perform thermal conductivity measurements at different confining stresses, temperatures and suctions, the predefined isotropic net normal stresses (i.e., 35, 100, 200, 400 kPa) and temperatures (i.e., 5.5, 20, 47.5, 75.5 °C), and matric suctions (i.e., 0, 4, 4.5, 5, 5.5, 6, 6.5, 7, 14, 45 kPa) are selected. Figure 6-10 displays the target net normal stress, temperature and matric suction paths of specimen for the test. The saturated specimen (i.e., matric suction is zero) at room temperature (~ 20 °C) under 35-kPa net normal stress is first isotopically and incrementally compressed with each predefined net normal stress (i.e., 100, 200, 400 kPa) for consolidation along Path I (Figure 6-10), and the excess pore water pressure of the specimen at each stress is allowed to dissipate until no visible increase in graduated burette that is connected to the specimen through valve II. Then the saturated specimen is unloaded back to 35 kPa. After the initial loadingunloading cycle, the specimen is heated and cooled to each temperature selections following Path II shown in Figure 6-10. At each temperature, the specimen is allowed to reach the thermal equilibrium for 2 to 3 h, and excess pore water is again allowed to dissipate into graduate burette. The heated or cooled specimen experiences the same loading-unloading cycle between 35 and 400 kPa. After the saturated soil specimen undergoes full heating and cooling cycles (20 - 5.5 - 20 -

47.5 – 75.5 – 47.5 – 20 °C), the next target matric suction from Path III is applied through top of the specimen, and kept for an extended period (~1 day for sand) until the outflow mass collected by the jar reaches equilibrium. At each matric suction, the unsaturated soil specimen undergoes the heating and cooling cycles following Path II, and subsequent loading and unloading cycles following Path I at a given temperature on Path II. Thermal conductivity, volumetric water content and matric suction of the specimen are concurrently measured after equilibrium at the end of each isotropic stress, thermal or matric suction step during the entire drying process.

After the specimen is tested at maximum matric suction (~45 kPa), the top of the specimen is vented to the atmosphere pressure. The specimen will start to imbibe water from the jar due to relatively high matric suction in soil. This wetting process is stopped periodically with 1-day interval. The specimen is then isolated from outside atmosphere and water supply for another 8 hours to reach equilibrium. Then the specimen undergoes single loading-unloading cycle between 35 and 400 kPa. And thermal conductivity, volumetric water content and matric suction are measured at each step. The entire imbibition process stops when the matric suction reading is nearly zero.

Since the soil specimen cannot reach completely or nearly dried condition (below 0.1 saturation) under maximum matric suction (45 kPa), the specimen is opened to the atmosphere and heated under 75.5 °C until no visible air bubble blows through the water in the jar. This thermally dried specimen will be tested following the same loading-unloading, heating-cooling steps as the saturated specimen for thermal conductivity and volumetric water content measurements. It should be noted that the matric suction is not measured for this period because of lost connections between tensiometer and the soil. Table 6-1 summarizes the main test program for each matric suction step and wetting direction for different test purposes.

6.3 RESULTS AND DISCUSSION

Figure 6-11(a) shows the change of measured thermal conductivity with respect to isotropic net normal stresses (σ_c) at 20 °C during the initial isotropic loading-unloading cycle for saturated sand. Thermal conductivity of saturated sand (λ_{sat}) increases with increasing σ_c in loading direction, and decreases in a different path with decreasing σ_c in unloading direction. The average difference of λ_{sat} at the same σ_c between loading and unloading directions is 0.009 W/m-K, which is about 0.3% in difference. This is likely due to the elasto-plastic behavior of the sandy specimen which is evident in Figure 6-11(b). During the first isotropic loading from 35 to 400 kPa, the specimen contracts as volumetric strain (ε_v) increases from 0 to 0.011 and void ratio decreases from 0.638 to 0.620. Thus, the effective thermal conductivity of saturated sand increases as smaller void space is occupied by water with relatively lower thermal conductivity ($\lambda_w \sim 0.6$ W/m-K) than that of sandy particles ($\lambda_s \sim 7.8 \text{ W/m-K}$). When the specimen is unloaded from 400 to 35 kPa, expansion occurs as ε_{ν} decreases by 0.001 which is only one eleventh of change in ε_{ν} while loading. This reflects volume change that is mainly plastic contraction for loading direction while only elastic expansion for unloading direction, which causes an irreversible plastic strain for the specimen. This irreversible plastic strain is why thermal conductivity in unloading direction remains relatively larger than the loading direction at a given σ_c . Figure 6-12 shows the relationship between saturated thermal conductivity and void ratio at 20 °C during initial loading-unloading cycle. The saturated thermal conductivity as a function of void ratio for loading and unloading cycles is obtained through linear curve-fitting as follows:

$$\lambda_{sat}(L) = 4.17 - 1.89e \tag{6-4}$$

$$\lambda_{sat}(UL) = 9.79 - 10.96e \tag{6-5}$$

where $\lambda_{sat}(L)$ and $\lambda_{sat}(UL)$ are the saturated thermal conductivity in initial loading and unloading directions, respectively. Since the plastic strain due to the initial stress loading at 20 °C is not reversible, thermal conductivity, void ratio and volumetric strain at the end of the initial loading-unloading sequence ($\sigma_c = 35 \text{ kPa}$) will be used as a starting point to eliminate the plastic strain solely due to initial stress loading. When the specimen is reloaded or unloaded isotopically between 35 and 400 kPa, the stress-strain changes of the soil specimen will normally follow the same path at the same temperature as the initial unloading path.

The measurements of λ_{sat} for incremental loading steps (35 – 100 – 200 – 400 kPa) in heating direction (5.5 - 20 - 47.5 - 75.5) after the initial loading-unloading cycle are displayed in Figure 6-13 as a function of temperature and isotropic net normal stress. Results show that λ_{sat} follows a generally decreasing trend as temperature increases from 20 to 75.5 °C at each isotropic net normal stress. This is likely attributed to the thermal volumetric expansion of the specimen. Figure 6-14 shows the volumetric strain of the specimen during the same heating and loading cycles. It is evident that the volume of specimen expands ($\varepsilon_{\nu} \sim 0.002$) when temperature reaches 75.5 °C at 35 kPa. The mechanism of volume expansion is explained by Mitchell and Soga (2005) in Eqn. 6-1. Since thermal conductivity was measured after excess pore water pressure dissipated, the volumetric expansion of the bulk specimen due to differential coefficient of thermal expansion between water and solid grain is not considered as a major factor for decrease in saturated thermal conductivity, despite the fact that some local volume expansion due to excess pore water pressure may still exist. Figure 6-15 shows the relationship between volumetric strain of specimen and temperature in heating direction when isotropic net normal stress is at 35 kPa. At the temperatures larger than 20 °C, the experimental ε_{ν} for the specimen is close to the theoretical ε_{ν} for thermal expansion of quartz sand grain suggested by Agar (1984); thus the primary volumetric expansion

is potentially due to the expansion of the solid particles. As solid particles expand with temperature increases, the void space may increase, thus resulting in decrease in thermal conductivity of saturated sand. The minimum λ_{sat} (~2.76 W/m-K) occurs at 35 kPa and 75.5 °C, which are approximately 6.9% lower than λ_{sat} (~2.963 W/m-K) at 35kPa and 20 °C. In Figure 6-15, there is still some difference between the measured ε_{v} of the specimen and theoretical ε_{v} of quartz, especially at 5.5 °C. This is likely due to the rearrangements of the soil particles caused by the thermal reduction of inter-particle shearing resistance (Mitchell and Soga, 2005). Figure 6-16 shows the changes in λ_{sat} and corresponding ε_{v} with respect to σ_{c} in loading direction after each target temperature reached equilibrium. The values of λ_{sat} and ε_{v} increase with σ_{c} at a larger rate than the initial unloading path. This indicates that the thermally-induced plastic strain occurs after heating or cooling the specimen. Although the temperature and stress effects on saturated thermal conductivity was found, the changes in λ_{sat} ranging from 2.76 to 3.10 W/m-K are relatively small given that soil thermal conductivity can change from 0.3 to 4 W/m-K over the full range of saturations.

Effect of temperature and isotropic stress on unsaturated thermal conductivity $(\lambda(S))$

Figure 6-17 shows a series of 3-D plots for measured thermal conductivity as a function of temperature and saturation at different σ_c (e.g., 35, 100, 200, 400 kPa) in heating and loading directions. When σ_c is at 35 kPa (Figure 6-17(a)), thermal conductivity at a given saturation remains relatively constant between 5.5 and 20 °C, but evidently increases as temperature rises from 20 to 75.5 °C. This is likely attributable to the theory of effective thermal conductivity due to latent heat, as explained in Chapter 4. The maximum increase in thermal conductivity occurs near S = 0.3 where thermal conductivity increases from 2.07 to 3.40 W/m-K. This maximum

change in thermal conductivity ($\Delta\lambda \sim 1.33$ W/m-K) due to elevated temperature is smaller than the value ($\Delta\lambda \sim 1.9$ W/m-K) from Chapter 4. Additionally, the saturation corresponding to this maximum change (i.e., critical saturation) is about twice of that ($S \sim 0.15$) reported. This may be attributed to different laboratory techniques used for measuring thermal conductivity of unsaturated sands at elevated temperatures. In Chapter 4, evaporative oven-drying method was used while the specimen is open to the atmosphere resulting in the latent heat of water vaporization is greater than close system used in this Chapter when temperature reaches equilibrium in specimen.

As the specimen is isotropically loaded to 100, 200, and 400 kPa (Figure 6-17 (b), (c), (d), respectively) at given saturations and temperatures, the effect of stress in thermal conductivity become increasingly explicit, most predominant at S = 0.54 and T = 75.5 °C shown as the peak with red color in Figure 6-17 (d). The peak value of thermal conductivity reaches 4.59 W/m-K, which increases 35% from the maximum thermal conductivity (~ 3.4 W/m-K) at 35 kPa and 75.5 °C. Comparing between Figure 6-17 (b), (c), (d) and (a), it is deduced that there are potentially different mechanisms other than latent heat theory leading to enhanced thermal conductivity for different range of saturation because thermal conductivity starts to increase at another saturation ($S \sim 0.54$) other than the peak for thermal conductivity due to latent heat ($S \sim 0.3$).

In order to isolate this enhanced thermal conductivity from the effective thermal conductivity, the differential thermal conductivity with respect to the thermal conductivity when $\sigma_c = 35 \text{ kPa}$ (Figure 6-17 (a)) at a given temperature and saturation was examined. The relationships between this differential thermal conductivity and saturation at the given temperatures are shown in Figure 6-18 (a), (b) and (c). It is evident that the differential thermal conductivity is dependent on temperature, isotropic stress, and saturation, and relatively significant when $T \ge 47.5$ °C, $\sigma_c \ge$

200 kPa and $0.30 \le S \le 0.75$. This saturation range was found to be in the range of funicular regime in soil water characteristic curve (SWCC) in drying direction shown in Figure 6-19. Therefore, the soil behavior in funicular regime is used for describing the first potential mechanism responsible for large increase in this saturation range. In funicular regime, the water drains out of larger pores first followed by smaller pores (Lu and Likos, 2004). When the specimen is maintained at a saturation in funicular regime, heating to a higher temperature (\sim 75 °C) and subsequent isotropic loading may result in more rearrangement of solid particles due to reduction of inter-particle shear resistance (Mitchell and Soga, 2005). This may induce pore water redistribution to balance the temporary change of suction, leading to potential increase in thermal conductivity measurements. In addition, the interfacial surface tension between pore water and solid particle decreases as temperature increases (Romero et al., 2001). This can lead to more pore water reentering the larger void space, leading to enhanced thermal conductivity.

Another potential mechanism is that the shear stiffness decreases as temperature increases, which may result in larger contact area between solid particles under isotropic load (Vargas and McCarthy, 2007). Cho and Santamarina (2001) also suggested that the pore water meniscus may expand due to larger particle contact area caused by externally applied stress as illustrated in Figure 6-20. Thus, as temperature and isotropic net normal stress increase, the heat can pass through the continuous grain-water-grain pathways more efficiently.

Figure 6-21 shows that the measured thermal conductivity of thermally dried specimen increases with respect to the isotropic net normal stresses at different temperatures. This is expected because larger normal stresses would cause the reduction of the void ratio and increased contact area between particles. The average increase of dry thermal conductivity from 35 to 400 kPa at each temperature is 0.103 W/m-K, which is about 23.6% changes of the thermal

conductivity value (\sim 0.436 W/m-K) at 35 kPa and 20 °C. The hysteresis effect with regard to the loading and unloading cycles on thermal conductivity of dry specimen is most noticeable in 75.5 °C, which indicates the specimen may have undergone a small irreversible thermal strain while loading and unloading. The hysteresis effect of drying-wetting direction is shown in Figure 6-22. Between S = 0.2 and S = 0.55, the values of thermal conductivity in wetting direction is consistently lower than those in drying direction. This is potentially due to that specimen is tend to dilate while soil imbibes water as evident in Figure 6-23 showing void ratio during wetting is consistently higher than that during drying.

6.4 SUMMARY

A suction-controlled thermo-mechanical (SCTM) method has been developed to measure thermal conductivity of unsaturated soils at different temperatures (5.5 °C to 75.5 °C), isotropic net normal stresses (35 kPa to 400 kPa), and wetting conditions. The apparatus consists of three main testing systems including temperature-control, pressure-control, and sensor and data acquisition systems. This method permits quantification of thermal conductivity of soils under the influence of stress level and temperature (i.e. construction and environmental conditions). A poorly-graded sand is used to investigate the coupled effects of temperature and stress level on thermal conductivity of unsaturated sands. For saturated sand, thermal conductivity from the initial loading cycle increases with increasing isotropic net normal stress in loading direction, and decreases in a different path with decreasing normal stress in unloading direction due to the irreversible plastic strain. Thermal conductivity of saturated sand also shows decreasing trend as temperature increases potentially due to increasing void space caused by thermal expansion of solid particles during heating. The thermal conductivity increases appreciably as both isotropic net normal stress and temperature increases at intermediate saturations (*S* ~ 0.3 to 0.75). Maximum

thermal conductivity occurs at 75.5 °C and 400 kPa when S = 0.54 where the value of thermal conductivity is 4.59 W/m-K. The potential mechanisms responsible for increasing thermal conductivity in this saturation range are pore water redistribution and larger effective area for heat path due to increased contact area and larger water meniscus between solid particles. Hysteresis in thermal conductivity with respect to wetting-drying direction is also observed due to the dilative pattern of soil specimen in wetting direction.

6.5 REFERENCES

- Abuel-Naga, H. M., Bergado, D. T., and Bouazza, A. (2007). Thermally induced volume change and excess pore water pressure of soft Bangkok clay. *Engineering Geology*, 89(1-2), 144-154.
- Agar, J. G. (1984). Geotechnical behaviour of oil sands at elevated temperatures and pressures.

 PhD thesis, University of Alberta, Edmonton, AB, Canada.
- Alonso, E.E., Springman, S.M., and Ng, C.W.W., 2008, "Monitoring large-scale tests for nuclear waste disposal," *Journal of Geotechnical and Geological Engineering*, 26(6): 817-826.
- Baser T., McCartney J.S. (2015). Development of a full-scale soil-borehole thermal energy storage system. *Proceedings of the International Foundations Conference and Equipment Exposition (IFCEE 2015)*, ASCE GSP 256: 1608–1617.
- Bowers, G.A., and Olgun, C.G. (2014). Ground-source bridge deck deicing systems using energy foundations. *Proceedings of GeoCongress* 2014, ASCE GSP 234: 2705-2714.
- Brandl, H. (2006). "Energy foundations and other thermo-active ground structures." *Geotechnique*, 56(2), 81–122.
- Brandon, T.L., Mitchell, J.K., and Cameron, J.T. (1989). "Thermal instability in buried cable backfills." *J. of Geotechnical Engineering*, ASCE, 115(1), 38-55.

- Campanella, R. G., and Mitchell, J. K. (1968). Influence of temperature variations on soil behavior. *Journal of Soil Mechanics & Foundations Div.*, ASCE, 94(3), 709-734.
- Cekerevac, C., Laloui, L., and Vulliet, L. (2005). A novel triaxial apparatus for thermo-mechanical testing of soils. *Geotechnical Testing Journal*, 28(2), 161-170.
- Cekerevac, C., and Laloui, L. (2004). Experimental study of thermal effects on the mechanical behaviour of a clay. *International journal for numerical and analytical methods in geomechanics*, 28(3), 209-228.
- Cho, G. C., and Santamarina, J. C. (2001). Unsaturated particulate materials—particle-level studies. *Journal of geotechnical and geoenvironmental engineering*, 127(1), 84-96.
- Cui, Y. J., Sultan, N., and Delage, P. (2000). A thermomechanical model for saturated clays. *Canadian Geotechnical Journal*, *37*(3), 607-620.
- Dong, Y., Lu, N., Wayllace, A., & Smits, K. (2015). Measurement of thermal conductivity function of unsaturated soil using a transient water release and imbibition method. *Geotechnical Testing Journal*, *37*(6), 980-990.
- François, B. and Laloui, L. (2008). ACMEG-TS: A Constitutive Model for Unsaturated Soils under Non-Isothermal Conditions. *International Journal for Numerical and Analytical Methods in Geomechanics*. 32: 1955-1988.
- Fredlund, D. G., & Rahardjo, H. (1993). Soil mechanics for unsaturated soils. John Wiley & Sons.
- Hilf, J. W. (1956). An investigation of pore pressure in compacted cohesive soils, Technical Memorandum 654. Denver, CO: US Bureau of Reclamation.
- Lu, N. and Likos, W. J. (2004). *Unsaturated Soil Mechanics*. J. Wiley.
- Laloui, L., and Rotta Loria, A. F. (2016). Multiphysical phenomena and mechanisms involved with energy piles. In *Energy Geotechnics: Proceedings of the 1st International Conference*

- on Energy Geotechnics, ICEGT 2016, Kiel, Germany, 29-31 August 2016 (p. 11). CRC Press.
- Laloui, L., Olgun, C.G., Sutman, M. McCartney, J.S., Coccia, C.J.R., Abuel-Naga, H.M., and Bowers, G.A. (2014). Issues involved with thermo-active geotechnical systems: characterization of thermo-mechanical soil behavior and soil-structure interface behavior. *The Journal of the Deep Foundations Institute*, 8(2), 107-119.
- Laloui, L., Nuth, M., and Vulliet, L. (2006). Experimental and numerical investigations of the behaviour of a heat exchanger pile. *International Journal for Numerical and Analytical Methods in Geomechanics*, 30(8), 763-781.
- McCartney, J. S., Jensen, E., and Counts, B. (2013). *Measurement of subgrade thermal conductivity using a modified triaxial test* (No. 13-1866).
- Mitchell, J. K., and Soga, K. (2005). Fundamentals of soil behavior (Vol. 3). New York: John Wiley & Sons.
- Nasirian, A., Cortes, D. D., and Dai, S. (2015). The physical nature of thermal conduction in dry granular media. *Géotechnique Letter*, 5, 1-5.
- Ng, C. W. W., Wang, S. H., and Zhou, C. (2016). Volume change behaviour of saturated sand under thermal cycles. *Géotechnique Letters*, 6(2), 124-131.
- Rad, N. S., and Clough, G. W. (1984). New procedure for saturating sand specimens. *Journal of Geotechnical Engineering*, 110(9), 1205-1218.
- Romero, E., Gens, A. and Lloret, A. (2001). Temperature Effects on the Hydraulic Behaviour of an Unsaturated Clay. *Geotechnical and Geological Engineering*. 19: 311-332.

- Smits, K. M., Sakaki, T., Limsuwat, A., and Illangasekare, T. H. (2010). "Thermal conductivity of sands under varying moisture and porosity in drainage-wetting Cycles." *Vadose Zone Journal*, *9*(1), 1-9.
- Soleimanbeigi, A., Edil, T. B., and Benson, C. H. (2014). Creep response of recycled asphalt shingles. *Canadian Geotechnical Journal*, *51*(1), 103-114.
- Towhata, I., Kuntiwattanaku, P., Seko, I., and Ohishi, K. (1993). Volume change of clays induced by heating as observed in consolidation tests. *Soils and Foundations*, *33*(4), 170-183.
- van Genuchten, M.T. (1980). "A closed form equation for predicting the hydraulic conductivity of unsaturated soils," *Soil Science Society of America Journal*, 44: 892-890.
- Vargas, W. L., and McCarthy, J. J. (2007). Thermal expansion effects and heat conduction in granular materials. *Physical Review E*, 76(4), 041301.
- Vega, A., and McCartney, J. S. (2015). Cyclic heating effects on thermal volume change of silt. *Environmental Geotechnics*, 2(5), 257-268.
- Yao, J., Oh, H., Likos, W. J., and Tinjum, J. M. (2014). "Three laboratory methods for measuring thermal resistivity dryout curves of coarse-grained soils." *J. ASTM Geotech. Test.*, 37(6), 1-12.
- Yun, T. S., and Santamarina, J. C. (2008). Fundamental study of thermal conduction in dry soils. *Granular matter*, 10(3), 197.

6.6 TABLE

Table 6-1. Summarized test program for different matric suction steps

Matric Suction steps (Path III)	Isotropic net normal stresses (Path I)	Temperatures (Path II)	Test purpose
Saturated (i.e. suction is zero) and thermally dried Soil	35 - 100 - 200 - 400 - 200 - 100 - 35 kPa	20 - 5.5 - 20 - 47.5 - 75.5 - 47.5 - 20 °C	Changes in thermal conductivity with respect to loading-unloading stresses and heating-cooling temperatures
4-kPa, 4.5-kPa, 5-kPa, 5.5-kPa, 6.5-kPa, 7-kPa, 14-kPa and 45-kPa target matric suctions in drying direction	35 - 100 - 200 - 400 - 35 kPa	5.5 – 20 – 47.5 – 75.5 – 20 °C	Changes in thermal conductivity with respect to loading stresses and heating temperatures only
Measured matric suctions in wetting direction	35 kPa	20 °C	Changes in thermal conductivity with respect to wetting direction

6.7 FIGURES

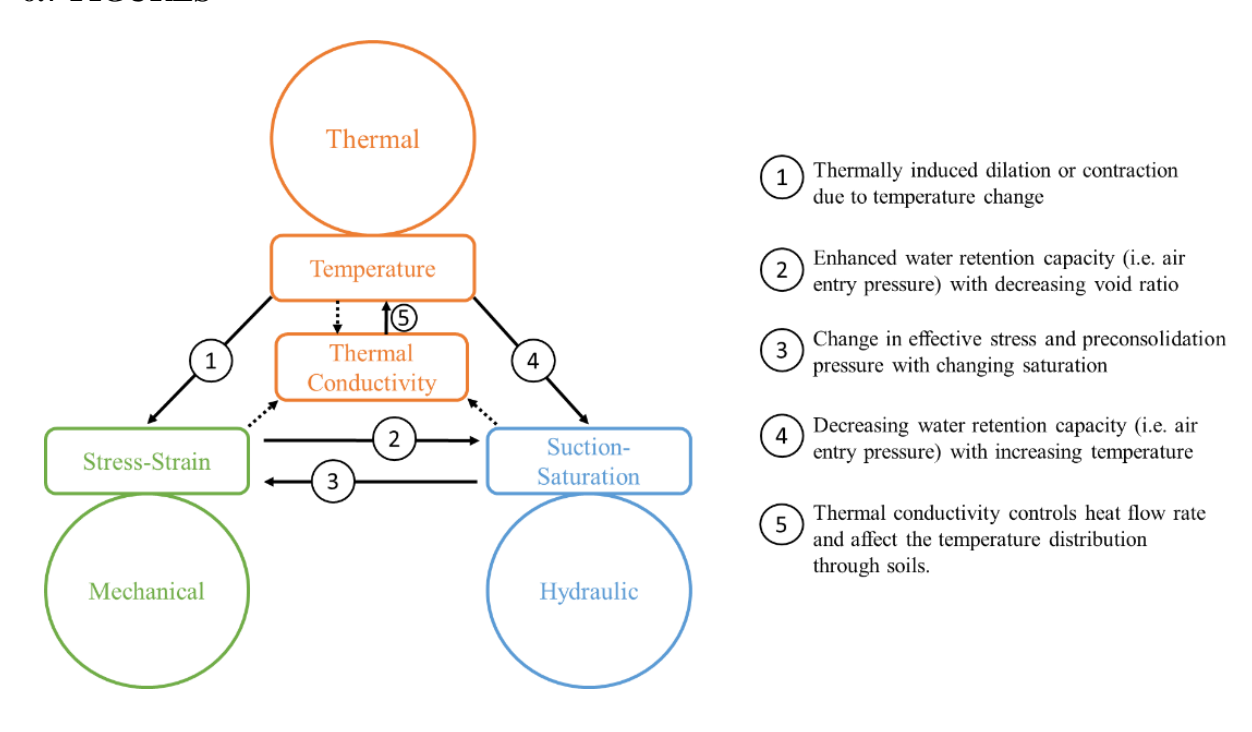
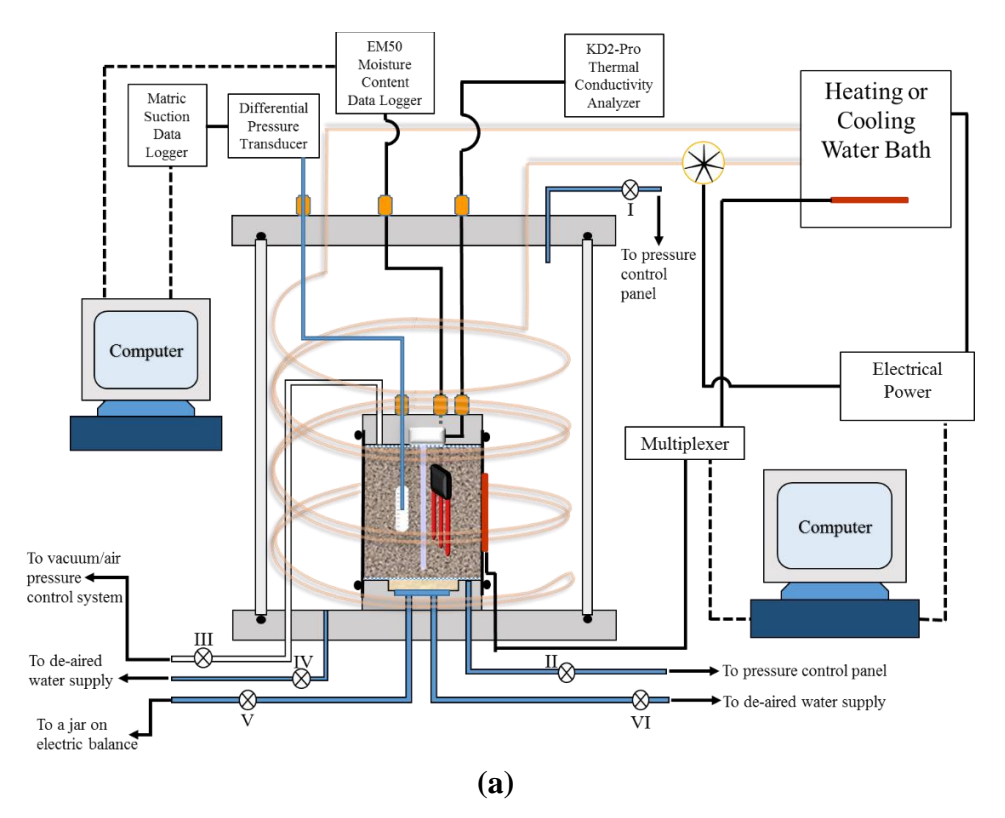


Figure 6-1. Primary coupled thermo-hydro-mechanical processes in soils (after François and Laloui, 2008)



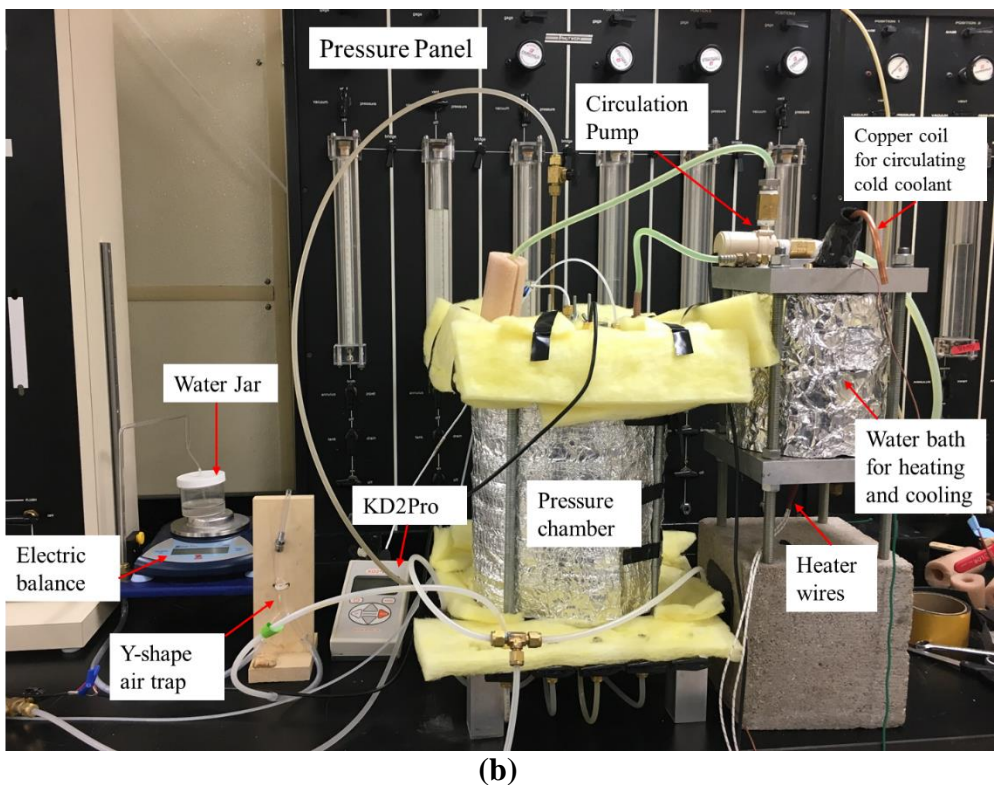


Figure 6-2: (a) Schematic and (b) Photo of Suction-Controlled Thermo-Mechanical (SCTM) apparatus

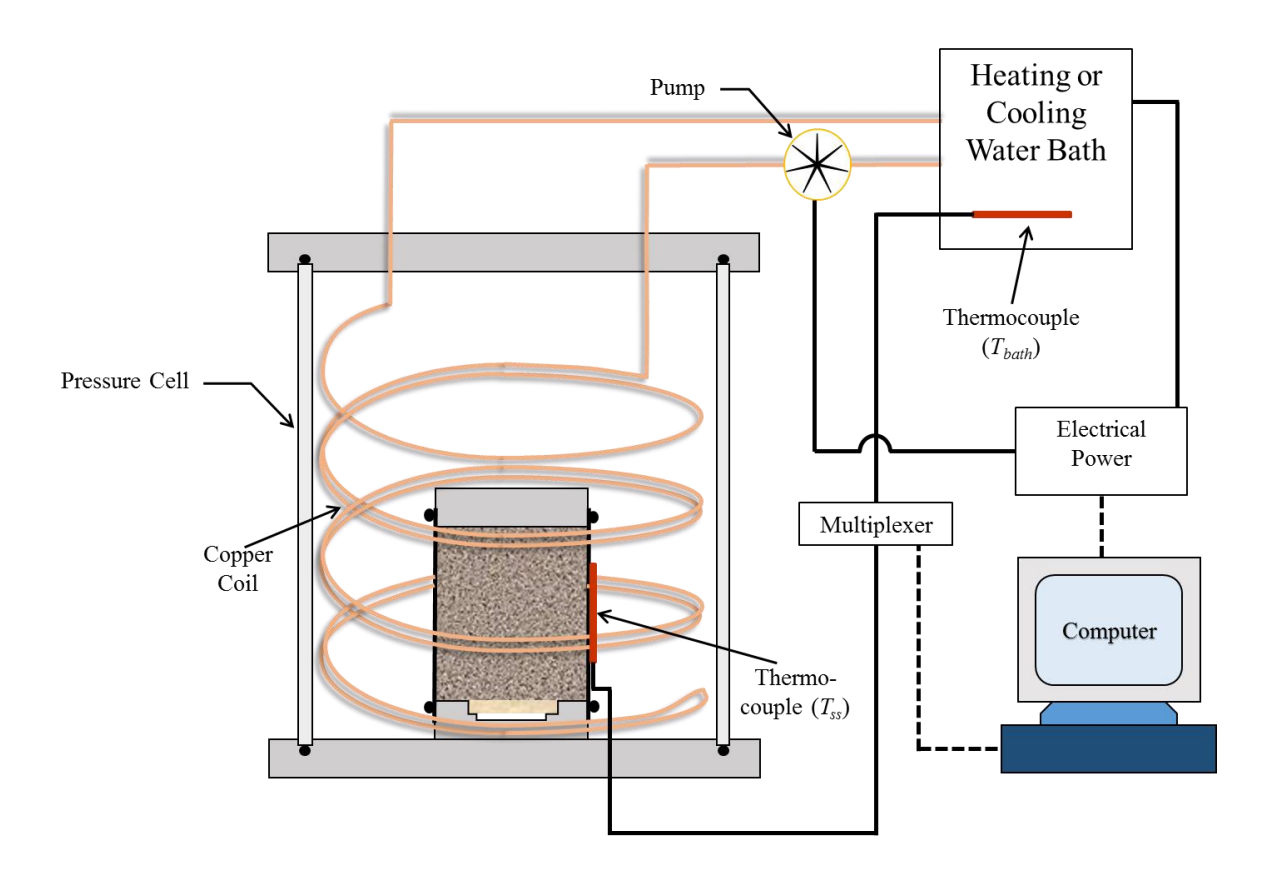


Figure 6-3. Temperature-Controlling System (TCS) in SCTM apparatus

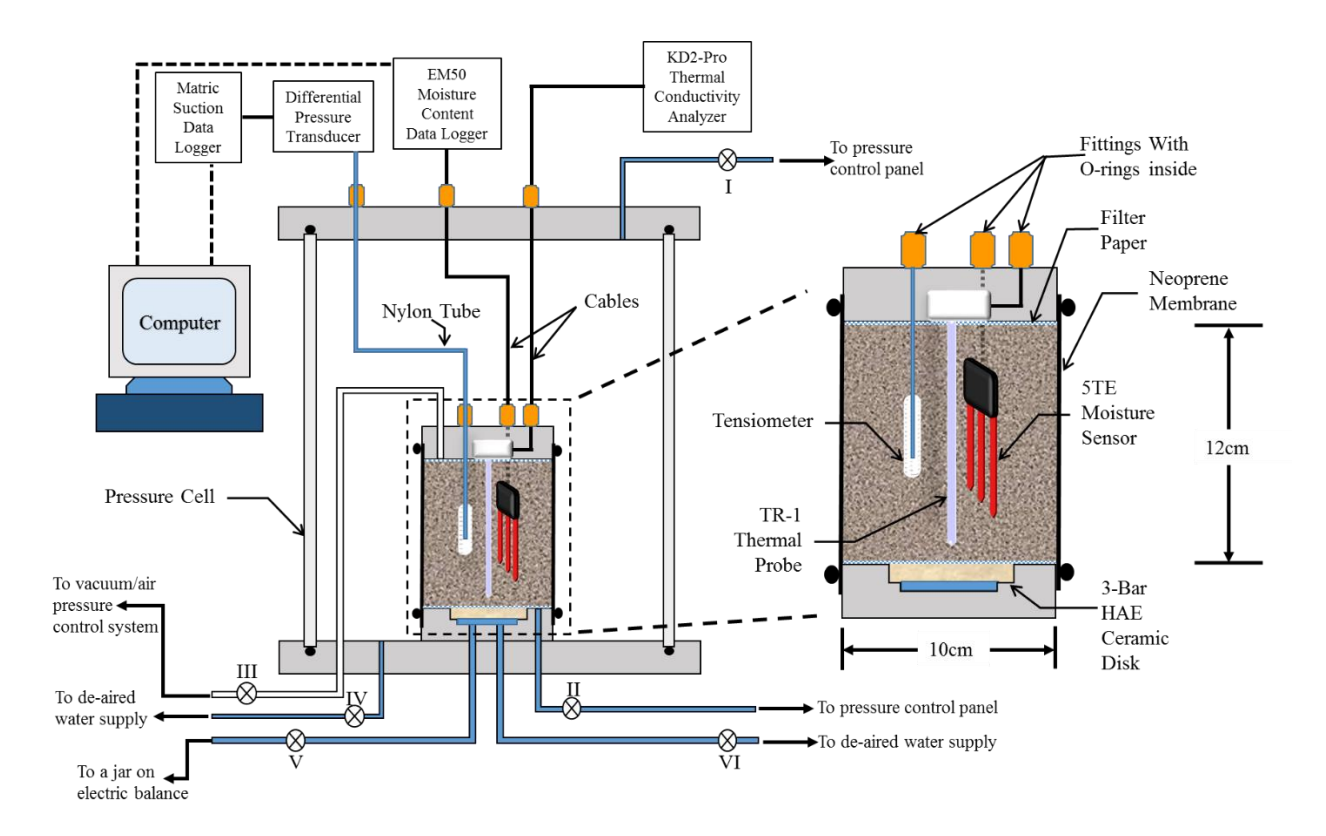


Figure 6-4. SCTM apparatus (TCS omitted) with specific sensor designations

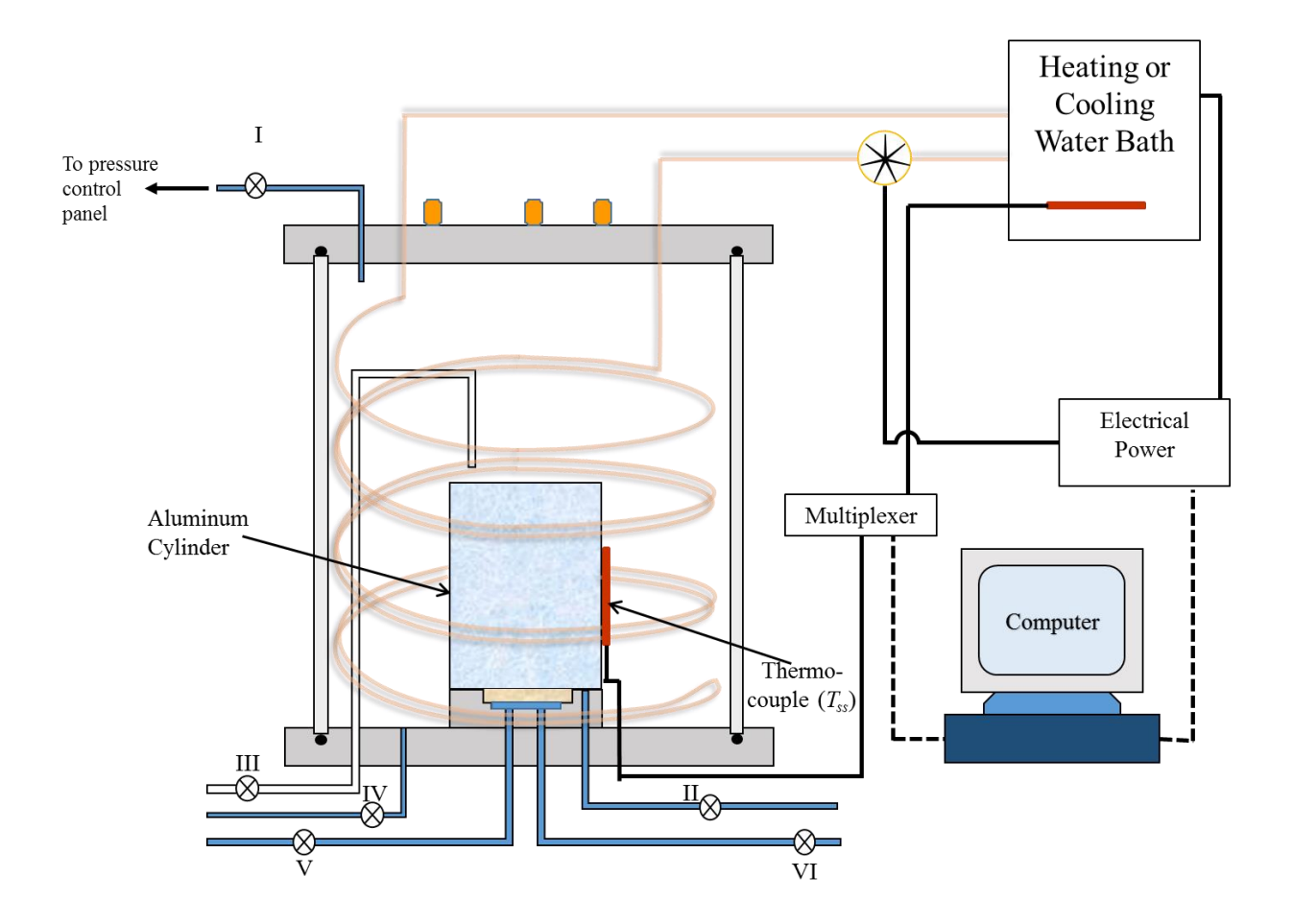


Figure 6-5. Schematic of thermal calibration set-up

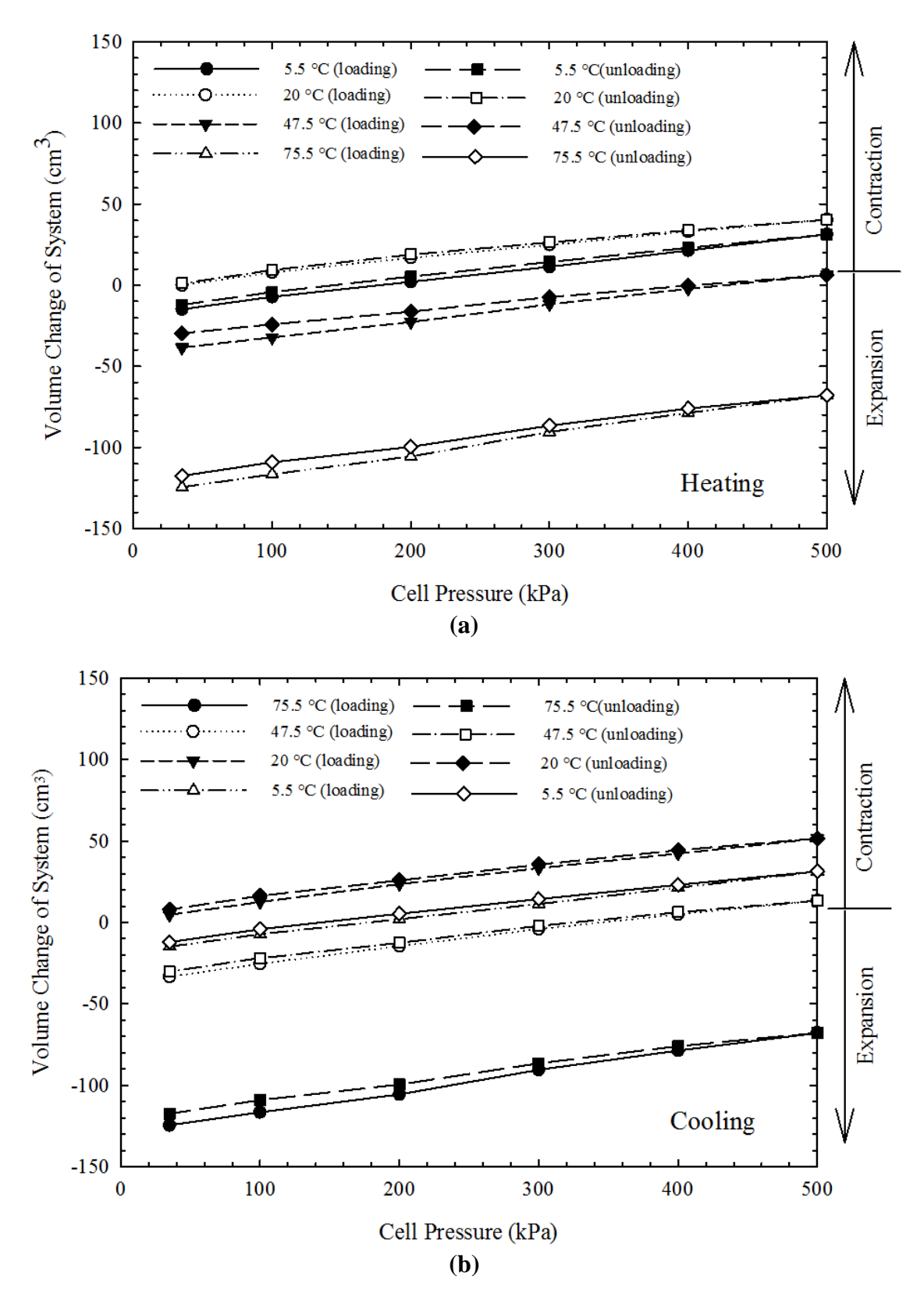
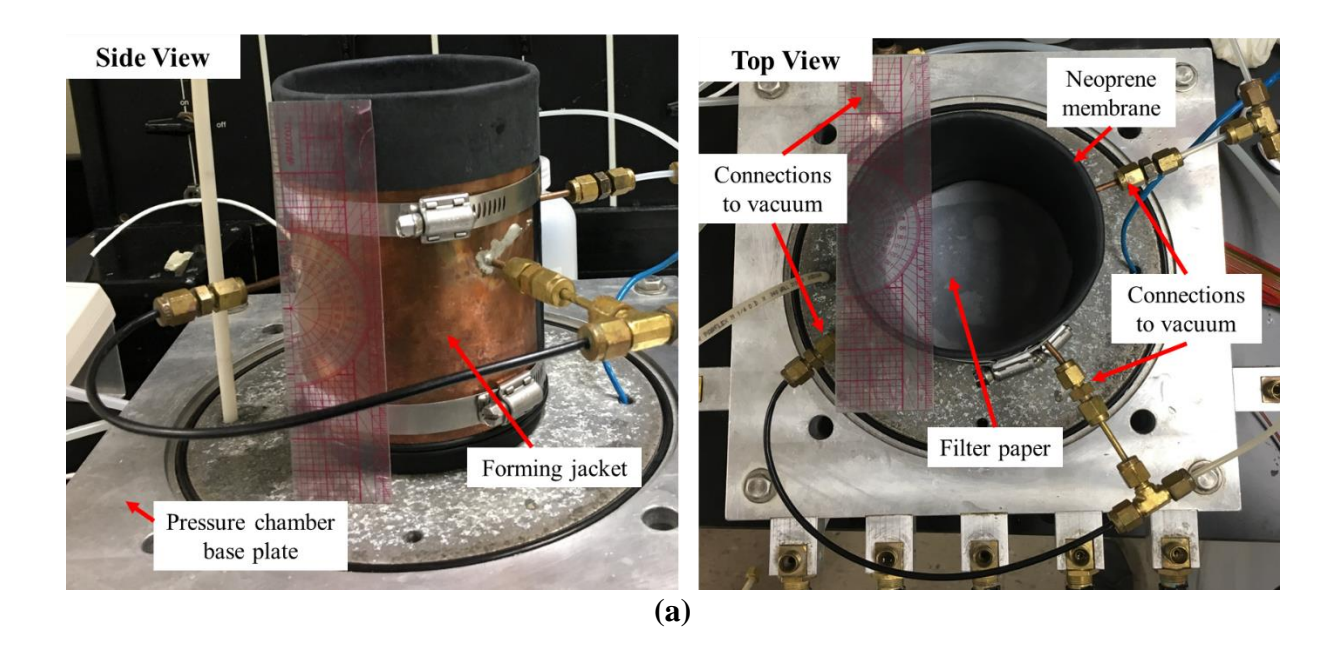


Figure 6-6. Thermal calibration curves for (a) heating and (b) cooling directions



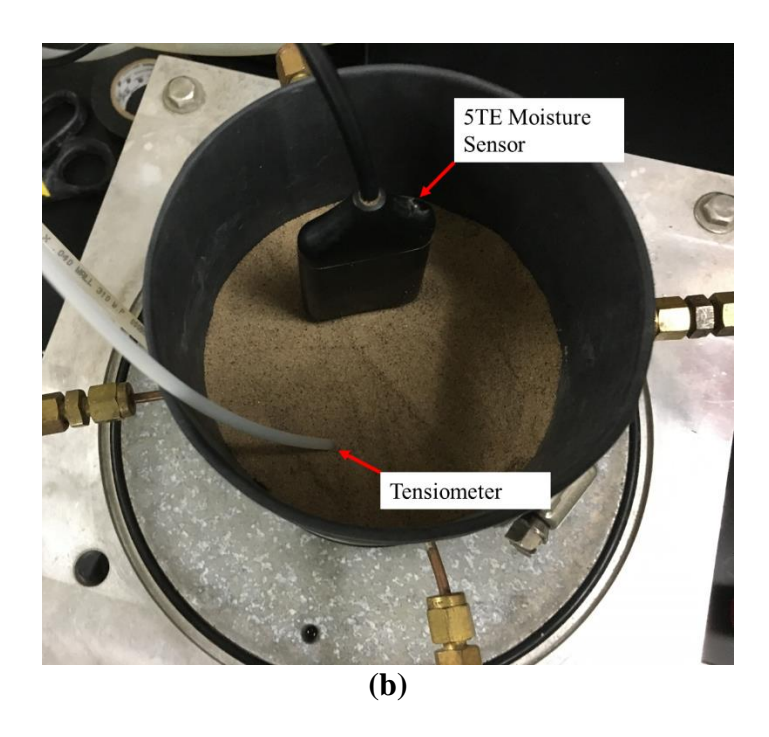
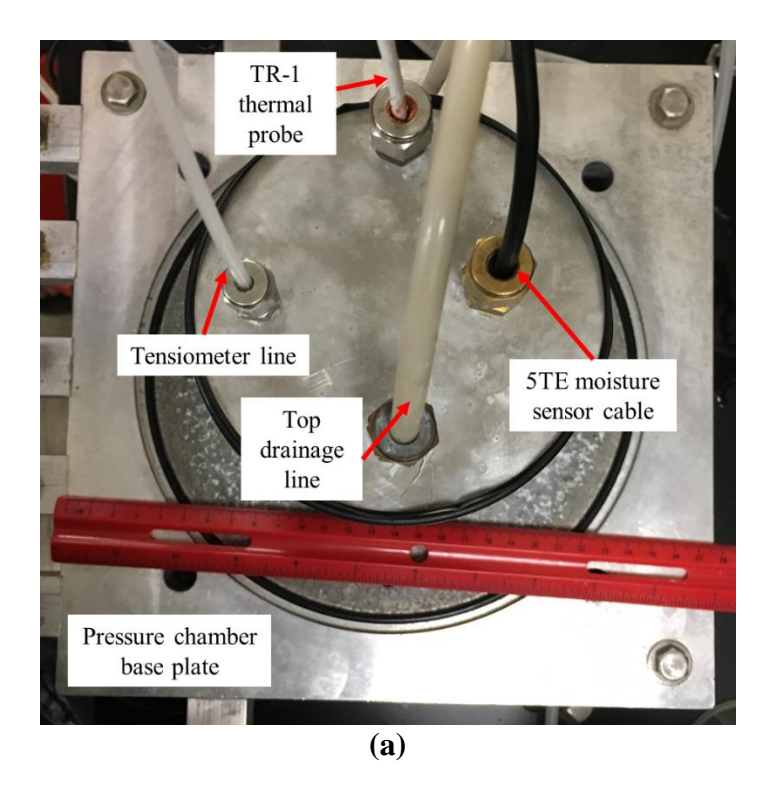


Figure 6-7. Photos of specimen set-up: (a) forming jackets with neoprene membrane; (b) sensor embedding after second layer of soil



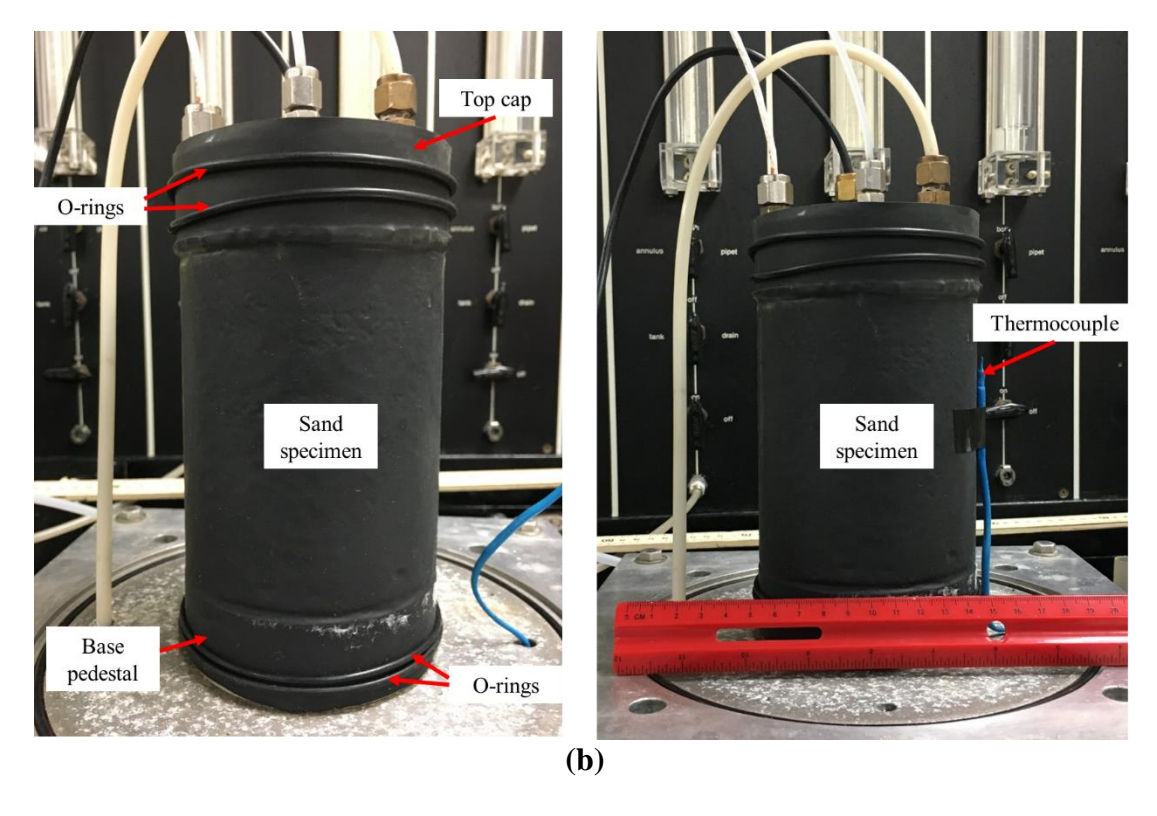


Figure 6-8. Photos of packed specimen with sensors: (a) top view of layout of sensor cables and lines; (b) side view of specimen with O-rings and thermocouple.

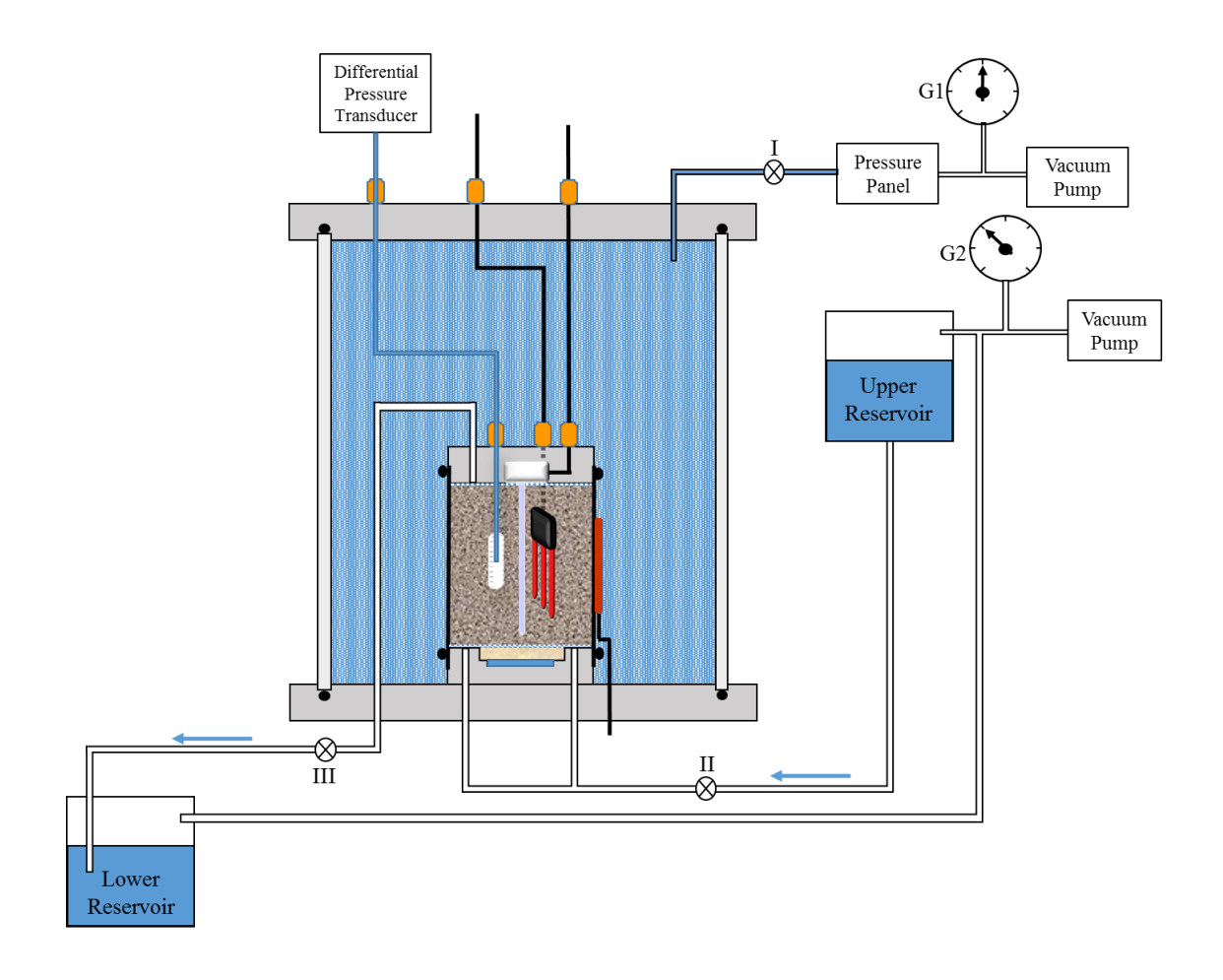


Figure 6-9. Schematic of specimen saturation set-up

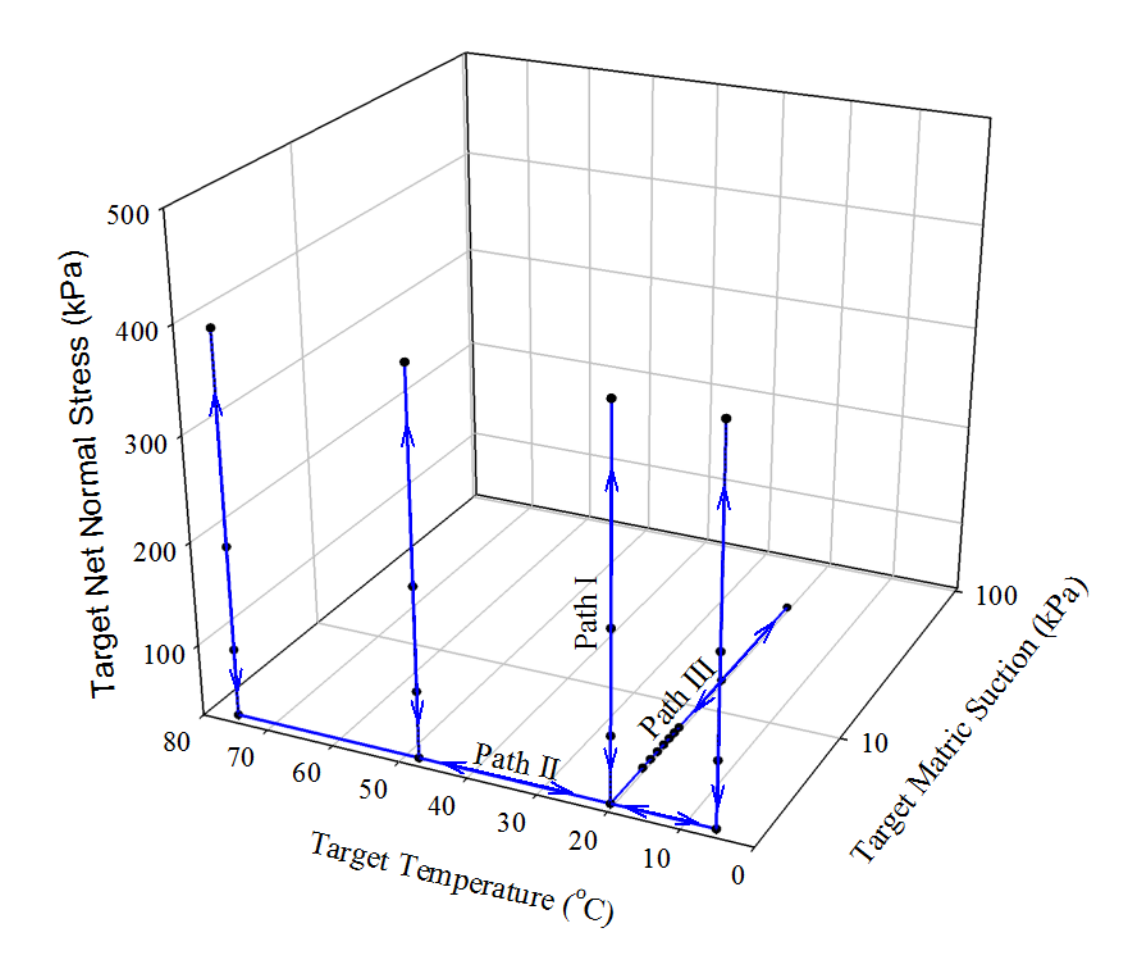


Figure 6-10. Temperature, isotropic net normal stress and matric suction paths of the soil specimen test procedures

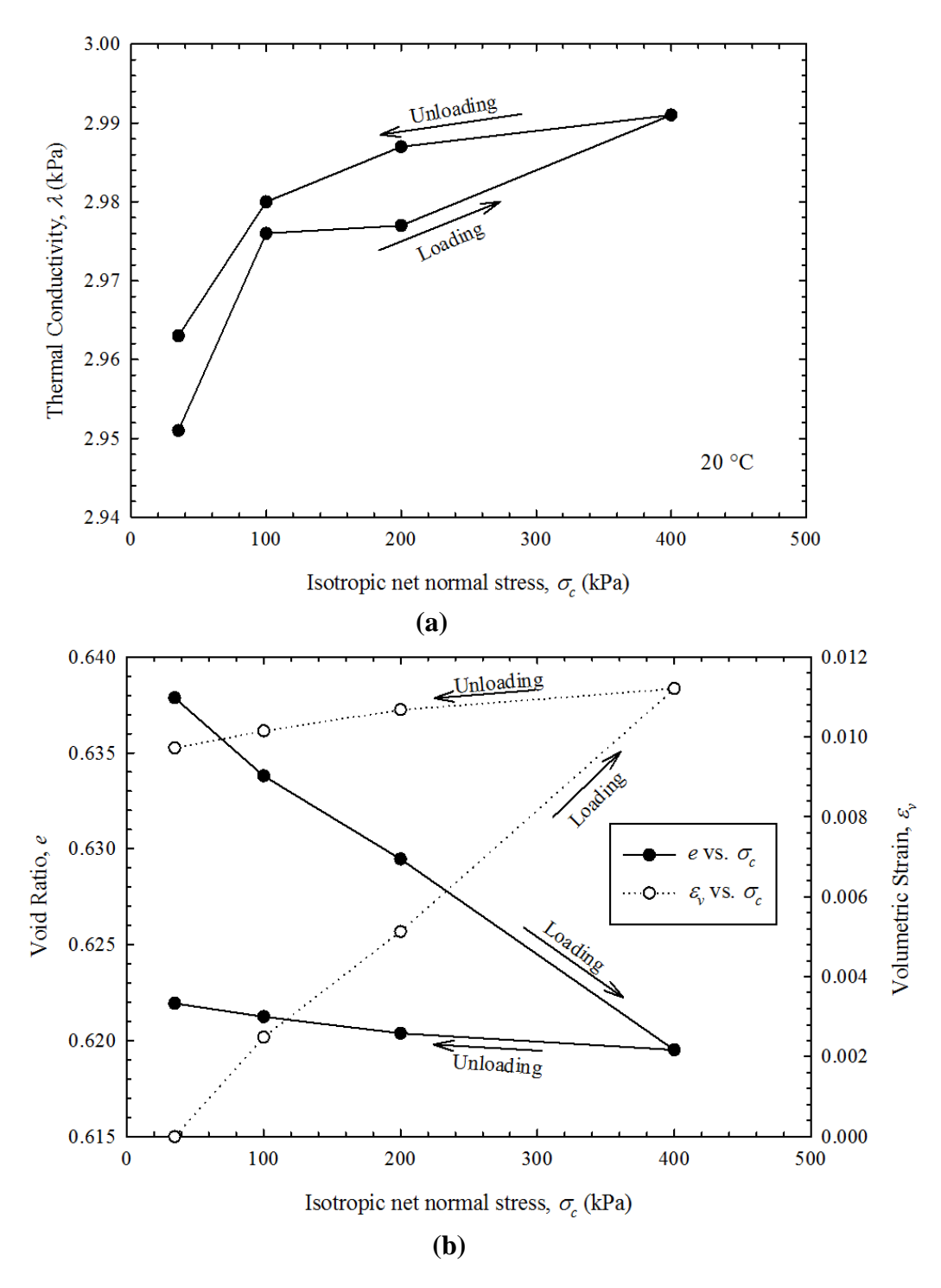


Figure 6-11. Results from (a) thermal conductivity and (b) void ratio and volumetric strain as a function of isotropic net normal stresses at 20 °C during initial loading-unloading cycle for saturated sand (S = 1).

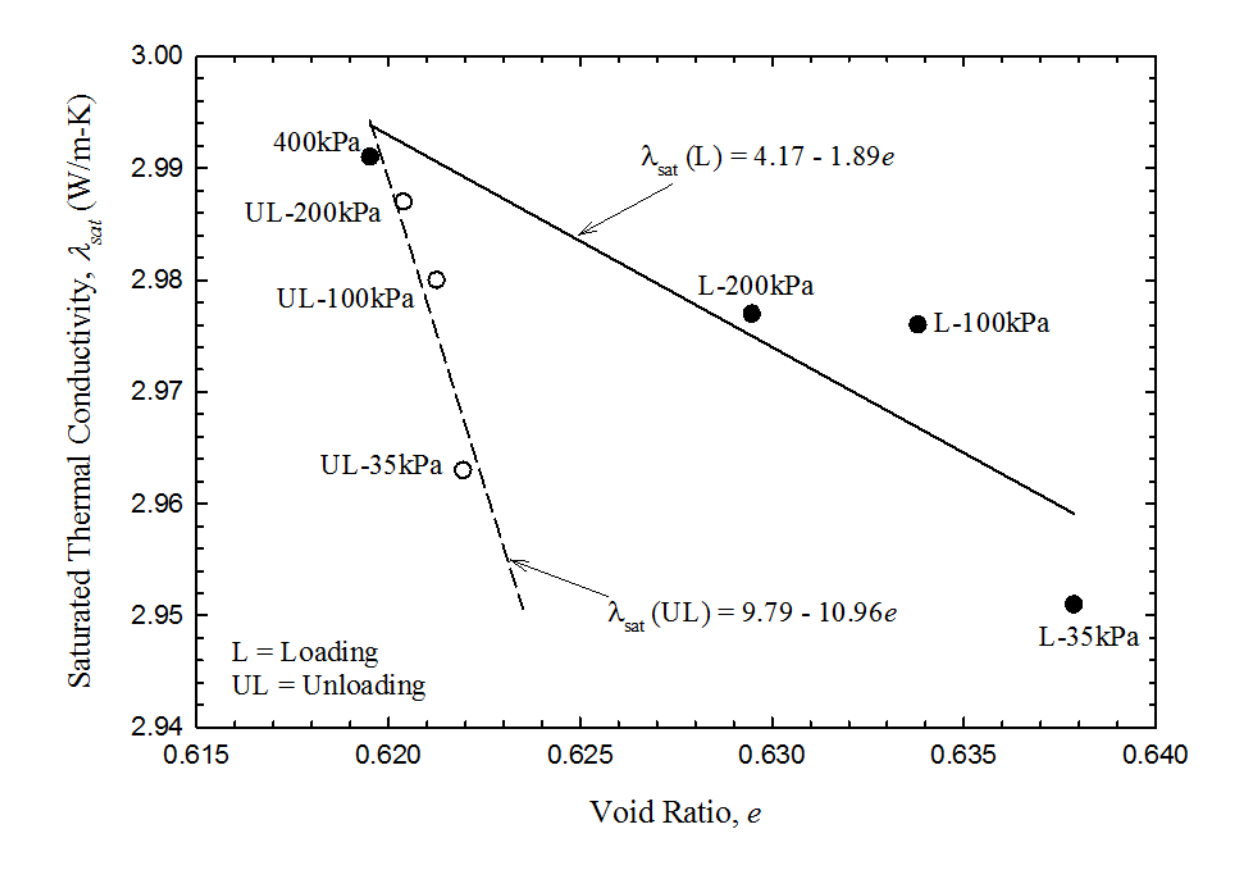


Figure 6-12. The relationship between saturated thermal conductivity (λ_{sat}) and void ratio at 20 °C during initial loading-unloading cycle.

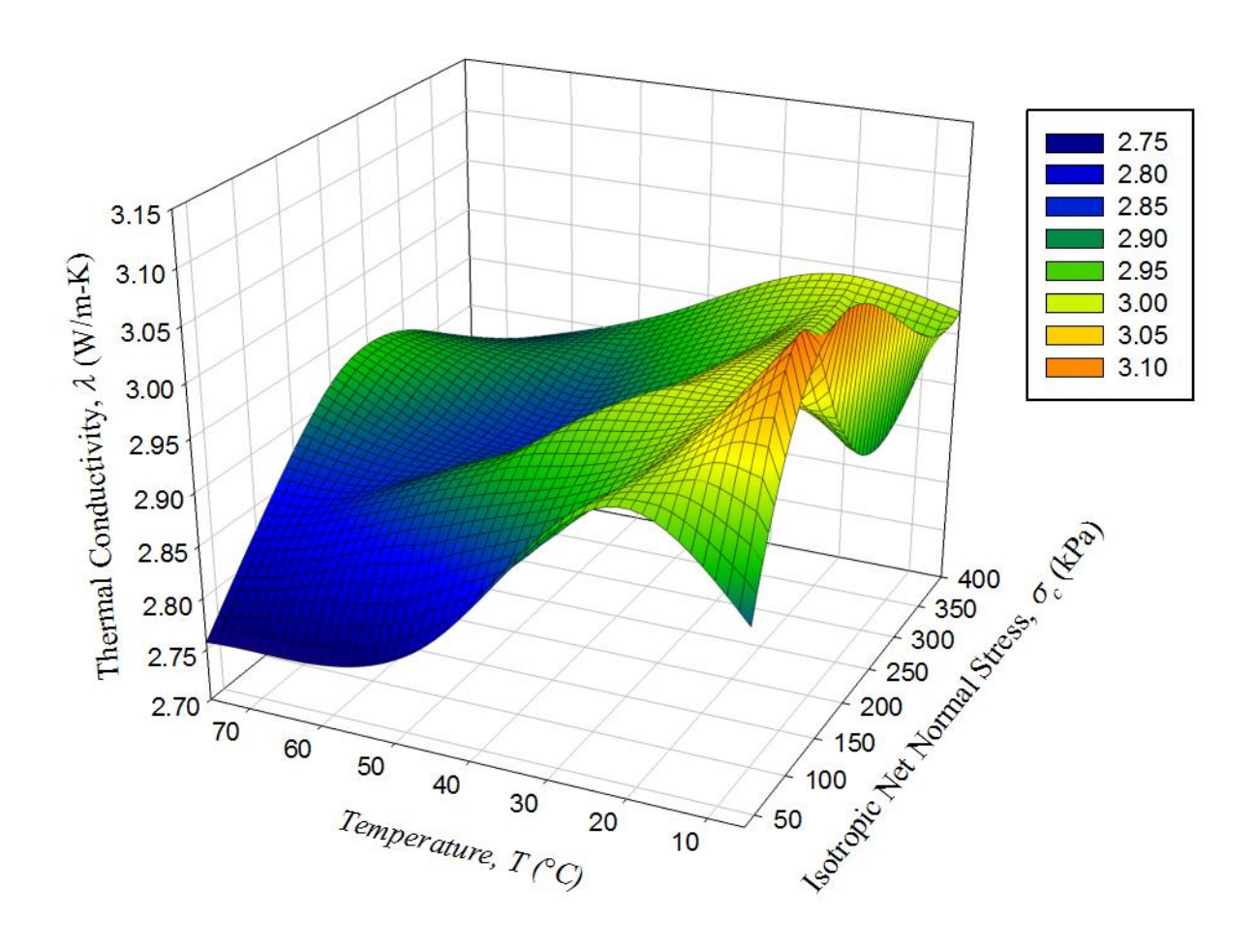


Figure 6-13. The relationship between saturated thermal conductivity (λ_{sat}), temperature (T), and isotropic net normal stress (σ_c) in heating and loading cycles.

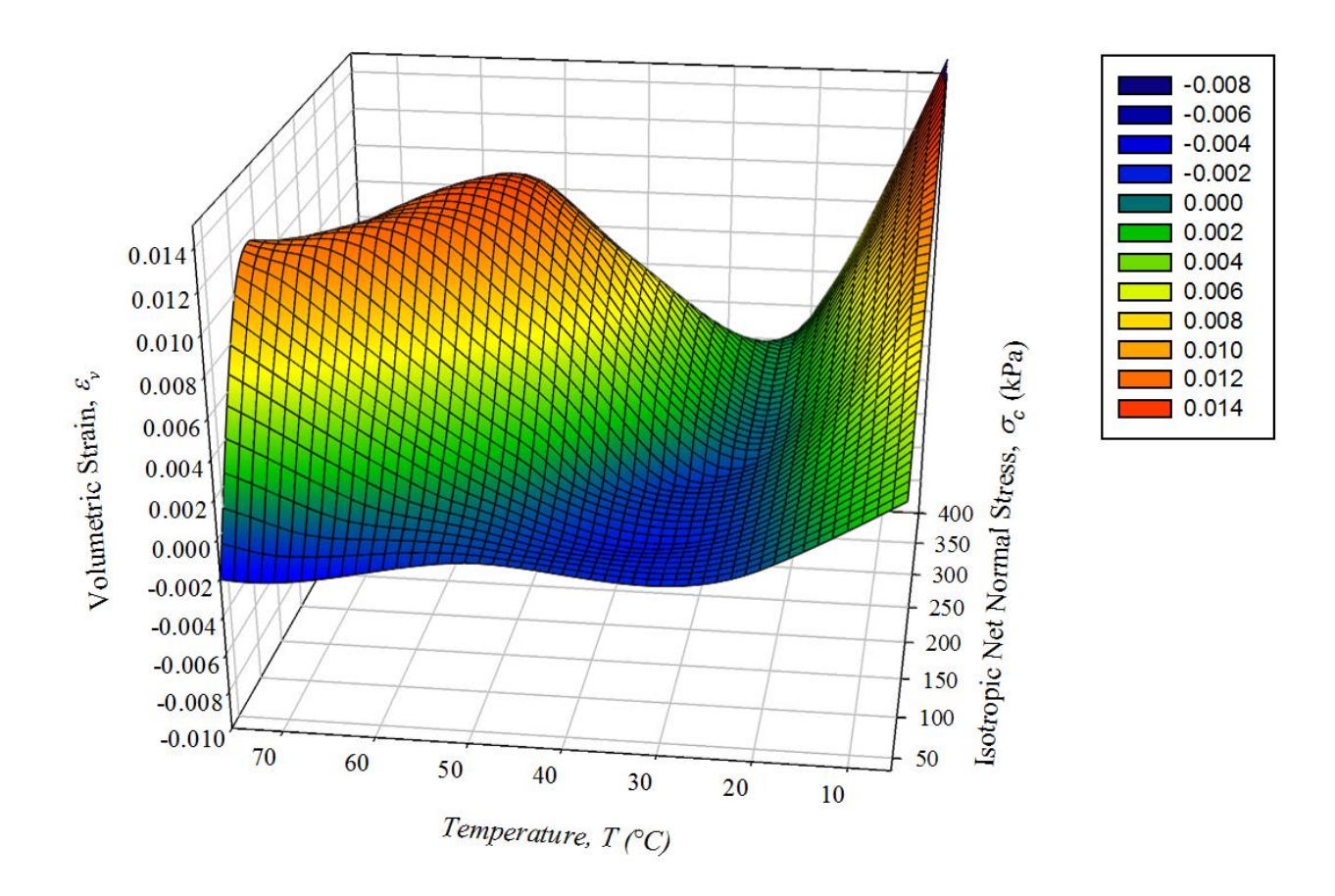


Figure 6-14. The relationship between volumetric strain (ε_{ν}) , temperature (T), and isotropic net normal stress (σ_c) in heating and loading cycles.

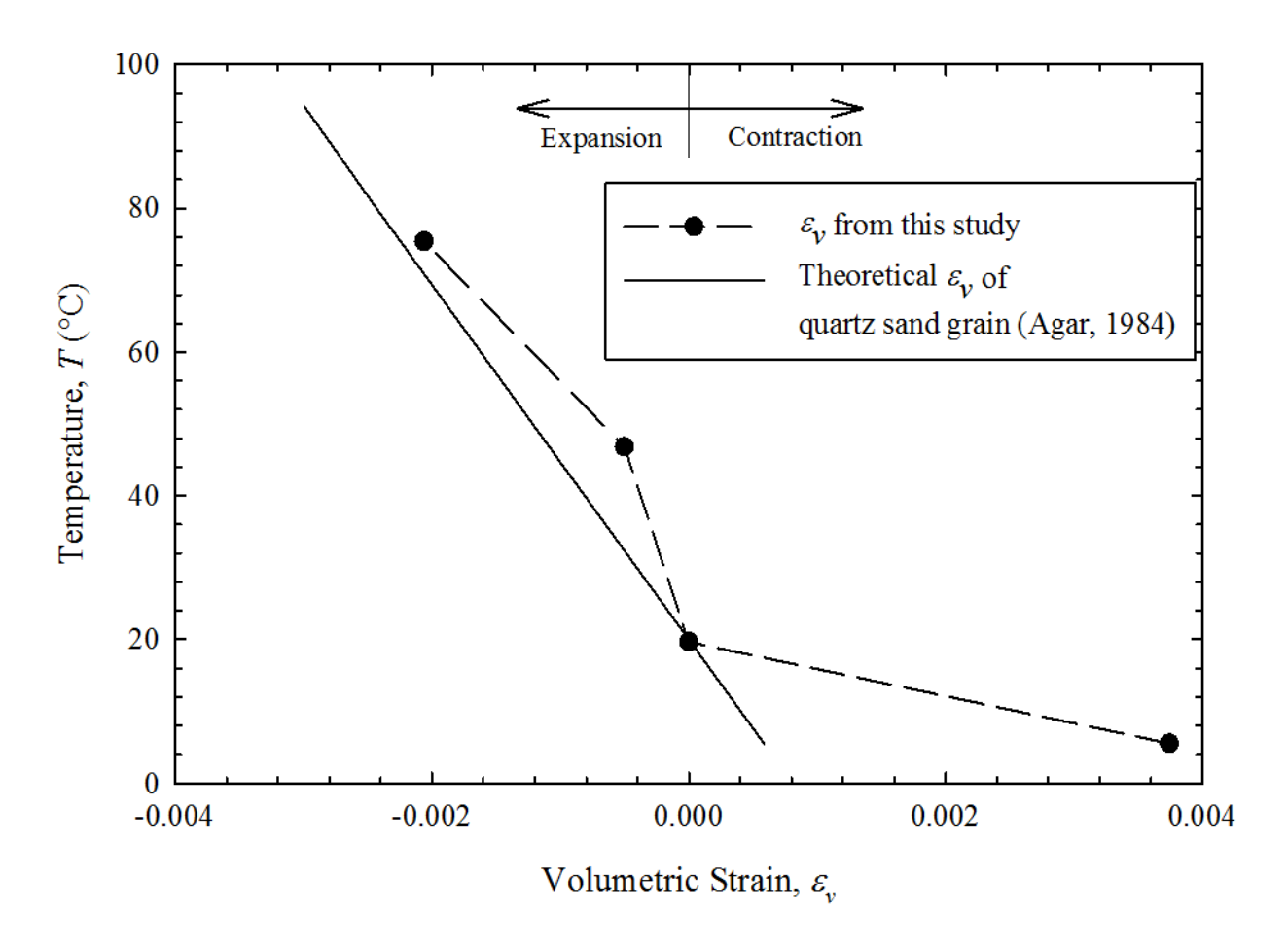


Figure 6-15. The relationship between volumetric strain (ε_v) and temperature (T) in heating direction when $\sigma_c=35$ kPa

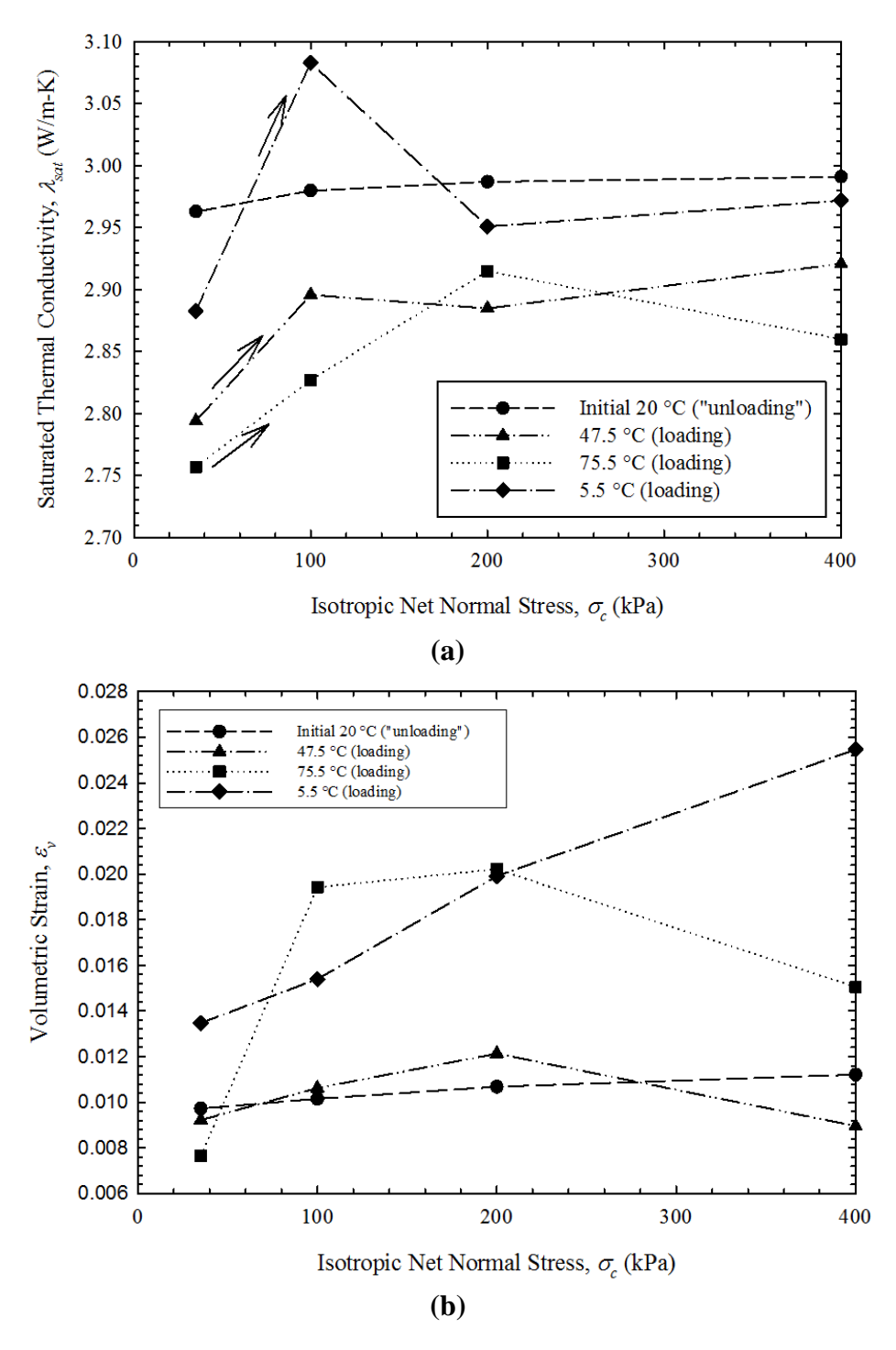


Figure 6-16. The relationship between (a) saturated thermal conductivity (λ_{sat}) and isotropic net normal stress (σ_c) ; and (b) volumetric strain (ε_{ν}) and isotropic net normal stress (σ_c) at each temperature in loading and heating direction.

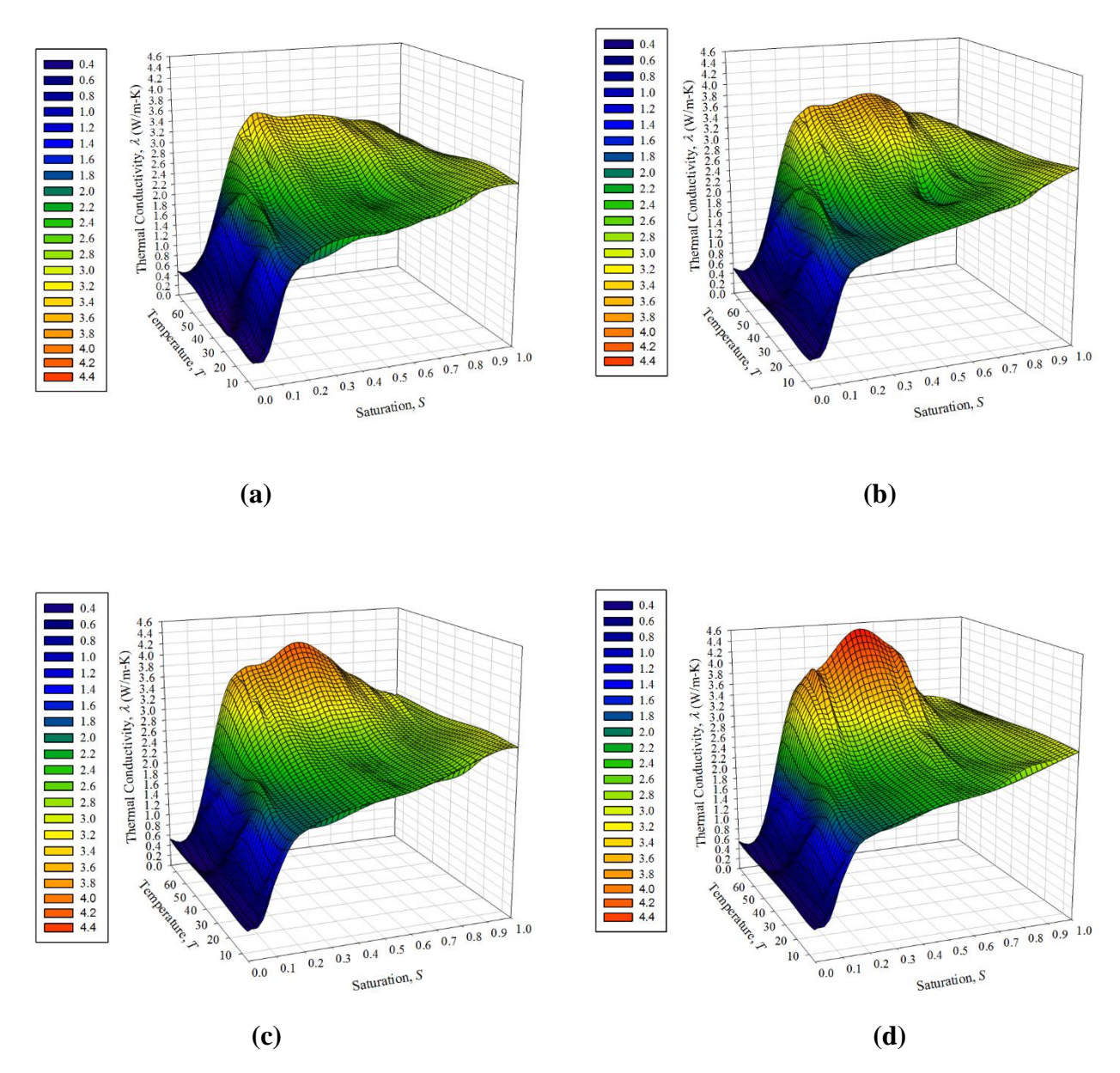


Figure 6-17. Measured thermal conductivity as a function of saturation (S) and temperature (T) when (a) $\sigma_c = 35$ kPa; (b) $\sigma_c = 100$ kPa; (c) $\sigma_c = 200$ kPa; and (d) $\sigma_c = 400$ kPa in heating and loading directions.

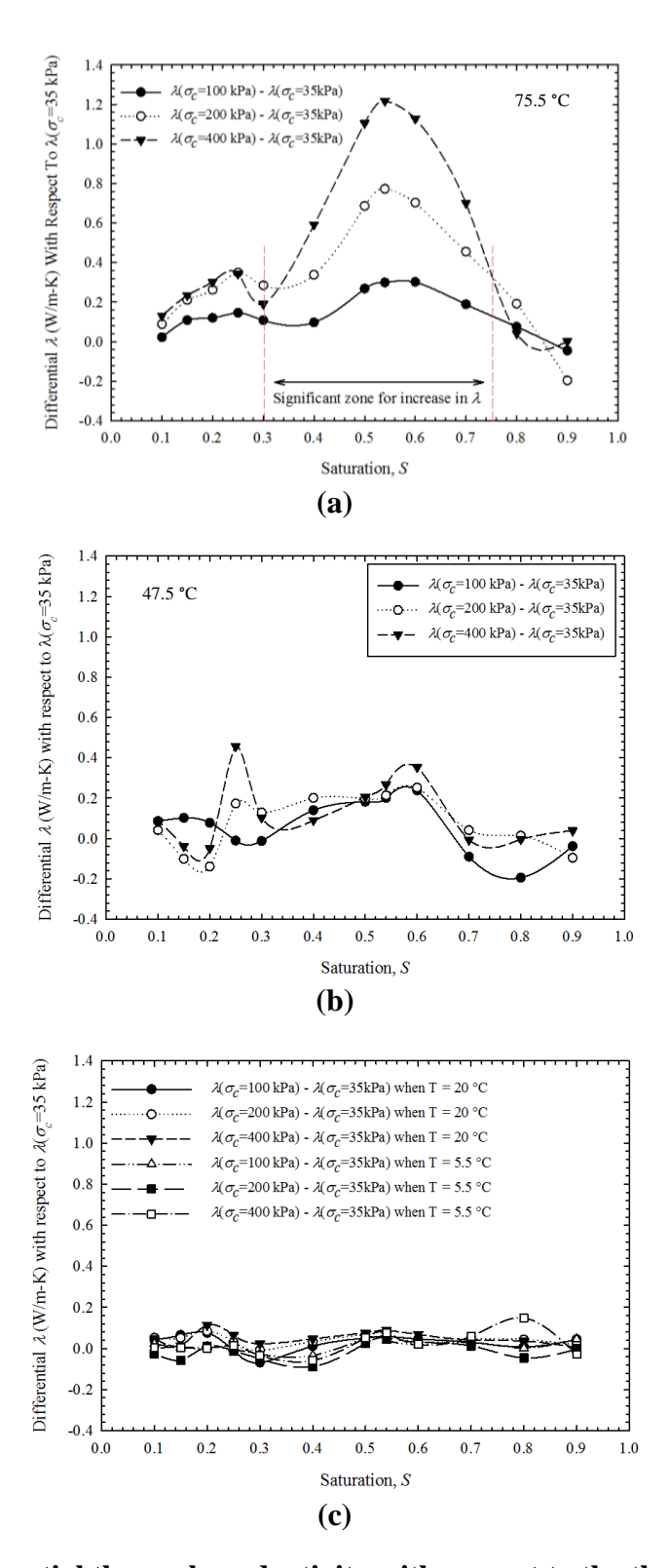


Figure 6-18. Differential thermal conductivity with respect to the thermal conductivity when $\sigma_c = 35$ kPa when (a) T = 75.5 C; (b) T = 47.5 °C; (c) T = 20 °C and 5.5 °C.

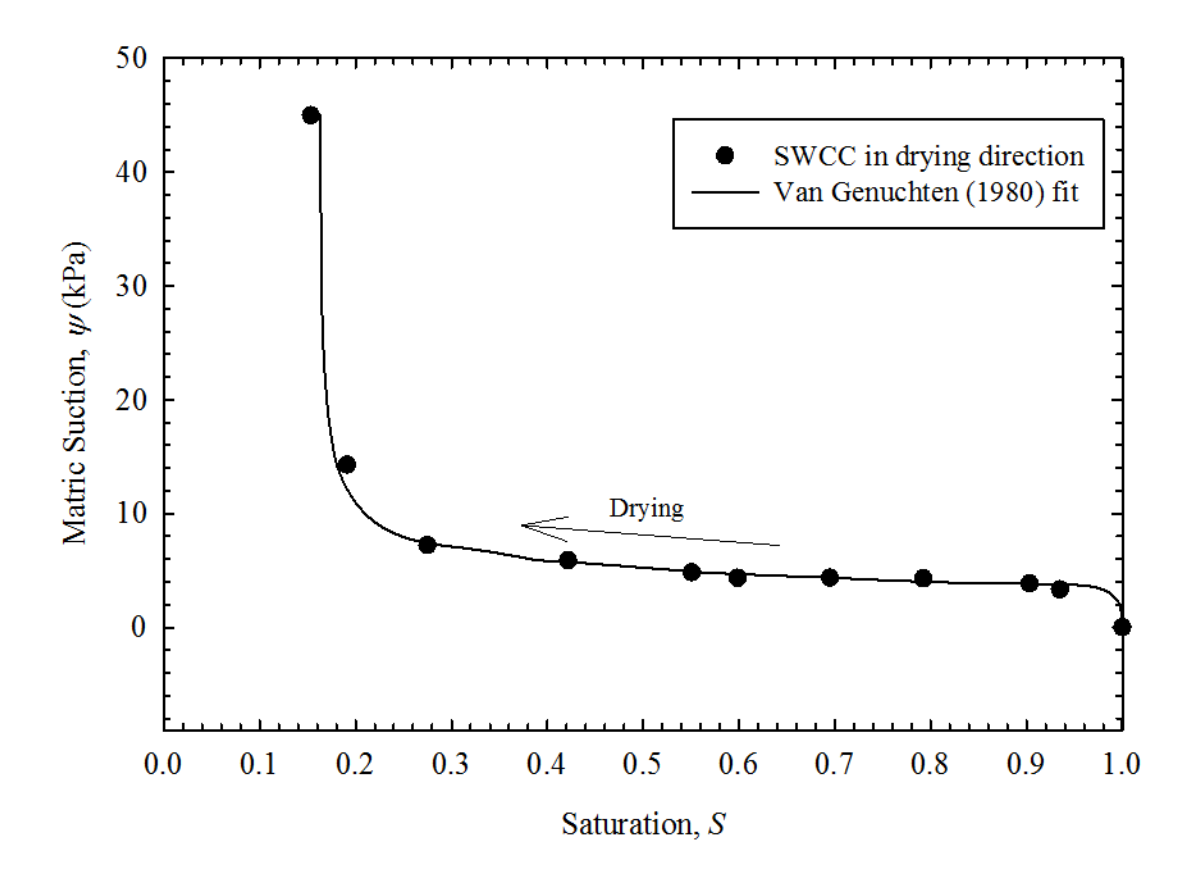


Figure 6-19. Soil water characteristic curve (SWCC) in drying direction obtained from axis-translation technique.

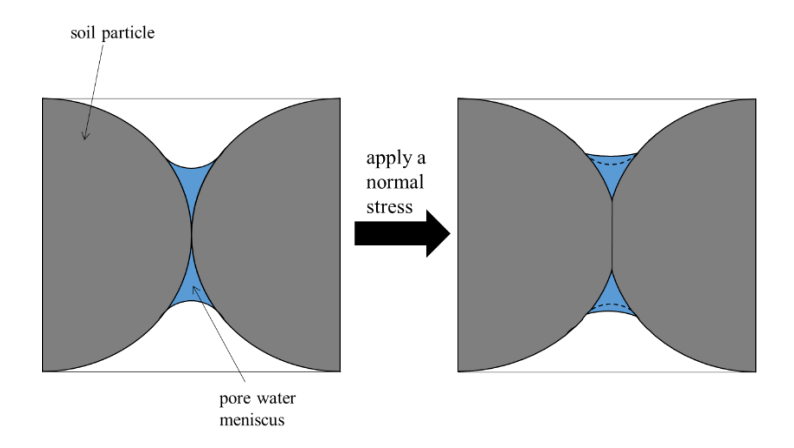


Figure 6-20. Schematic of contact area and pore water meniscus changes due to normal stress (Cho and Santamarina, 2001)

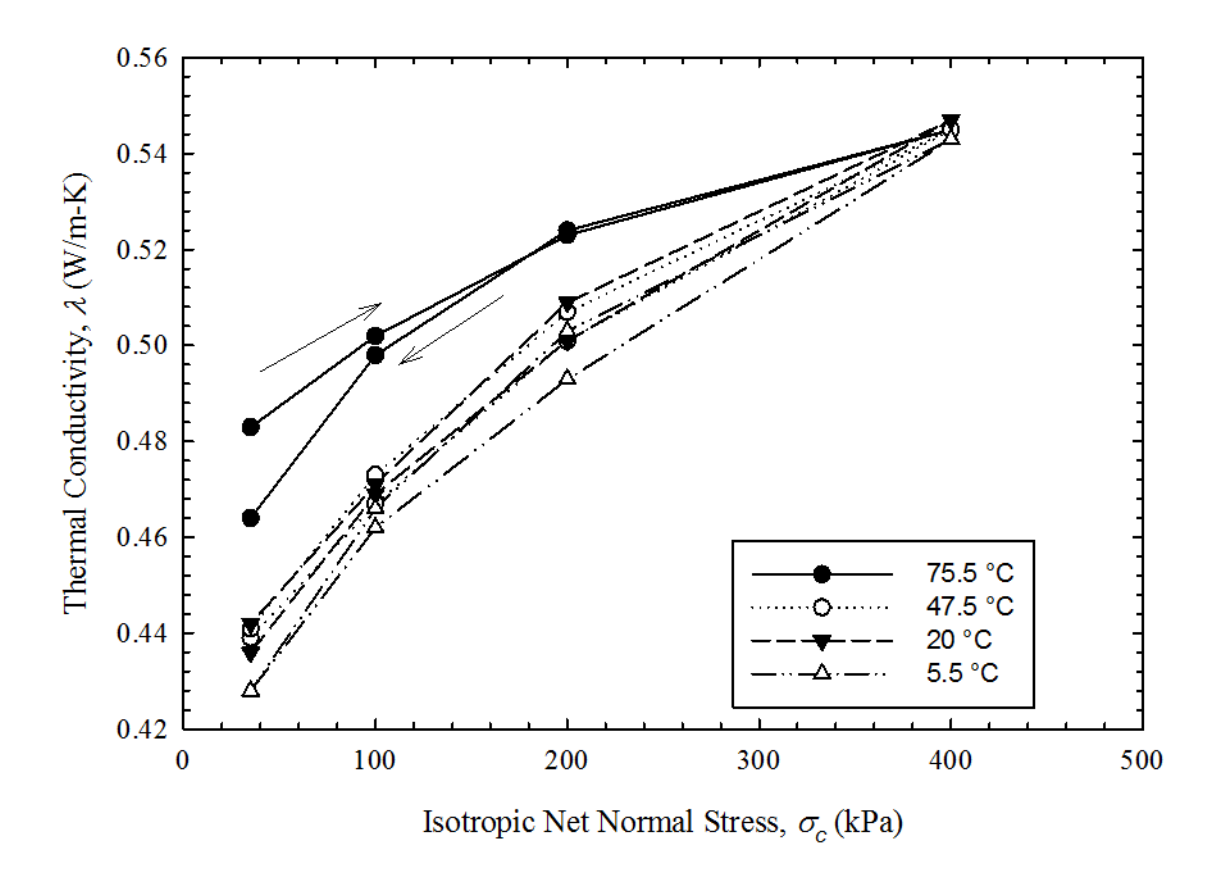


Figure 6-21. Measured thermal conductivity of thermally dried specimen as a function of isotropic net normal stress

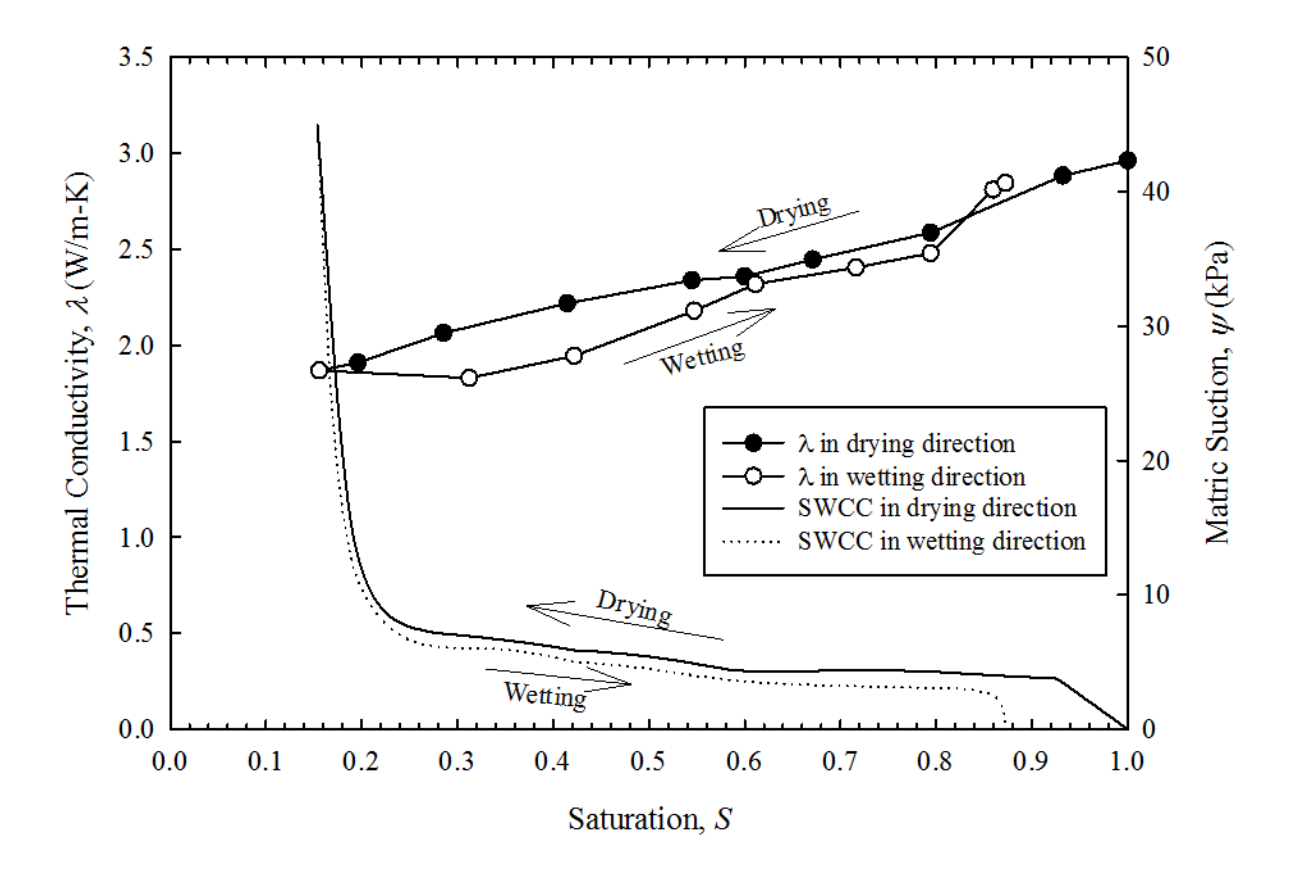


Figure 6-22. Measured thermal conductivity and SWCC in drying and wetting directions

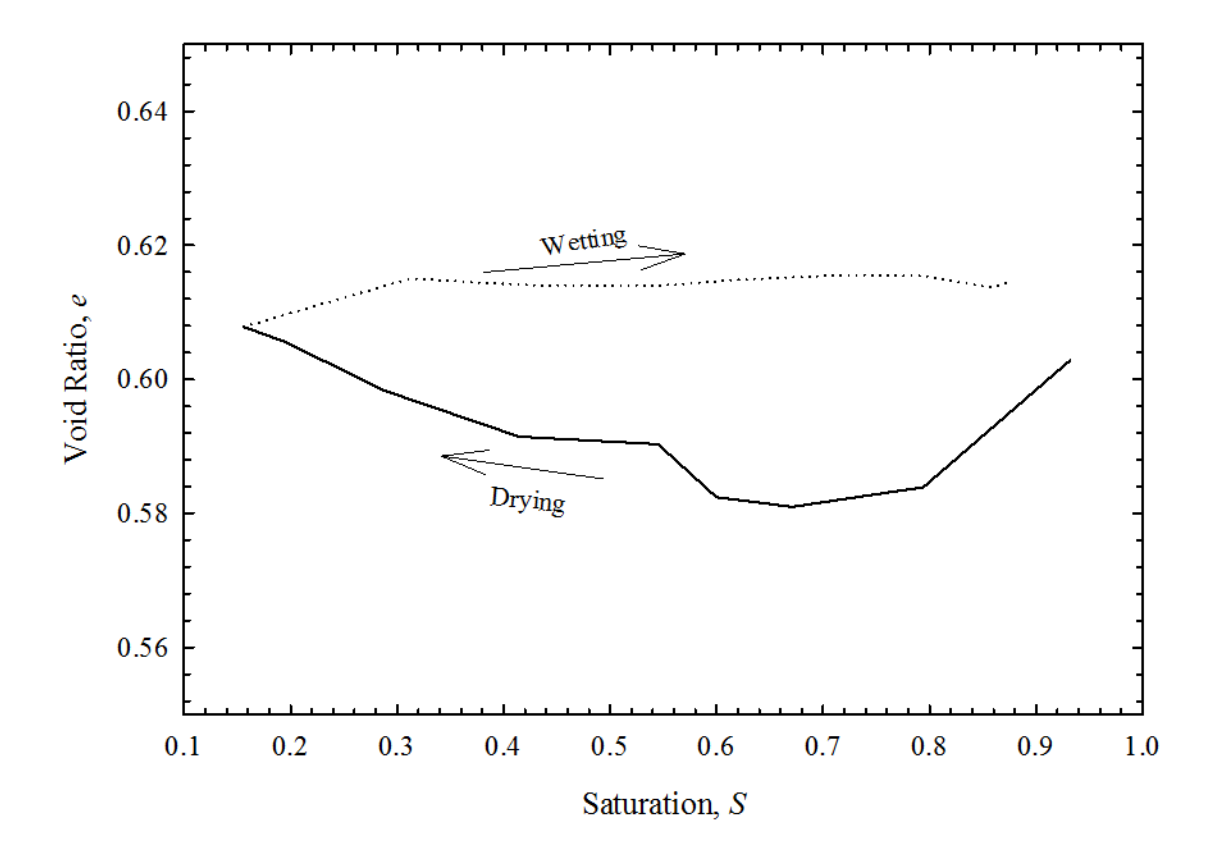


Figure 6-23. Void ratio changes in drying and wetting directions at 35 kPa and 20 °C